Design Studies for the Double Chooz Trigger

Von der Fakultät für Mathematik, Informatik und Naturwissenschaften der RWTH Aachen University zur Erlangung des akademischen Grades eines Doktors der Naturwissenschaften genehmigte Dissertation

vorgelegt von
Master-Physiker **Andi Sebastian Cucoanes**
aus Câmpina (Rumänien)

Berichter:

Universitätsprofessor Dr. rer. nat. Christopher Wiebusch
Universitätsprofessor Dr. rer. nat. Tobias Lachenmaier

Tag der mündlichen Prüfung: 24. Juli 2009

Diese Dissertation ist auf den Internetseiten der Hochschulbibliothek online verfügbar.

Design Studies for the Double Chooz Trigger

Andi Sebastian Cucoanes
III. Physikalisches Institut B - Rheinisch-Westfalische Technische Hochschule Aachen

The main characteristic of the neutrino mixing effect is assumed to be the coupling between the flavor and the mass eigenstates. Three mixing angles $(\theta_{12}, \theta_{23}, \theta_{13})$ are describing the magnitude of this effect. Still unknown, θ_{13} is considered very small, based on the measurement done by the CHOOZ experiment. Although theoretical models cannot explain the big difference between θ_{13} and the other two mixing angles, the true θ_{13} value is likely not far from the present bound. Nevertheless, a non-zero value of θ_{13} allows to experimentally access fundamental physics such as CP violation in the leptonic sector.

In the near future, the experiments which aim to explore the region allowed by CHOOZ, are based on two complementary approaches. The super-beam experiments will use GeV neutrinos and long baselines in oscillation searches based on the appearance channel: $\nu_\mu \rightarrow \nu_e$. On the other side, reactor neutrino experiments search the disappearance of $\bar{\nu_e}$ using 1-2 km baselines and antineutrinos having few MeV energy. Both kinds of experiments have substantially improved sensitivities with respect to CHOOZ.

The next generation reactor neutrino experiments will use multiple detectors in order to reduce the uncertainties related to the neutrino production and interaction. A leading experiment will be Double Chooz, placed in the Ardennes region (northwest of France), on the same site as used by CHOOZ. The Double Chooz goal is the exploration of ~80 % from the currently allowed θ_{13} region, by searching the disappearance of reactor antineutrinos.

Double Chooz will use two similar detectors, located at different distances from the reactor cores: a near one at ~150 m where no oscillations are expected and a far one at 1.05 km distance, close to the first minimum of the survival probability function. The measurement foresees a precise comparison of neutrino rates and spectra between both detectors. The detection mechanism is based on the inverse β-decay.

The Double Chooz detectors have been designed to minimize the rate of random background. In a simplified view, two optically separated regions are considered.

The target, filled with Gd-doped liquid scintillator, is the main antineutrino interaction volume. Surrounding the target, the inner veto region aims to tag the cosmogenic muon background which hits the detector. Both regions are viewed by photomultipliers.

The Double Chooz trigger system has to be highly efficient for antineutrino events as well as for several types of background. The trigger analyzes discriminated signals from the central region and the inner veto photomultipliers. The trigger logic is fully programmable and can combine the input signals. The trigger conditions are based on the total energy released in event and on the PMT groups multiplicity. For redundancy, two independent trigger boards will be used for the central region, each of them receiving signals from half of the photomultipliers. In this way, the hardware failures are easily detected and will not result in a loss of events. A third trigger board will handle the inner veto signals and the additional trigger inputs.

The work presented in this thesis establishes the trigger algorithm as result of the trigger efficiency optimization. The efficiency parameters are obtained from fits of Monte Carlo simulation data. Various possible influences are considered, the resulted algorithm being able to sustain the trigger goals for all kinds of events. Also presented is a method for measuring the trigger efficiency based on the redundancy of the two target trigger boards. This method require experimental and simulated Double Chooz data.

Cosmogenic muons are the dominant source of the Double Chooz triggered events. For the near detector, the foreseen muon rate is $\sim$250 Hz. The DAQ system is unable to sustain the full read-out of the detector at such high frequency. As consequence, the triggered events are treated differently, regarding their importance for future analysis. For physics events, the full available information is saved, the offline data for background muons will contain only summary information. An important concern is related to muons which stop in the target region. They can generate late β-decaying products such as ^{9}Li or ^{8}He, a source of correlated background. The trigger algorithm is able to identify "special" muons classes, for which the full detector read-out is performed. The muon recognition is based on the energy depositions from all detector regions and on the "topological" information provided by groups of inner veto photomultipliers.

Contents

Chapter 1

Understanding Neutrinos

1.1 Introduction

For many years, the neutrino has been a permanent provocation for the particle physics community. Neutrinos interact rarely with matter and have no electrical charge. These properties make them difficult to detect and study.

In the early years of the last century, the violation of energy conservation in beta-decays was interpreted by Pauli as an indication of the existence of a new fermion [1]. It was 1930 and this "wenig wahrscheinlich"[1] presumption was recognized later as the birth of the neutrino. Pauli considered the new particle as being neutral and weakly interacting. He also assumed that this particle has a mass smaller than the electron mass and spin 1/2.

The first method for the neutrino mass determination was proposed in 1933 by Fermi [2] and Perrin [3] and involves the investigation of the high-energy part of the β-spectrum.

The first direct observation of neutrinos was made later, in 1956, when Reines and Cowan succeeded to detect reactor antineutrinos [4, 5] from inverse β-decay events:

$$\overline{\nu}_e + p \rightarrow e^+ + n \qquad \text{Threshold: } 1.806\,\text{MeV} \tag{1.1}$$

They measured the delayed coincidence between the e^+ annihilation:

$$e^+ + e^- \rightarrow 2\gamma \tag{1.2}$$

[1]less probable (german)

and the neutron capture on cadmium using a detector based on liquid scintillator.

A step further was done in 1957 by Salam and Landau [6] with the so called "theory of the two component neutrino". They introduced the idea of a massless neutrino as an explanation for the large parity violation in the processes of emission and absorption of neutrino. One year later, neutrinos were found to be left-handed [7], in agreement with the two component neutrino theory.

Later studies showed three neutrino flavors, which were named according to the accompanied leptons: electron-, muon- and tau- neutrinos. The number of neutrinos coupling to the Z boson was measured by LEP from 1990 until 1995 and it was found to be $2.98 \pm 0.07\,(\text{stat.}) \pm 0.07\,(\text{syst.})$ [8]. Nevertheless, this result does not exclude the existence of light "sterile" neutrinos which might not couple to the W or Z bosons.

It is well recognized that one of the greatest achievements in particle physics, is the Standard Model ($\mathcal{SM}$) elaborated by Glashow, Salam and Weinberg [9] in the second part of the last century.

The $\mathcal{SM}$ is a renormalizable gauge field theory, describing the interactions of the fundamental matter constituents. Within this framework, the interacting particles are two kinds of fermions (spin $\pm 1/2$ particles): the leptons and the quarks. They are listed in table (1.1).

The $\mathcal{SM}$ also accounts for three kinds of possible interactions between fermions, namely electromagnetic-, weak- and strong- interactions. The gravitational interactions are not described within $\mathcal{SM}$, as for the regime over which the model is believed to be valid, the gravitational induced effects are negligible. The fundamental interactions are mediated by the exchange of gauge boson particles shown in table (1.2).

The $\mathcal{SM}$ considers only left handed neutrino states (L). The weak interactions associate neutrinos according to their flavor in leptons doublets:

$$\begin{pmatrix} \nu_l \\ l^- \end{pmatrix}_L$$

where $\mathrm{l} = \mathrm{e}, \mu, \tau$ are the charged lepton eigenstates.

Neutrinos are massless within the $\mathcal{SM}$.

Gen.	Flavor	Q	$(T_3)_L$	Mass (MeV)
1	e	-1	$-\frac{1}{2}$	0.51
	ν_e	0	$+\frac{1}{2}$	$< 3\times10^{-6}$
2	μ	-1	$-\frac{1}{2}$	105.7
	ν_μ	0	$+\frac{1}{2}$	< 0.19
3	τ	-1	$-\frac{1}{2}$	1777
	ν_τ	0	$+\frac{1}{2}$	< 18.2
1	u	$+\frac{2}{3}$	$+\frac{1}{2}$	1.5-3
	d	$-\frac{1}{3}$	$-\frac{1}{2}$	3-7
2	c	$+\frac{2}{3}$	$+\frac{1}{2}$	1250±90
	s	$-\frac{1}{3}$	$-\frac{1}{2}$	90±25
3	t	$+\frac{2}{3}$	$+\frac{1}{2}$	174200±3300
	b	$-\frac{1}{3}$	$-\frac{1}{2}$	4200±70

Table 1.1: **Properties and quantum numbers of fermions** Q is the electromagnetic charge of the particle in units of e; T_3 is the weak isospin of the particle. The subscript L indicates that only left handed chiral particles and right handed anti-particles feel the weak force. [10].

Boson	Q	Spin	Mass (GeV)
γ	0	1	0
$W^{\pm}$	±1	1	80.4
Z^o	0	1	91.1
g	0	1	0
H	0	0	> 114.4

Table 1.2: **Properties and quantum numbers of bosons** Q is the electromagnetic charge of the particle in units of e. [10]. The value of the Higgs boson mass was obtained from direct searches at LEP [11].

1.2 Experimental Evidence for Neutrino Oscillations

First observations of solar neutrinos shown contradictions between measured fluxes and the solar model. In addition, the experiments which measure neutrinos generated in the earth's atmosphere did not agree with theirs expectations. These incompatibilities generated the so-called solar and atmospheric "anomalies". The welcomed solution is indicated by Pontecorvo [12] with the neutrino oscillation theory.

1.2.1 Solar Neutrinos

The present knowledge related to the Sun is synthesized by the "Standard Solar Model" (SSM) [13] and confirmed by helioseismological measurements. The thermonuclear reactions, which generate the solar energy, occur mainly via the "pp-chain" summarizing the fusion reaction of protons into helium [14]:

$$4p + 2e \rightarrow {}^4\mathrm{He} + 2\nu_e + 26.73\,\mathrm{MeV} \tag{1.3}$$

Here, the neutrinos carry only a small fraction from the released energy, more precisely, 590 KeV. The pp-chain is the principal production mechanism of solar neutrinos. It contains several branches, some of which generate neutrino. Other reactions which release solar neutrinos are listed in table (1.3).

Reaction	Energy of ν (MeV)
$p + p \rightarrow {}^2H + e^+ + \nu_e$	≤ 0.42
$p + e + p \rightarrow {}^2H + \nu_e$	1.44
${}^7Be + e \rightarrow {}^7Li + \nu_e$	(90%) 0.86
	(10%) 0.38
${}^8B \rightarrow {}^8Be* + e^+ + \nu_e$	~ 15
${}^3He + p \rightarrow {}^4He + e^+ + \nu_e$	≤ 18.77
${}^{13}N \rightarrow {}^{13}C + e^+ + \nu_e$	≤ 1.2
${}^{15}O \rightarrow {}^{15}N + e^+ + \nu_e$	≤ 1.7

Table 1.3: **The production reactions of solar neutrino.** [17].

The energy spectra of the neutrinos created by the main solar reactions is shown in figure (1.1). One can see that higher energetic neutrinos have smaller contributions to the total flux. The integrated solar neutrino flux at the Earth surface is:

$$\Phi_\nu^{solar} = 6.4 \times 10^{10}\,\nu/\mathrm{cm}^2\mathrm{s} \tag{1.4}$$

Two kinds of experiments searched for neutrinos coming from the Sun, using radiochemical techniques or using Cherenkov radiation generated by neutrino scatterings inside large volumes of water.

The radiochemical detection of solar neutrinos is based on inverse β-decay. The reaction can use chlorine (as in the Homestake experiment [18]):

$$\nu_e + {}^{37}\mathrm{Cl} \rightarrow e + {}^{37}\mathrm{Ar} \qquad \text{Threshold: } 0.8\,\mathrm{MeV} \tag{1.5}$$

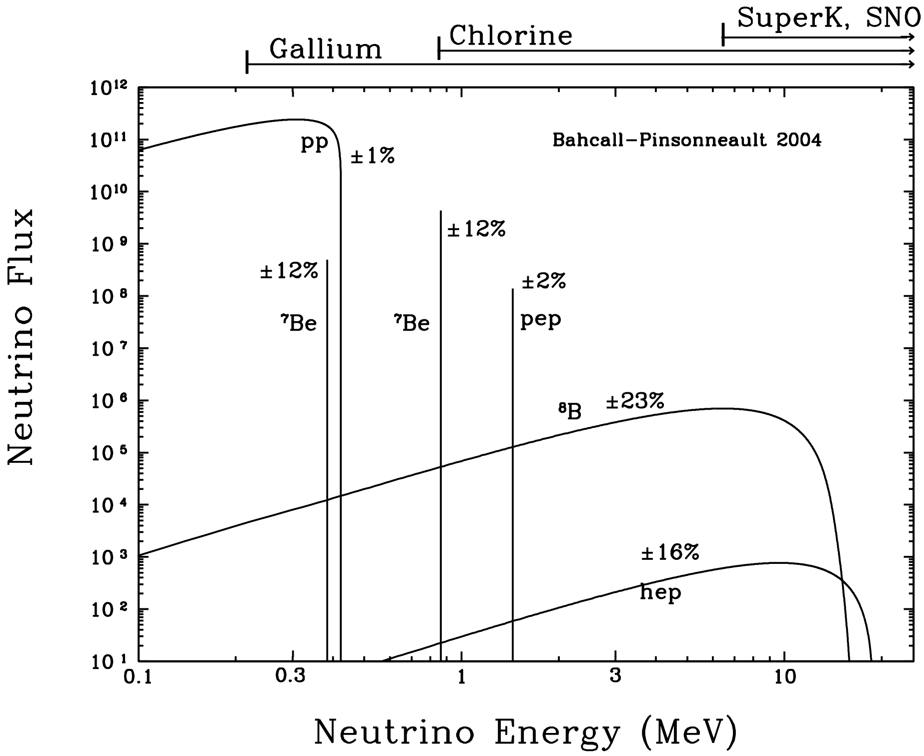

Figure 1.1: **The solar neutrino energy spectrum as predicted by the SSM.** The upper side represents the threshold energies for the different classes of solar neutrino experiments [16].

or gallium (as in GALLEX [19] or in SAGE [20] experiments).

$$\nu_e + {}^{71}\mathrm{Ga} \rightarrow e + {}^{71}\mathrm{Ge} \qquad \text{Threshold: } 0.2\,\mathrm{MeV} \tag{1.6}$$

In both cases, the isotopes are extracted at time intervals comparable with their decay times, typically 20-30 days. The number of isotopes is a measure of the neutrino interactions. The advantage of this detection technique lies in the very low energy threshold, especially for gallium-based experiments. This allows the measurement of low energetic *pp* neutrinos (figure 1.1). However, no particular information on the specific neutrino energy, direction or the arrival time is provided.

Complementary, information about high-energetic solar neutrinos was brought by water-Cherenkov experiments such as Kamiokande [22], SNO [29] and Super-Kamiokande [30]. All water-Cherenkov detectors are sensitive to solar neutrino, through electron-neutrino elastic-scattering (ES):

$$\text{ES:} \quad \nu_x + e^- \rightarrow \nu_x + e^- \tag{1.7}$$

The reaction (1.7) is produced at all neutrino energies. The energy depositions are measured by detectors having large areas of photomultipliers (PMT). The number of hit PMT is a measure of the neutrino energy.

Thresholds, established for each experiment, are mainly given by background considerations. The values are usually high, e.g. 7 MeV for Kamiokande, 5 MeV for Super-Kamiokande, constraining the sensitivity of water-Cherenkov experiments to ^{8}B neutrinos (1.1) only. The direction of recoiled electron in reaction (1.7) is correlated with the direction of the incoming neutrino resulting in background rejection.

Another example is the SNO detector which uses heavy water (D_2O) in its fiducial volume. The advantage is a separation of electron neutrinos from other neutrino flavors. The electron neutrinos are detected using charge-current (CC) scatterings on deuteron. The neutral-current (NC) reaction, additionally produced, is immune to neutrino flavors.

$$\text{CC:} \quad \nu_e + d \rightarrow p + p + e \qquad \text{Threshold: } 1.4\,\text{MeV} \tag{1.8}$$

$$\text{NC:} \quad \nu_x + d \rightarrow \nu_x + p + n \qquad \text{Threshold: } 2.2\,\text{MeV} \tag{1.9}$$

Surprisingly, the number of electron neutrinos counted experimentally seems to not coincide with those predicted by Standard Solar Model. The summary of experimental results and the SSM expectations are shown in figure (1.2). The total number of neutrinos predicted by SSM coincides with the experimental results (the last set of columns in figure 1.2). This fact represents another confirmation of the SSM predictions, and a hint for neutrino oscillation.

1.2.2 Atmospheric Neutrinos

The discrepancy between experimental results and the numbers of expected neutrinos persists also for neutrinos induced in atmosphere by cosmic rays. In this

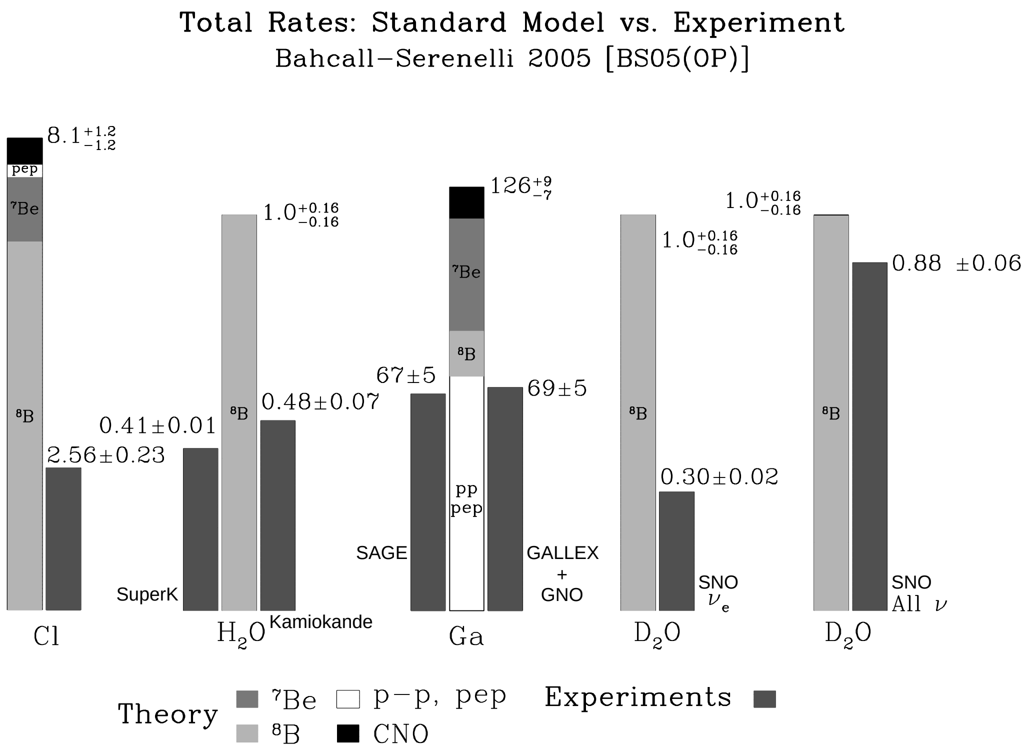

Figure 1.2: **The measured solar neutrino rates as compared with the SSM predictions.** For the radiochemical experiments, the units are SNU (1 SNU $= 10^{-36}$ captures per target atom per second); for water-Cherenkov experiments, the ratio data/experiment is shown. [16].

case, the main production mechanism is:

$$\text{Cosmic rays } (p, \alpha, \dots) + \text{ Air } (N_2, O_2, \dots) \rightarrow \pi^{\pm} + X \tag{1.10}$$

$$\pi^{\pm} \rightarrow \mu^{\pm} + \nu_{\mu}(\bar{\nu_{\mu}}) \tag{1.11}$$

$$\mu^{\pm} \rightarrow e^{\pm} + \nu_e(\bar{\nu_e}) + \bar{\nu_{\mu}}(\nu_{\mu}) \tag{1.12}$$

As a direct consequence of reactions (1.11) and (1.12), the fraction between the electron and the muon neutrino fluxes is assumed to be 1/2. In reality, this number might be different depending on the secondary effects like differences in the pions and muons lifetimes or other neutrino production mechanisms.

The atmospheric neutrino experiments count for the following double ratio in which the systematic uncertainties largely cancel:

$$R(\mu/e) \equiv \frac{[(\nu_\mu + \bar{\nu_\mu})/(\nu_e + \bar{\nu_e})]_{measured}}{[(\nu_\mu + \bar{\nu_\mu})/(\nu_e + \bar{\nu_e})]_{expected}} \tag{1.13}$$

Here, the denominator considers all effects previously mentioned. $R(\mu/e)$ is expected to be close to unity.

In general, atmospheric neutrinos cover the energy range from 10 MeV to more than 10 GeV [21] and are detected via charge-current reactions:

$$\nu_e(\bar{\nu_e}) + A \rightarrow e^-(e^+) + X \tag{1.14}$$

$$\nu_\mu(\bar{\nu_\mu}) + A \rightarrow \mu^-(\mu^+) + X \tag{1.15}$$

The atmospheric neutrino flux was measured by water-Cherenkov detectors like Kamiokande [22], IMB [23] and Super-Kamiokande [24] but also by iron calorimeter experiments such as Frejus [25], Soudan [26] and NUSEX [27]. For iron calorimeter experiments, the target is composed of iron layers alternating with tracking elements such as plastic drift tubes. The tracking system allows the reconstruction of charged particles such as muons and electrons using reactions (1.15).

A clear evidence was obtained by the Super-Kamiokande collaboration [24]. They measured the zenith angle dependency of the electron and muon neutrino fluxes. The zenith angle [15] is defined as:

$$\cos\theta = \begin{cases} 1 & \Longrightarrow \nu \text{ come from above} \\ 0 & \Longrightarrow \nu \text{ come from horizon} \\ -1 & \Longrightarrow \nu \text{ come from below} \end{cases} \tag{1.16}$$

The neutrino flux has been found to lie within the range of predictions for $\bar{\nu_e}$ and smaller for upward going $\bar{\nu_\mu}$ (coming from below). This result is shown in figure (1.3).

1.3 The Neutrino Oscillation Formalism

The neutrino oscillation theory is the most favored formalism accounting for interflavor neutrino transition. The idea of mixing between the weak and the mass eigenstates is already known in $\mathcal{SM}$. The CKM ("Cabibbo-Kobayashi-Maskawa")

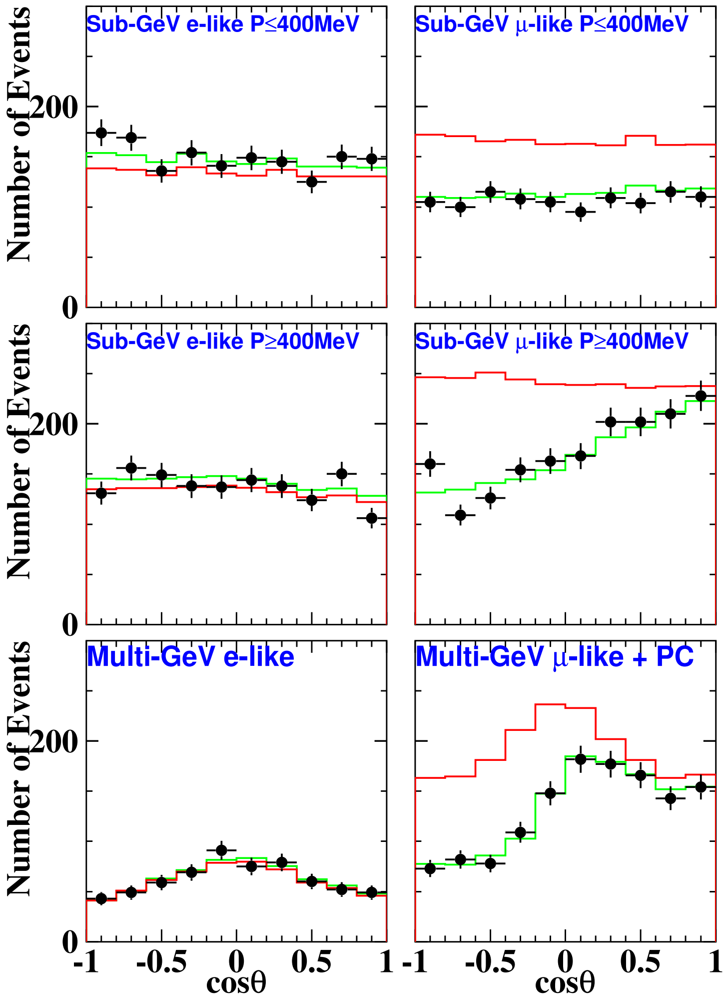

Figure 1.3: **Zenith angle distribution from Super-Kamiokande.** The left panels corresponds to the e-like events and the right ones to the μ-like events. The energy range increases from the top panels to the down panels [24].

mixing matrix accounts for mixing between weak and strong eigenstates in the quark sector. Based on the same idea, the neutrino flavor transitions are described by the PMNS ("Pontecorvo-Maki-Nakagawa-Sakata") matrix.

In the hypothesis of massive neutrinos, the neutrino flavor eigenstates, $|\nu_\alpha\rangle$ can be considered as a linear superposition of orthogonal mass eigenstates:

$$|\nu_\alpha\rangle = \sum_i U_{\alpha i}|\nu_i\rangle \qquad (\alpha = e,\, \mu,\, \tau) \tag{1.17}$$

where $U_{\alpha i}$ corresponds to the neutrino weak-eigenstate α and the neutrino mass-eigenstate i.

Relation (1.17) describes a stationary state of a neutrino and is the basis of neutrino oscillations phenomenon. The propagating state is given by the Schrödinger equation, affecting mass-eigenstates:

$$|\nu_\alpha(t)\rangle = \sum_i U_{\alpha i} e^{-iE_i t}|\nu_i(t)\rangle \tag{1.18}$$

Here, E_i is the energy of the respective mass eigenstate component. Using the relativistic approximation ($p_i \equiv p \simeq E$), E_i becomes:

$$E_i = \sqrt{p_i^2 - m_i^2} \simeq p + \frac{m_i^2}{2E} \tag{1.19}$$

The propagation of a neutrino with mixed mass eigenstates results in different relative phases between these states. Hence, the flavor composition will evolve depending on neutrino energy. Using equation (1.18), the transition amplitude is given by:

$$\mathrm{A}(\nu_\alpha \to \nu_\beta) = \langle\nu_\beta|\nu_\alpha(t)\rangle = \sum_{i,j}\langle\nu_j|U_{\alpha i}U^*_{\beta j}e^{-iE_i t}|\nu_i(t)\rangle = \sum_i U_{\alpha i}U^*_{\beta i}e^{-iE_i t} \tag{1.20}$$

The probability for this transition is:

$$\begin{aligned}\mathrm{P}(\nu_\alpha \to \nu_\beta) &= |\mathrm{A}(\nu_\alpha \to \nu_\beta)|^2 = \\ &= \sum_i |U_{\beta i}|^2\,|U_{\alpha i}|^2 + 2\,\mathrm{Re}\sum_{j>i} U^*_{\beta i}U_{\beta j}U_{\alpha i}U^*_{\alpha j}e^{i\Delta_{ij}}\end{aligned} \tag{1.21}$$

where:

$$\Delta_{ij} = (E_i - E_j)t \simeq \frac{m_i^2 - m_j^2}{2E}t = \Delta m^2_{ij}\frac{L}{2E} \tag{1.22}$$

The amplitudes of flavor transitions are proportional to the mixing matrix elements. The oscillations are permitted for non degenerate mass states ($\Delta m^2_{ij} \neq 0$)

and $U_{\beta i} U_{\alpha i} \neq 0$

If one assumes three flavor formalism, the mixing matrix is 3×3 and can be parametrized using three angles $0 \leq \theta_{ij} \leq \pi/2$ with $i, j = 1, 2, 3$. These angles determine the amplitude of weak-mass eigenstates transitions.

A common representation of the mixing matrix [17] is the following:

$$U_{PMNS} = \begin{pmatrix} c_{12}c_{13} & s_{12}c_{13} & s_{13}e^{-i\delta} \\ -s_{12}c_{23} - c_{12}s_{23}s_{13}e^{i\delta} & c_{12}c_{23} - s_{12}s_{23}s_{13}e^{i\delta} & s_{23}c_{13} \\ s_{12}s_{23} - c_{12}c_{23}s_{13}e^{i\delta} & -c_{12}s_{23} - s_{12}c_{23}s_{13}e^{i\delta} & c_{23}c_{13} \end{pmatrix} \tag{1.23}$$

$$= \begin{pmatrix} 1 & & \\ & c_{23} & s_{23} \\ & -s_{23} & c_{23} \end{pmatrix} \begin{pmatrix} c_{13} & & s_{13}e^{i\delta} \\ & 1 & \\ -s_{13}e^{i\delta} & & c_{13} \end{pmatrix} \begin{pmatrix} c_{12} & s_{12} & \\ -s_{12} & c_{12} & \\ & & 1 \end{pmatrix} \tag{1.24}$$

$$= M_{23} \times M_{13} \times M_{12} \tag{1.25}$$

where $c_{ij} = \cos\theta_{ij}$ and $s_{ij} = \sin\theta_{ij}$. δ represents a CP-violation phase with $-\pi \leq \delta \leq \pi$. One can observe that a non-zero $\sin\theta_{13}$, would allow the observation of CP violation in the lepton sector. If neutrinos were Majorana particles, the formalism would include additional CP-violation phases. However, the Majorana phases cancel out when one obtains oscillation probabilities.

The relation (1.25) shows three matrix components involving mixing angles:

M_{23} corresponds to atmospheric neutrino oscillations. These are dominated by $\nu_\mu \to \nu_\tau$ transitions, as shown by the Super-Kamiokande result.

M_{12} describes the solar neutrino oscillations, dominated by $\nu_e \to \nu_\mu$ transitions.

M_{13} , based on θ_{13}, considers $\nu_\tau \to \nu_e$ transitions which have not been observed so far. The smallness of θ_{13} (given mainly by the CHOOZ experiment [33]), permits the effective de-coupling between the solar and the atmospheric components: M_{23} and M_{12}. In this case, one can use a simplified structure for M_{23} and M_{12}:

$$U = \begin{pmatrix} \cos\theta & \sin\theta \\ -\sin\theta & \cos\theta \end{pmatrix} \tag{1.26}$$

where θ can be replaced with the solar or atmospheric mixing angles.

In this case, the transition probability between two neutrino flavors can be written as:

$$P(\nu_\alpha \rightarrow \nu_\beta) = \sin^2(2\theta_{13}) \cdot \sin^2\left(\frac{1.27 \cdot \Delta m^2[eV^2] \cdot L[km]}{E[GeV]}\right) \tag{1.27}$$

1.4 Oscillations Searches Using Reactor Neutrinos

The nuclear reactors are an important source of terrestrial antineutrinos. The β-decays of nuclear fission fragments release electron antineutrinos having energies in range of a few MeV (figure 1.4). Since the antineutrinos are emitted isotropically by reactors, the flux decreases with the square of traveled distance. Oscillation experiments search for deviations from this rule by counting the number of antineutrinos at a given distance L normalized to the number of antineutrinos emitted by reactor. So, one expects a decrease of the normalized flux in case of oscillations.

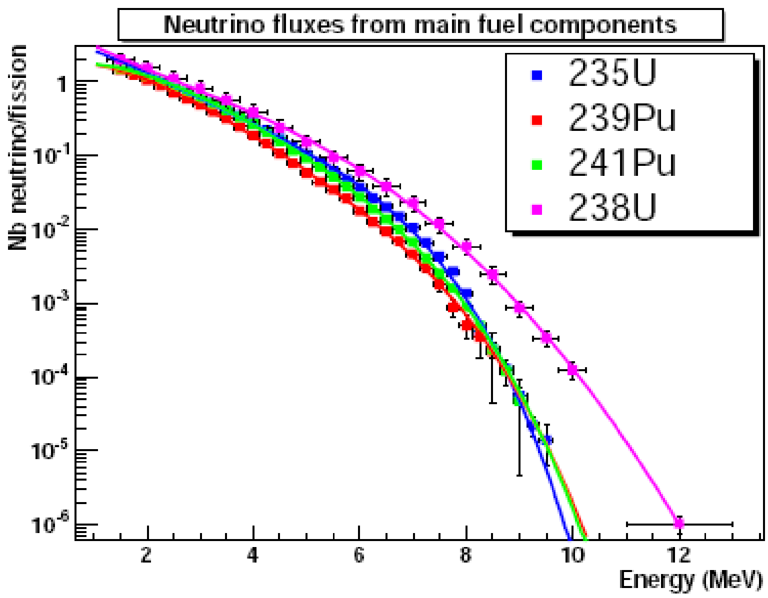

Figure 1.4: **The ν_e energy spectrum of the four dominant isotopes** [31].

The low energy of reactor antineutrinos permits the exploration of small Δm^2 values (1.27). An additional increase of L would require a larger neutrino flux given by more powerful reactors and/or a detector with a large fiducial volume.

Until now, two reactor neutrino experiments had an important impact on the regions where the oscillation parameters are allowed: KamLAND [32] and CHOOZ [33].

KamLAND uses the same underground site as the Kamiokande experiment. It is located at ∼180 km from powerful nuclear reactors and contains 1000 tons of pure scintillator liquid in its fiducial volume. The detection mechanism is based on the inverse β-decay (1.1). The neutron capture representing the delayed event is produced by protons from hydrogen atoms.

The KamLAND collaboration measured neutrino fluxes in very good concordance with the oscillation hypothesis. The normalized neutrino flux generated by reactors was found to be lower [32] with respect to the no oscillation hypothesis. The strong evidence for neutrino oscillations is given by the L/E dependency of the $\bar{\nu}_e$ survival probability as shown in the figure (1.5).

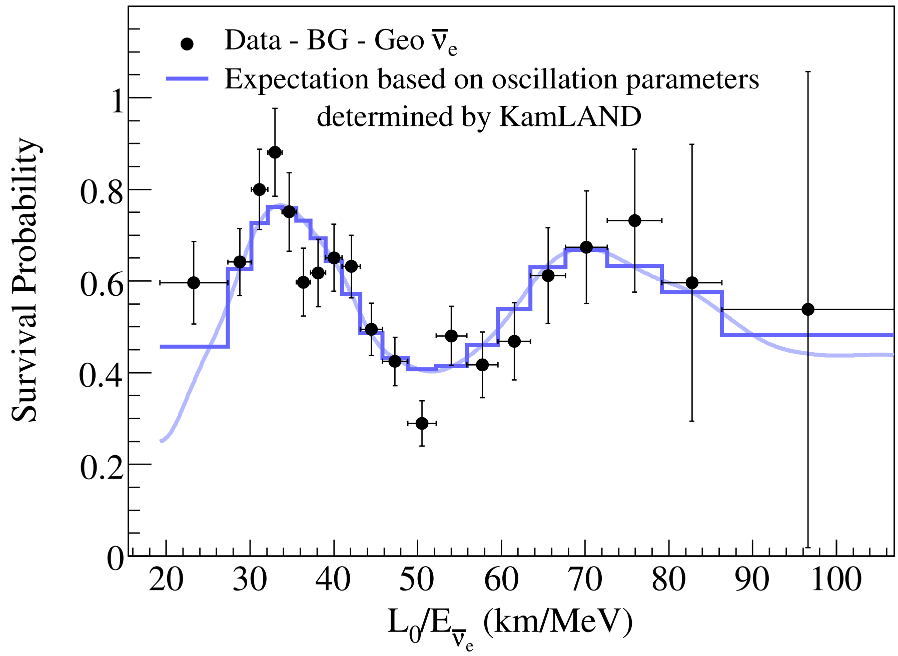

Figure 1.5: **The Observed $\bar{\nu}_e$ spectrum L/E and the expectations for the neutrino oscillations in KamLAND** [32].

The present experimentally collected data can be understood in the 2ν-flavor framework, neglecting the third angle parameter, θ_{13}. This fact is based mainly on the result of CHOOZ experiment.

CHOOZ was located at 1050 m away from two nuclear reactors which provide a total thermal power of 8.5 GW.

CHOOZ measured a normalized reactor neutrino flux of $1.01 \pm 2.8\,(\text{stat.}) \pm 2.7\,(\text{syst.})$, in concordance with the no oscillation expectations. In addition, the antineutrino energy spectrum shows no distortion [33].

1.5 Neutrinos Experiments Using Accelerators

Following the reaction chain described by relations (1.10, 1.11, 1.12), a neutrino beam can be produced from the decay of pions. The oscillation searches can investigate ν_μ disappearance, or the appearance of ν_τ or $\bar{\nu_e}$. The electron antineutrinos are detected via inverse β-decay following same procedure as in the case of the reactor antineutrinos.

Depending on the distance traveled by the neutrino beam before reaching the detector, the accelerator experiments can be divided in:

experiments at long baselines have typically distances of hundreds of kilometers between source and detector and can address atmospheric parameters range. The results from MINOS [38] and K2K [35] experiments shows a clear correspondence with the atmospheric neutrino data. Moreover, using a controlled neutrino beam, the long baseline experiments increase the precision of atmospheric oscillation parameters.

experiments at short baselines have typically distances of hundreds of meters between source and detector and can address both, the solar and the atmospheric oscillation parameters space. These experiments showed no evidence in their oscillation searches, with a notable exception given by the LSND experiment [28]. The best fit of the LSND data shows a mass parameter $\Delta\mathrm{m}^2$ which is incompatible with the atmospheric or solar findings. This fact implies the possible existence of "sterile" neutrinos, as the number of the "active" neutrinos is limited to three based on LEP experiments. However, the LSND result has not been confirmed by KARMEN [36] experiment and by the currently running MiniBooNE [37] experiment at Fermilab.

1.6 Summary of Experimental Results

The experiments measuring solar and atmospheric neutrino fluxes show clear evidence in flavor of the oscillation hypothesis. The same conclusion is reinforced by experiments which use man-made neutrinos. All available experimental data are processed in "global analysis" resulting in best fit values of the oscillation parameters.

In this thesis, the results from reference [40] will be presented, as this analysis contains the latest published MINOS results.

The present constraint on the solar mixing parameters is given by complementary measurements of solar neutrino experiments and KamLAND:

$$\Delta m^2_{12} = 7.65^{+0.23}_{-0.20} \times 10^{-5} eV^2 \ , \quad sin^2\theta_{12} = 0.304^{+0.022}_{-0.016} \quad (1\sigma \text{ errors}) \qquad (1.28)$$

On the other side the atmospheric and accelerator experiments provide information correlated with the atmospheric parameters:

$$|\Delta m^2_{31}| = 2.40^{+0.12}_{-0.11} \times 10^{-3} eV^2 \ , \quad \sin^2\theta_{23} = 0.5^{+0.07}_{-0.06} \quad (1\sigma \text{ errors}) \qquad (1.29)$$

The "last" oscillation parameter, namely θ_{13}, is presently not known. A strong constraint is given by contributions from all the previously mentioned experiments, in particular CHOOZ:

$$\sin^2\theta_{13} \leq 0.04 \quad (2\sigma \text{ errors}) \qquad (1.30)$$

The global analysis from reference [40] provides not only a constraint on θ_{13} but also the "best fit value". This is:

$$\sin^2\theta_{13} = 0.01^{+0.016}_{-0.011} \qquad (1.31)$$

The value from (1.31) is inside the sensitivity range of next generation of reactor neutrino experiments. Of course, new neutrino data from the current experiments could modify this presumption. In chapter (2) it is shown that, in its second phase, the Double Chooz experiment can measure θ_{13} values having $\sin^2\theta_{13} \gtrsim 0.006$.

The contributions of different neutrino experiments regarding the oscillation hypothesis are summarized by figure (1.6). Here, the allowed or excluded regions are provided in the parameter space of neutrino oscillations.

1.7 Open Questions

Despite the huge effort done in understanding the neutrino phenomenology, some questions still remain. These are the main tasks for the future experiments:

- The values of the mixing parameters need to be measured with higher precision, specifically, the value of θ_{13}. This unknown parameter is the target of the future reactor experiments. For a θ_{13} value smaller than the sensitivity of the reactor neutrino experiments, the future detectors using accelerators will address this task. Depending on the value of the θ_{13} parameter, future accelerator experiments could also address the CP violation phase.

- The absolute neutrino masses and the sign of Δm_{31} are not known. These tasks can be addressed by the measurement of neutrinoless double beta decay and by accelerator neutrino experiments.

- Also, we do not know if the neutrinos are Majorana or Dirac particles. This puzzle can be resolved by a positive evidence of a neutrinoless double beta decay.

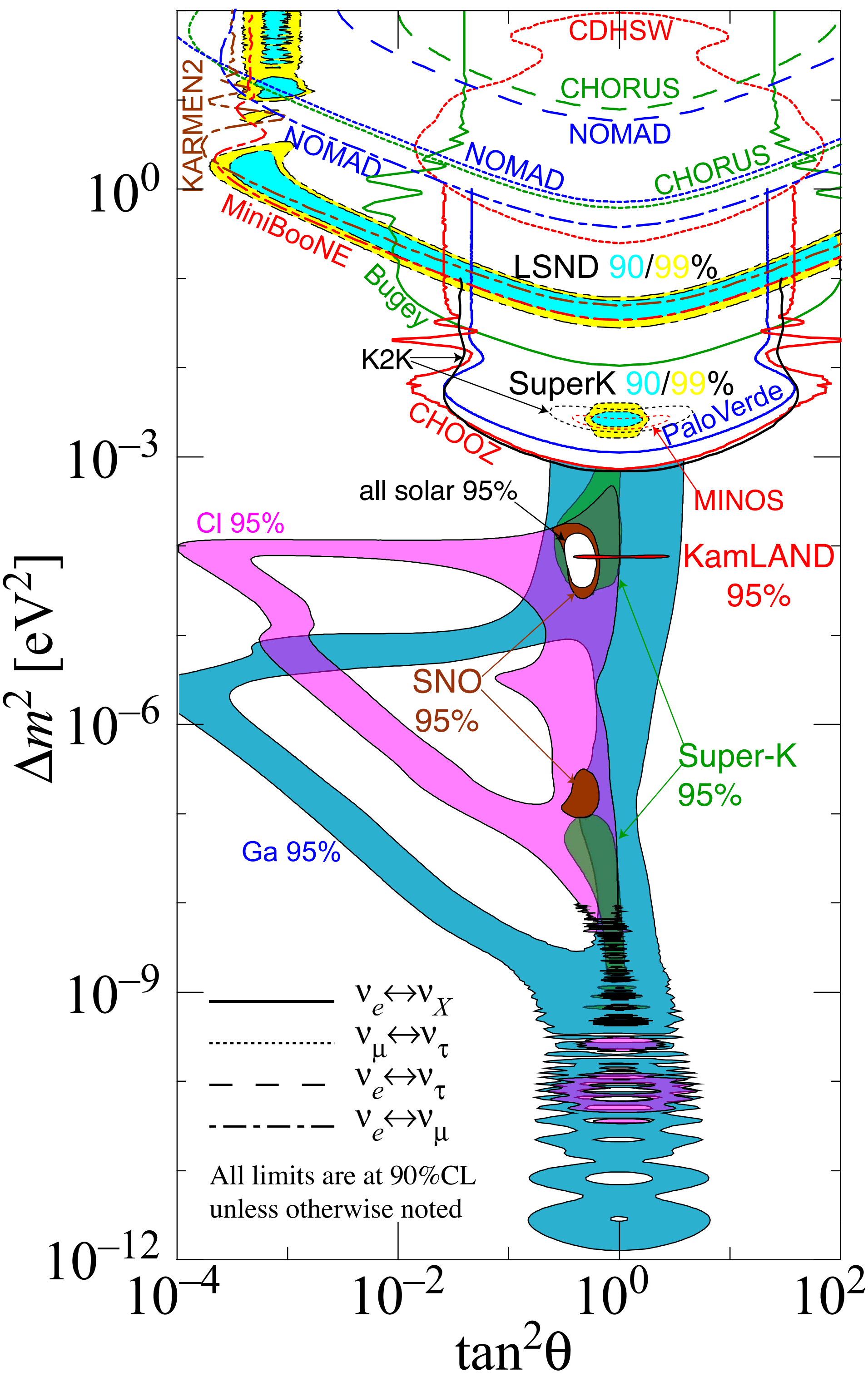

Figure 1.6: **Summary of current knowledge of neutrino oscillation parameters.** The colored regions are allowed regions for the oscillation parameters. White regions demarcated by a line are excluded regions. The line pattern shows the oscillation channel [34].

Chapter 2

The Double Chooz Experiment

2.1 The Double Chooz Concept

The Double Chooz experiment has been designed to search for the disappearance of electron antineutrinos. The investigated flux is provided by two reactors of the EDF-Chooz nuclear power plant. Each Chooz reactor has 4.27 GW power at an average duty factor of 80%.

Double Chooz aims for a θ_{13} measurement limited at $\sin^2 2\theta_{13} < 0.025$ in 5 years of data taking. It is almost one order of magnitude below the present limit[1]: $\sin^2 2\theta_{13} < 0.17$ given by the CHOOZ experiment. Double Chooz represents a collective effort of a multinational collaboration counting more than 120 physicists from 26 institutes and universities (see list in reference [42]).

In order to achieve its goal, the Double Chooz experiment foresees a significant decrease of systematic uncertainties as compared to CHOOZ experiment. The reduction of the sum of systematic errors below one percent is highly desired [42]. As a consequence, the Double Chooz experiment uses two similar detectors at different distances, a so called **"Near"** detector at ~ 400 m and a so called **"Far"** detector at 1050 m from the reactor cores. In fact, the near detector provides an unoscillated reference for the antineutrino flux and spectrum measured by the far detector. In conclusion, the far detector is sensitive to antineutrino oscillations due to θ_{13}.

The experiment's site is situated in the Ardennes mountains, close to the french-belgian border (figure 2.1). An important advantage of this location is given by the

[1] following direct measurements

possibility to re-use the facilities of the CHOOZ experiment for the far detector. The existing experimental hall (figure 2.2) is located underground, with a rock overburden corresponding to 300 meters-water-equivalent [2] (m.w.e.). The near detector site will be located at the bottom of a 56 m shaft, with ~ 140 m.w.e. overburden.

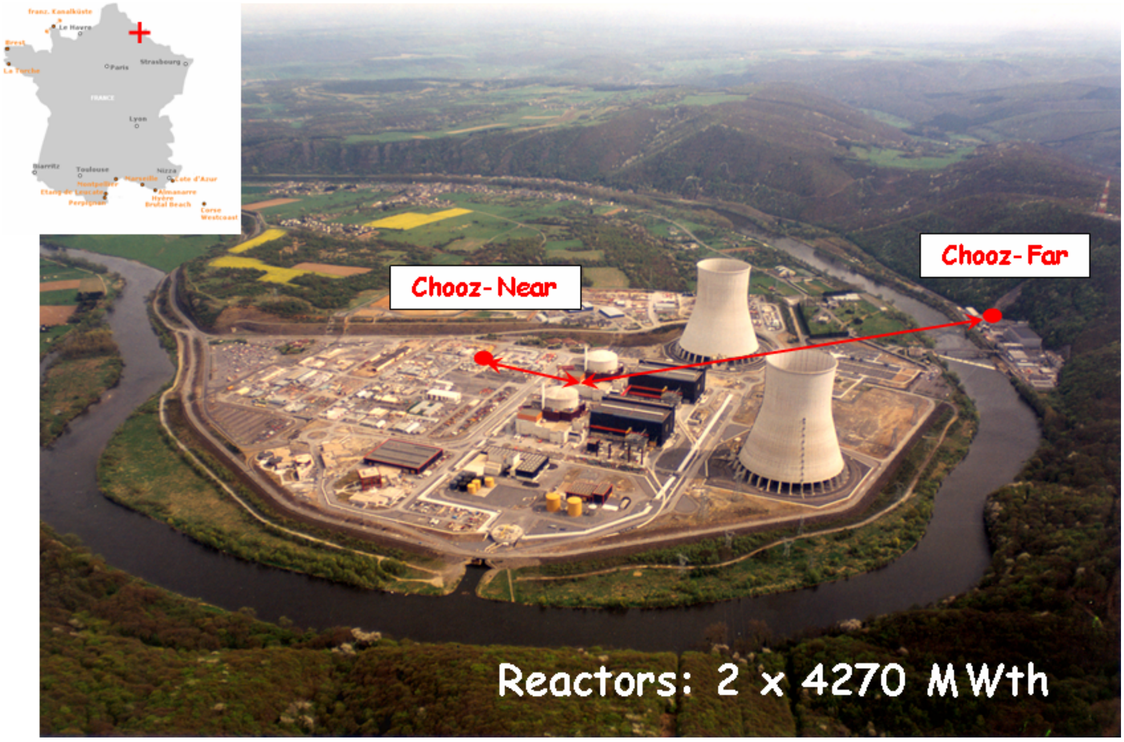

Figure 2.1: **An overview of the Double Chooz experiment site.** In the upper left corner the site is shown on a map of France [42].

The Double Chooz sites fulfill additional required conditions, e.g. a minimum distance from reactor cores and equal antineutrino fluxes from both reactors.

The main benefit of a multi-detector experiment like Double Chooz is the cancellation of reactor-induced systematic errors, remaining only the parameters involved in the relative normalization between detectors. Examples of such parameters are: the number of free protons in target or the distance between the detectors locations and the "barycenter" of neutrino emission in the cores. There is a huge progress in the uncertainties reduction with respect to CHOOZ [44, 42].

For now, a 0.6 % relative normalization error between the Double Chooz detec-

[2] This unit of overburden is introduced in order to facilitate the comparison between various underground sites. Equal overburden of two locations results in equal reduction of the cosmic ray flux.

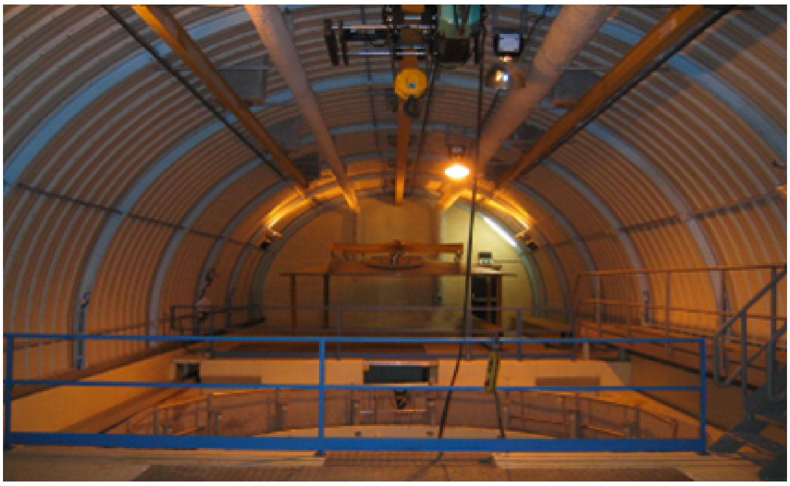

Figure 2.2: **Double Chooz far detector location**.

tors is assumed [42]. In order to reduce this normalization error, a considerable effort has to be put into reducing the differences between detectors.

Furthermore, the calibration system is a powerful tool against differences between the detector responses. For Double Chooz, radioactive sources, laser flashes and LED will be used for monitoring the detector parameters. For example, the scintillator aging effects or the relative efficiencies are important parameters to be calibrated.

2.2 The Detection Principle

For reactor neutrino experiments, the detection mechanism is based on delayed coincidence between inverse β-decay (relation 1.1 and figure 2.3) products. Usually, the fiducial target is a tank filled with liquid scintillator or water viewed by photomultiplier tubes. The photomultipliers measure the light released by scintillator from the energy depositions of the inverse β-decay products.

An event is characterized by two delayed energy depositions: The prompt energy deposition is the positron annihilation (relation 1.2) resulting in two 511 KeV gammas. The capture of the neutron represents the delayed energy deposition. The time difference between prompt and delayed events is given by the neutron thermalization and is $\sim$200 μs. Because of this characteristic time delay, most of the background can be discriminated.

The antineutrino energy is correlated to the prompt energy deposition, and can be directly measured using the following relations:

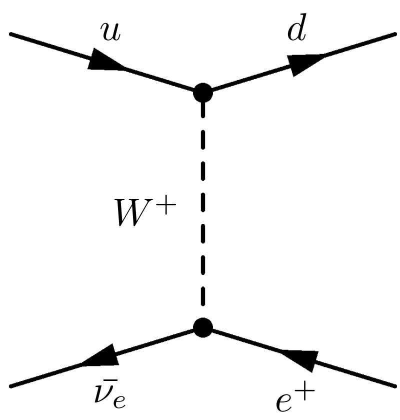

Figure 2.3: **Inverse β-decay.**

$$E_{vis} = E_{e^+} + m_e \tag{2.1}$$

$$E_{\bar{\nu_e}} = E_{e^+} + m_n - m_p \tag{2.2}$$

E_{e^+} is the sum of the rest mass and kinetic energy of the positron. The neutron recoil is neglected in previous relations. By replacing (2.2) into (2.1), one delivers:

$$E_{vis} = E_{\bar{\nu_e}} - E_{thr.} + E_{annih.} \approx E_{\bar{\nu_e}} - 0.8\,MeV \tag{2.3}$$

where $E_{thr.} = 1.8\,MeV$ is the inverse β-decay threshold and $E_{annih.} = 1.022\,MeV$ is the energy released by the positron annihilation. Relation (2.3) shows the correlation between the visible energy released and the antineutrino energy.

Double Chooz will use in its fiducial volume liquid scintillator doped with 0.1 % gadolinium. The neutron capture on Gd nucleus generates a cascade of 8 MeV gammas, far from the radioactive background.

2.3 Double Chooz Detectors

The Double Chooz detectors are designed to deliver high detection efficiency for antineutrinos as well as for background related events. The radioactive contamination havs a low level and the cosmogenic background is tagged.

An overview on the general design of Double Chooz detectors foresees concentric cylindrical volumes, (figure 2.4):

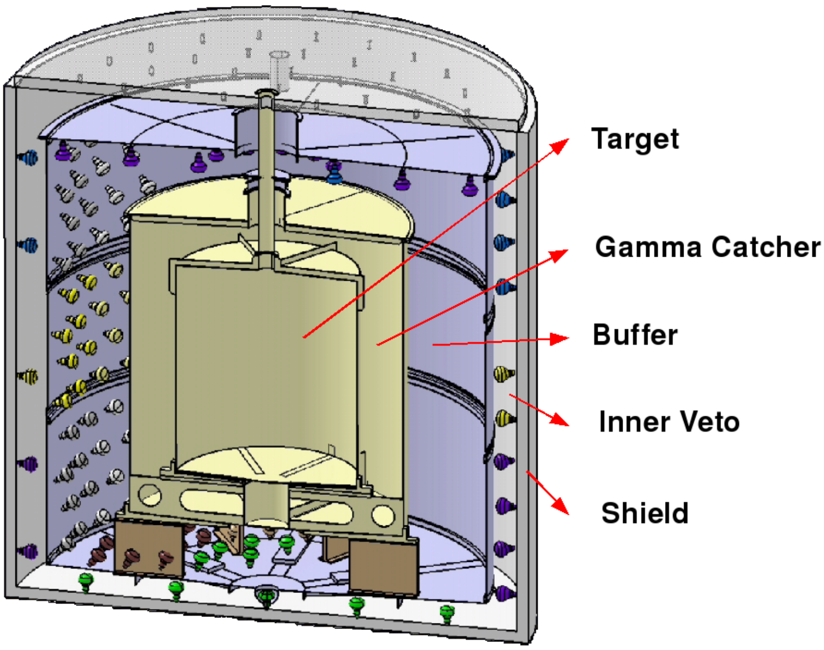

Figure 2.4: **Double Chooz detector - general design** [42].

2.3.1 General Mechanical Design

The Central Region is the most important part, aiming to detect antineutrino related energy depositions. It consists of two concentric vessels. The inner vessel is the **Target**. It contains 10.3 m^3 dodecane and PXE liquid scintillator loaded with Gd. The outer cylinder, named **Gamma Catcher** is filled with unloaded scintillator and aims to detect energy depositions which escape from the target. Both vessels are made of transparent acrylic material.

The target and gamma catcher cylinders are placed inside a stainless steel tank, which contains non scintillating dodecane and is called **Buffer**. The goal is the reduction of random background generated by the PMT glass. The central region of the detector is "seen" by 390 photomultipliers with 10 inches in diameter which are mounted to the walls of the buffer tank.

The Inner Veto is a 60 cm thick cylindrical region which enclose the central region. This volume contains unloaded liquid scintillator. The goal of this volume is to tag the muons which cross the detector. The energy depositions from the inner veto are observed by 78 photomultipliers, type 8 inches.

The Outer Veto and Shielding In addition to the inner veto, an external veto region, called **Outer Veto** is provided. It is placed above the main detector, and aims to tag the muons which pass near detector using plastic scintillator planes. In this way the spallation neutrons which migrate into the detector can be tagged. Moreover, the outer veto will improve the tracking capability for muons which cross the main detector. The outer veto can also detect muons which pass through the detector **Chimney**, and do not leave energy depositions in the inner veto. The chimney will be used for the deployment of the calibration sources inside the target volume.

The Double Chooz detectors will be covered with a layer of steel (figure 2.5), in order to decrease the influence of external radioactivity events.

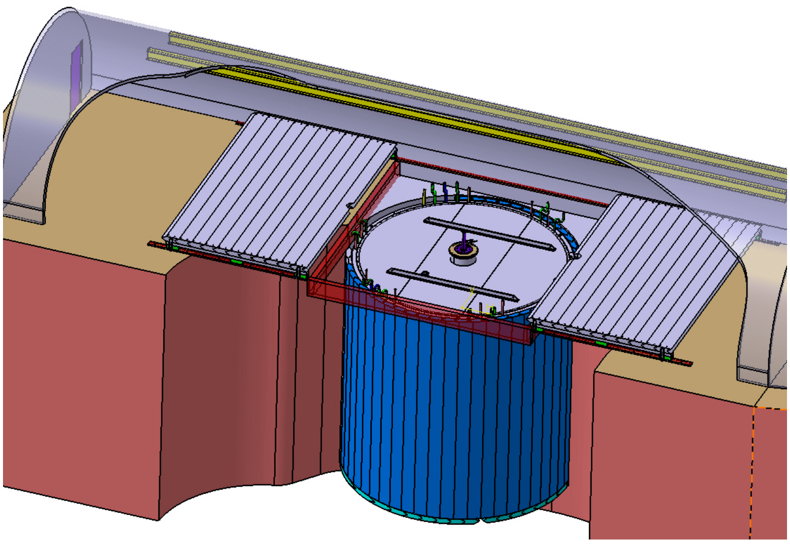

Figure 2.5: **The overview of the Double Chooz steel shielding** The top part contains two separate elements in order to facilitate the access at the inner detector [45].

2.3.2 The Electronics, Trigger and DAQ

The tasks of the Double Chooz electronics are related to the processing and distribution of photomultiplier signals. A simplified sketch of the overall system is shown in figure (2.6).

A single cable will carry the high voltage and the signal for each photomultiplier. This will reduce the space requirements as well as the ground-loop effects. The signal separation will be done with dedicated devices called high voltage splitters.

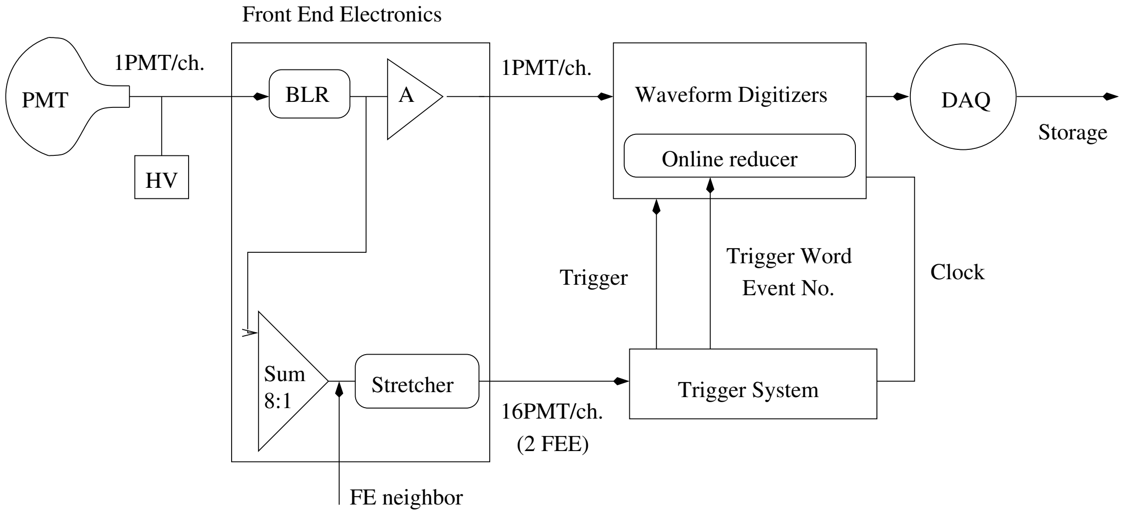

Figure 2.6: **A sketch Double Chooz electronics and DAQ**.

The front-end electronics (FEE) handle pre-amplification, filtering and baseline restoration of the photomultipliers signals. FEE use purely analog boards in order to prevent the digital crosstalk.

The FEE boards perform also the summation of 16 PMT channels followed by an analog stretching. These signals are the trigger inputs. The stretched signals have amplitudes proportional to their charge for a time window given by the stretcher time. As will be shown in chapter (5), the foreseen stretcher time is 60 ns. The trigger receives inputs from two FEE boards, this corresponds to a maximum of 16 photomultipliers.

The trigger is designed to be highly efficient for antineutrino and background events, at sub-percent precision. It will also distribute a common clock signal to the detector components and will provide a unique time stamp for each event. More details related to the trigger system will be discussed in the following chapters of this thesis.

The trigger readout is followed by the Online Data Reducer (ODR). ODR uses the trigger information to reduce the amount of data flow from the waveform digitizers to a rate which can be handled by the DAQ system. It also tags the delayed coincidence for antineutrino related events.

The pulse shapes of individual PMT are written to the memory of fast wave form digitizers (WFD). Double Chooz will use the model VX1724 [43], (figure 2.7) which has been developed by CAEN [3] in collaboration with Double Chooz.

[3]Costruzioni Apparecchiature Elettroniche Nucleari, Italy

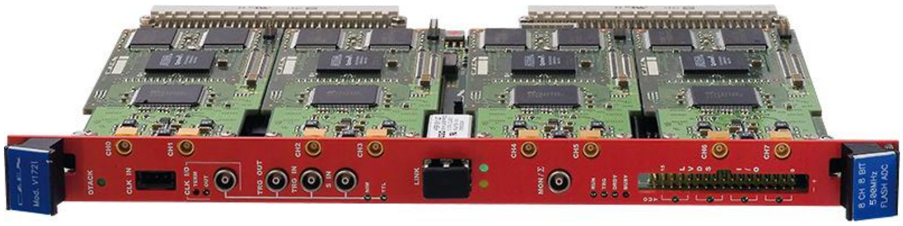

Figure 2.7: **The Double Chooz wave form digitizer: CAEN model V1721**[43].

The WFD are based on 8-bit Flash ADC (analog to digital converters) working at 500 MHz clock frequency. Using a smart memory control, the pulse shapes are recorded without dead time. This fact is possible if the available memory is structured in so called "pages". There are 1024 pages, each of them containing 1028 bytes. WFD record continuously the photomultiplier pulse shapes, until a trigger signal arrives. Then, the location where the future pulses are written is changed by incrementing the page index. In this way, the old data become available for a parallel read out and record. The overall memory can be considered as "circular" (figure 2.8).

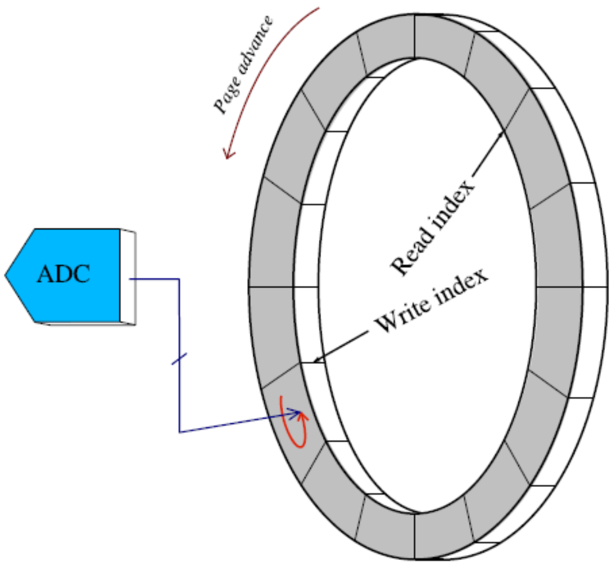

Figure 2.8: **The memory management of the Double Chooz wave form digitizer** [42].

2.4 Background in Double Chooz

A triggered event which does not respect an antineutrino signature, is identified as background. It has been shown that an inverse β-decay gives rise to a prompt signal in the range $\sim$1 to $\sim$8 MeV followed by an event identified as 8 MeV energy deposition for neutron capture on a Gd nucleus. For the selection of physics events, a coincidence window: $\tau_{coincidence} \simeq 200\,\mu$s is applied.

It is possible that a background event whose energy lies within the physics range, falls in the same coincidence window, thus creating **accidental background**. The producing rate of such events can be expressed as:

$$R_{accidental} \simeq r_{e^+} \cdot r_n \cdot \tau_{coincidence} \tag{2.4}$$

where, r_{e^+} is the positron-like event rate and r_n is the neutron-like event rate. The accidental rate can be measured by defining a coincidence window having the same width at a later time than the antineutrino related events.

Accidental background is created by radioactive elements present in the photomultiplier glass, surrounding rock, or construction materials. The decay chains of heavy elements such as U, Th and K create products with energies in the antineutrino range. These elements might also induce spontaneous fission reactions of the type (α, n). In this case, the resulting neutron, (after thermalization), can mimic the delayed physics event. One has to consider that a low radioactivity in the detector materials is a very important requirement for the detector design since it reduces considerably the background and in consequence, increases the detection sensitivity.

In addition, cosmic muons might produce fast neutrons, which after thermalization, can be captured by gadolinium nuclei. The neutrons are either produced by a spallation process or by muon capture on nuclei. The number of neutrons created via muon spallation is proportional to the muon flux.

A second category of background is represented by the **correlated background**. In this case, one event can mimic both parts of the coincidence signal. Through spallation of ^{12}C nuclei, cosmogenic muons produce fast neutrons and long-lived β-decaying isotopes such as ^{9}Li or ^{8}He. In a similar way, fast neutrons can be created in the surrounding rock of the detector. They might enter the fiducial region and, after multiple scattering on protons, can be captured, giving rise to a delayed signal. In this case, the prompt signal is given by the scattered protons. The correlated background is more critical because it cannot be directly measured;

it is possible only an estimation from the known production rates.

		DC-far	DC-near
Specifications	overburden [m.w.e.]	300	114
Muons	flux [Hz/m^2]	0.63	5.0
	mean energy [GeV]	63	34
	inner veto rate [Hz]	45.4	250
Neutrons	prod. rate in CR [Hz]	0.15	0.8

Table 2.1: **The Double Chooz cosmogenic background summary** [53, 31].

A summary of expected rates for accidental and correlated backgrounds for Double Chooz, is given in table (12) from reference [42]. The cosmogenic induced background rates, are shown in table (2.1).

To summarize, an efficient protection against muons and rock radioactivity is given by increasing the overburden size at the experiment sites, as this measure will decrease the flux and the mean energy of muons which cross the detector.

2.5 Calibration

The Double Chooz detectors are continuously monitored by the calibration system. The calibration tasks are multiple, including the estimation of the detection efficiency, or the monitoring of the scintillator stability. Double Chooz will use radioactive sources with energies in the inverse β-decays range, such as ^{252}Cf, AmBe, or ^{137}Cs. As the detection efficiency might depend on the event location inside detector, this parameter has to be checked for different calibration sources at different locations.

The Double Chooz calibration will use fast lasers with different wavelengths in order to extend the energy range of the radioactive sources. In this way, the characterization of detector response will be scaled to higher energies. Moreover, the light emitted by the lasers have precise timing and amplitudes and will be used for the calibration of the vertex reconstruction.

Another important task of the calibration is related to the trigger system. This includes the calibration of trigger thresholds and the estimation of the trigger efficiency. The details related to the trigger calibration strategy will be discussed in chapter (3).

2.6 Double Chooz Simulation Software

The effort made for optimization of the Double Chooz detector design is based on computer simulations. Nevertheless, the simulation software will play an important role during the data analysis phase.

Presently, the main Double Chooz simulation software, DCGLG4sim [42], is a GEANT4 based application containing models of the detectors components and related physics aspects. DCGLG4sim is based on GLG4sim [46], the Monte Carlo software used for KamLAND simulations.

Another program used by the Double Chooz collaboration is NuGen. NuGen is a generator aiming to simulate the reactor antineutrino flux and energy. The combination of DCGLG4sim and NuGen successfully simulates the detector response to reactor antineutrino events.

An significant part of the Double Chooz simulation effort is related to background modeling. The production and transport of cosmogenic muons is described by software based on FLUKA [48] and MUSIC [49] packages, containing details of the geological structure at the detectors sites. The outputs are used by DCGLG4sim. In this way, the detector response to cosmogenic background can be estimated.

Further, many other software modules have been added in order to provide a complete set of tools for the Double Chooz simulation and analysis. An easy way to plug all software modules together is given by a common software framework. For Double Chooz this is called "DOGS" and contains dedicated packages for the specialized tasks of the data simulation and analysis. The different components can interact and inter-change data. Within DOGS, there are the following packages:

DCAna is the basis for future data analysis software within the DOGS framework. Using DCAna, the user can access and process the simulated or experimental data.

DCEvent is the event data storage code. DCEvent is the core of the DOGS framework, as all the other applications interact with the same set of data. It contains data storage classes based on ROOT [47] libraries.

DCRoSS introduces readout simulation to the detector response. DCRoSS completes the detector simulation, implementing all Double Chooz electronic systems from the photomultipliers to the pulse shapes in the wave form digitisers. DCRoSS output data uses the same format as experimental data in order to facilitate the comparison. It also allows the implementation of possible detector imperfections, e.g. "hot" or "dead" PMT channels.

DCGLG4sim is the Geant4-based Monte Carlo simulation of Double Chooz. DCGLG4sim is the only program, within DOGS, which uses GEANT4 libraries.

DCCalib is the DOGS component which handles the detector calibration. DCCalib contains a set of calibration constants which will be measured with radioactive sources or laser flashes.

DCDisplay is the Double Chooz event display. It permits the visualization of different detector parts as well as physics events.

DCGeo handles the geometry of the detector components and the relative positions between them.

DCNuGen simulates antineutrino interactions, independent from the detector simulation. DCNuGen is able to manage any number of reactors of any power and any number of detectors at different positions. The normalizations of flux and target mass are automatically taken into account. An example of energy spectrum for the products from inverse β-decay, obtained with DCNuGen, is given in figure (2.9).

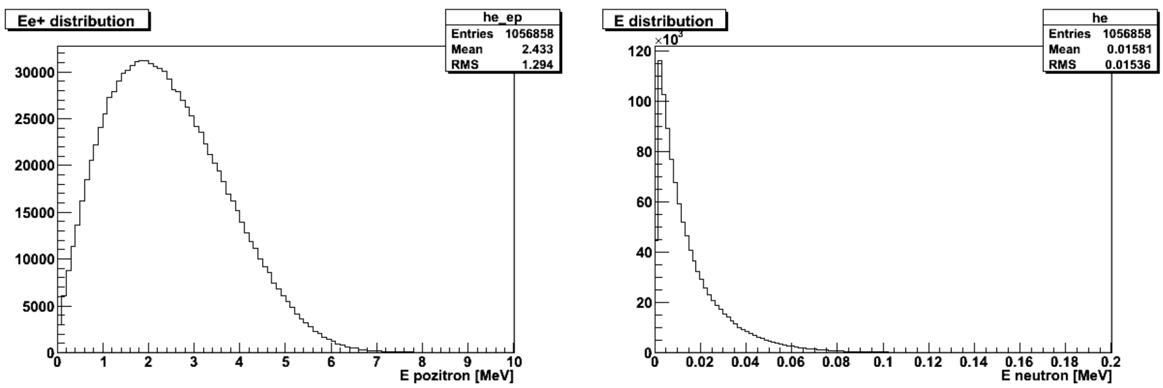

Figure 2.9: **Energy spectrum of the inverse beta decay products: positron (left), neutron (right)**.

DCReco is the event reconstruction code. It provides a common interface for algorithms which performs the time and charge reconstruction (DCRecoShape) and the spatial reconstruction (DCRecoBAMA, DCRecoMOSCOW).

2.7 Conclusions and Schedule

So far, the Double Chooz collaboration has made a considerable progress in the realization of the detector components.

The first data taking is planned for the fall of 2009. However, the existing infrastructure at the far site will split the data taking period in two phases. The first one will consider the far detector only followed a year and half later by a second phase when both detectors will be involved.

In short time, a considerable progress is expected, e.g. the CHOOZ θ_{13} limit can be surpassed in the first 2 months of data taking. The second phase will decrease the systematic uncertainty down to 0.6% (figure 2.10) and the sensitivity of $\sin^2(2\theta_{13})$ will be better than 0.025, which means an order of magnitude lower than the current limit.

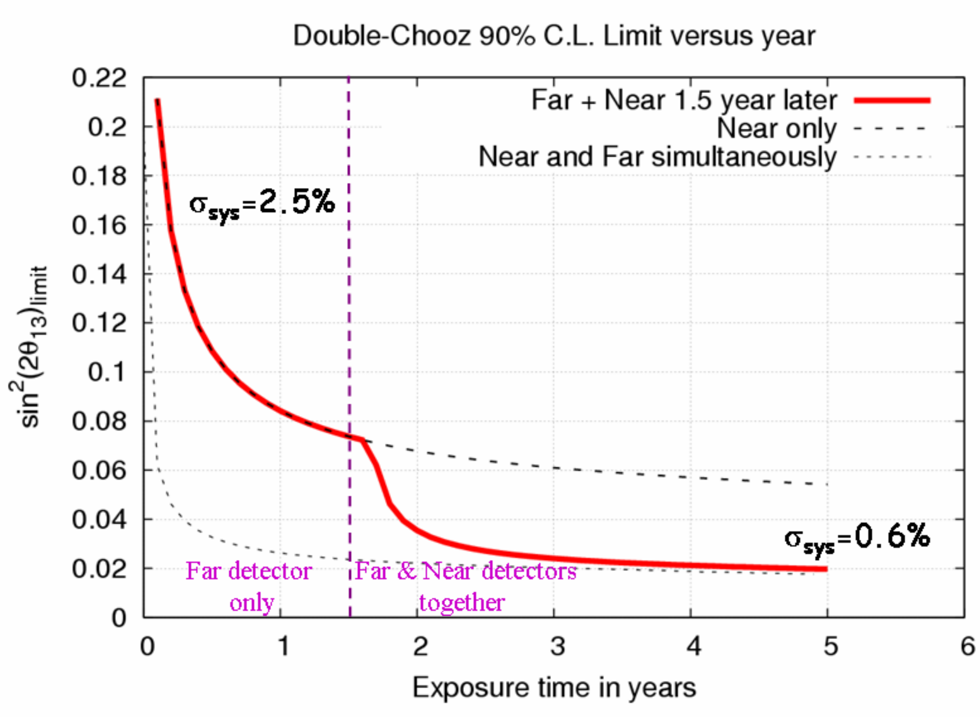

Figure 2.10: **The $\sin^2(2\theta_{13})$ sensitivity limit for the foreseen installation scenario.** For the first phase (∼1.5 years), only the far detector will be involved, meantime the construction of the near detector will be finalized. For the second phase (∼3.5 years), both detectors will be involved, thus the sensitivity can be improved [42].

Chapter 3

The Double Chooz Trigger

3.1 General Principles

For Double Chooz, the measure of the total energy depositions in the central region is given by the sum of the signals from the photomultipliers. The trigger system is designed to discriminate PMT summed signals by multiple thresholds, in order to create event classes. Starting from this general principle, the actual trigger design includes a muon recognition algorithm for the inner veto as well as protection against hardware failures.

The trigger receives stretched sum signals from the Front End boards and sends its output to the Waveform Digitizers (figure 2.6). The amplitude of the signals delivered by FEE boards for the trigger purpose is correlated with the charge of the PMT signals.

An overview of the trigger system is shown in figure (3.1). The trigger is a two level system. The first level is represented by the boards which process the information from central region and inner veto (TB-A, TB-B respectively TB-V). The second level is represented by the trigger master board which combines the information received from the first level boards and produces the trigger outputs:

Trigger word - is the summarized information of the conditions fulfilled by the triggered events.

Trigger number - is the output of the trigger counter. It is incremented for each triggered event.

Trigger - is a synchronous signal for each triggered event.

The internal logic of each trigger board is a logical "AND" of the following conditions:

The multiplicity condition requires a number of input PMT groups to have a signal above a given threshold called group threshold (figure 3.1). The inputs of the trigger boards are summed PMT signals from FEE boards.

The sum signal condition - is the discrimination by multiple thresholds of the sum signal of the trigger board inputs (figure 3.1). The sum of the trigger board inputs is a measure of the total energy released in detector.

The hardware implementation of the trigger boards foresees two group thresholds for each input and four sum signal thresholds. The multiplicity condition can consider individual inputs and/or partial sum of inputs, depending on the board algorithm.

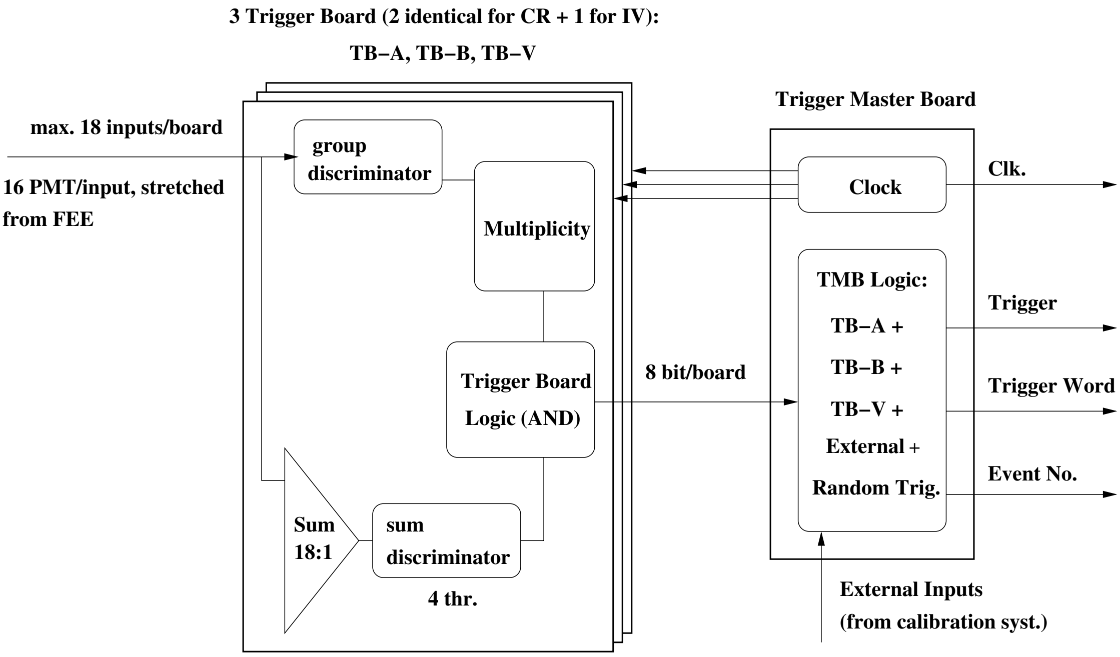

Figure 3.1: **The Double Chooz trigger system.** Two identical boards share the central region PMT signals (TB-A, TB-B) and one trigger board (TB-V) processes the inner veto PMT signals. The decisions of the boards are combined by the master board and sent to the DAQ system.

The trigger system design is based on **redundancy**. The processing of the central region PMT signals is done by two independent trigger boards (TB-A and

TB-B in figure 3.1) having identical discriminator levels and logic. The final trigger decision is build as a logical OR from the decisions of the central region boards and the information from the inner veto board. Using this approach, the hardware failures of the trigger system will not result in loss of events. As it will be shown in chapter (5), the trigger efficiency is still high for the physics energy range even if only one of the central region boards is considered. Two independent trigger decisions permit the estimation of the trigger efficiency from offline data following the procedure described in chapter (5). In addition, the redundancy enhances the robustness of the trigger system, the decisions of the central region boards can be crosschecked.

Another characteristic of the trigger boards logic is the use of **multiplicity**, as a measure against single noisy photomultipliers. The multiplicity condition is set to "$\geqslant 2$" trigger inputs and a very low group threshold (0.25 p.e/PMT). As will be shown in chapter (5) for this set of values, the trigger efficiency is not influenced by the multiplicity condition.

FPGA[1] chips are used to implement the trigger system logic. The **flexibility** provided, can be useful when the conditions "in situ" are not in the range predicted by simulations. The FPGA chips can accommodate complex algorithms due to their large memory.

An additional task of the trigger system is to provide a **common clock signal** for the electronic components. The clock frequency is 62.5 MHz, corresponding to a time stamp resolution of 16 ns. There will be independent clocks for far and near detectors, both using GPS[2] signals for absolute time calibration. The absolute time reference is used for the inter-detector synchronization and optionally for the study of supernova events [50].

The trigger system decisions are transmitted to the Online Data Reducer (ODR) which creates the delayed coincidence between the antineutrino-like events and processes the Waveform Digitizers data for the background events. The ODR is a software component of the Data Acquisition System (DAQ) and is justified by the limitations of the DAQ rate [51]. For the background events, ODR reduces the amount of saved data to a summary. For the antineutrino-like events as well as for some categories of background, all the extended information will be available offline.

The photomultipliers signals arrive to wave-form digitizers and trigger after

[1]Field Programmable Gate Array
[2]Global Positioning System

~ 300 ns with respect to the interaction time. This time interval is given by the transit time of the PMT, the cable lengths, and the time of flight inside the detector.

The time of the trigger decision establishes the event window for the pulse shapes data inside WFD (figure 3.2). The event window has a fixed width for physics events, for example 256 ns. In order to include the first part of the pulse shapes (before the time of the trigger decision), the trigger signal is delayed inside the WFD. For physics events, the PMT pulse shapes included in the event window are stored.

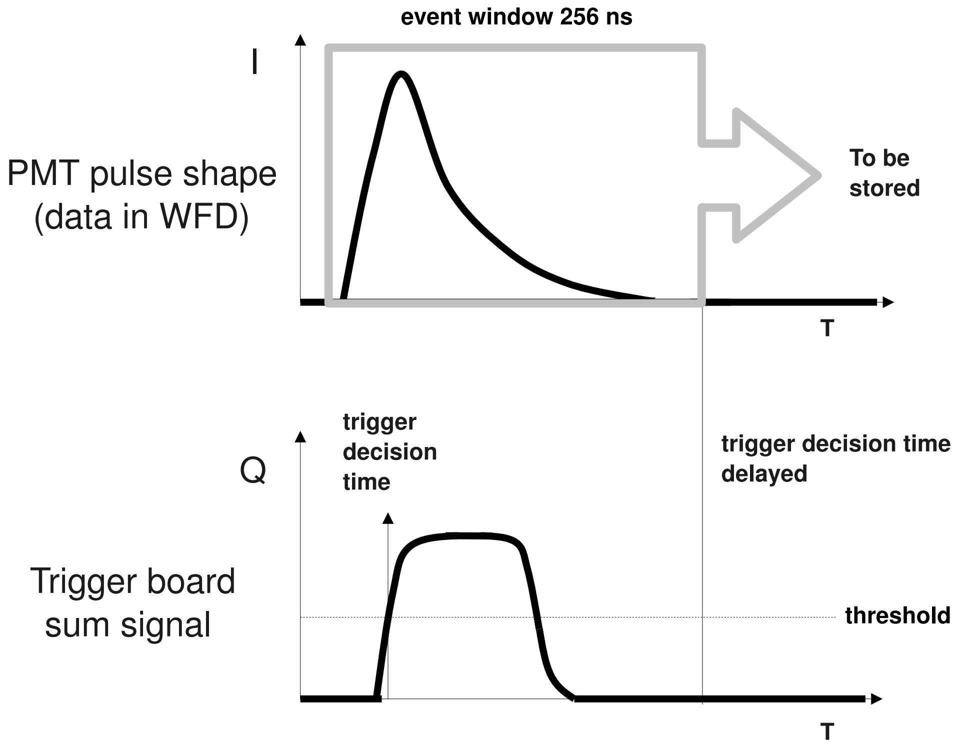

Figure 3.2: **The definition of the event widow using the trigger tag synchronization.** The trigger tag time is the time when the trigger word and the trigger are available.

3.2 The Trigger Event Classes

The event classes are based on multiple discrimination of the PMT sum signals and aim to clarify the physics as well as the background events. As described previously, the correspondence with the deposited energy is ensured by the front-end boards. There are four thresholds related to events in central region: 0.3 MeV, 0.5 MeV, 5 MeV and 50 MeV and 2 sum thresholds for the discrimination of the inner veto signals. The main trigger threshold corresponds to the physics events and is 0.5 MeV. The inner veto event classes which aim to identify background muons, require information from all the detector volumes.

The summary information on the trigger event classes is transferred in a binary form by a trigger word.

3.2.1 Central Region Event Classes

Central region single $\boxed{\mathrm{E_{CR}} > 0.5\,\mathrm{MeV}}$ Here, the focus lies on positrons from inverse β-decays and neutrons captured on free protons.

Central region low energy $\boxed{\mathrm{E_{CR}} > 0.3\,\mathrm{MeV}}$ The low energy threshold provides a way for the trigger efficiency measurement. This procedure is described in chapter (5).

Central region neutron $\boxed{\mathrm{E_{CR}} > 5\,\mathrm{MeV}}$ This class selects the inverse beta decay neutrons captured on gadolinium and background neutrons.

Central region muon $\boxed{\mathrm{E_{CR}} > 50\,\mathrm{MeV}}$ This class will include cosmogenic muon events and high energy depositions by background neutrons.

3.2.2 Inner Veto Event Classes

The trigger conditions along with more details on the inner veto events, will be presented in chapter (5). The inner veto muon classes are identified by the muon pattern recognition algorithm, also presented in chapter (5).

Inner veto passing muon The passing muons create energy depositions only inside the inner veto.

Inner veto crossing muon The crossing muons leave energy depositions in all detector volumes, having two separate paths inside the inner veto.

Inner veto stopping muon The stopping muons stop in one of the central region components, and have one path inside the inner veto.

Inner veto neutron The main contribution is given by the neutrons created in the surrounding rock of the detector by cosmogenic muons.

3.2.3 External Event Classes

The trigger master board can accommodate up to eight external inputs (figure 3.6). This is a convenient implementation of calibration triggers. With respect to the PMT signals, the calibration signals reach the trigger system earlier, due to differences in cable lengths. This inconvenience is remedied using a programmable delay line implemented in the master board.

3.2.4 Special Event Classes

Random trigger The random trigger is set to a fixed frequency. The rate will be established between 1 Hz and 0.01 Hz, depending on the value of the low energy background at the detector site. There is no correlation between these trigger signals and physics events. The random trigger offers an alternative way for the measurement of background and trigger efficiency.

Close-in-time trigger This trigger is generated if the time difference between two consecutive trigger signals is smaller than the event window. The Close-in-time triggers are used for the identification of pile-up events.

Follow-up trigger Complementary to the previous case, a follow-up trigger is generated if the trigger conditions are fulfilled for more than the event window time. Typically, background muons can generate large signals, exceeding the event window.

3.3 The Trigger Rate

There are two main components of the trigger rate. At low energies, the main contribution is given by background produced by radioactive elements which are present in the detector materials, especially in the cathode glass of the photomultipliers. At higher energies, the trigger rate is dominated by cosmogenic muons. Other contributions have smaller rates [51] and can be neglected.

The low energy background can be estimated using figure (3.3) having the detector dimensions from reference [42]. The anticipated trigger rate for the central region is 20 Hz.

The muon flux will be higher at the near site than at the far site due to the differences in the corresponding detectors overburdens. The predicted muon rate at the inner veto is 45.4 Hz for the far site [52] and 250 Hz [53] for the near site.

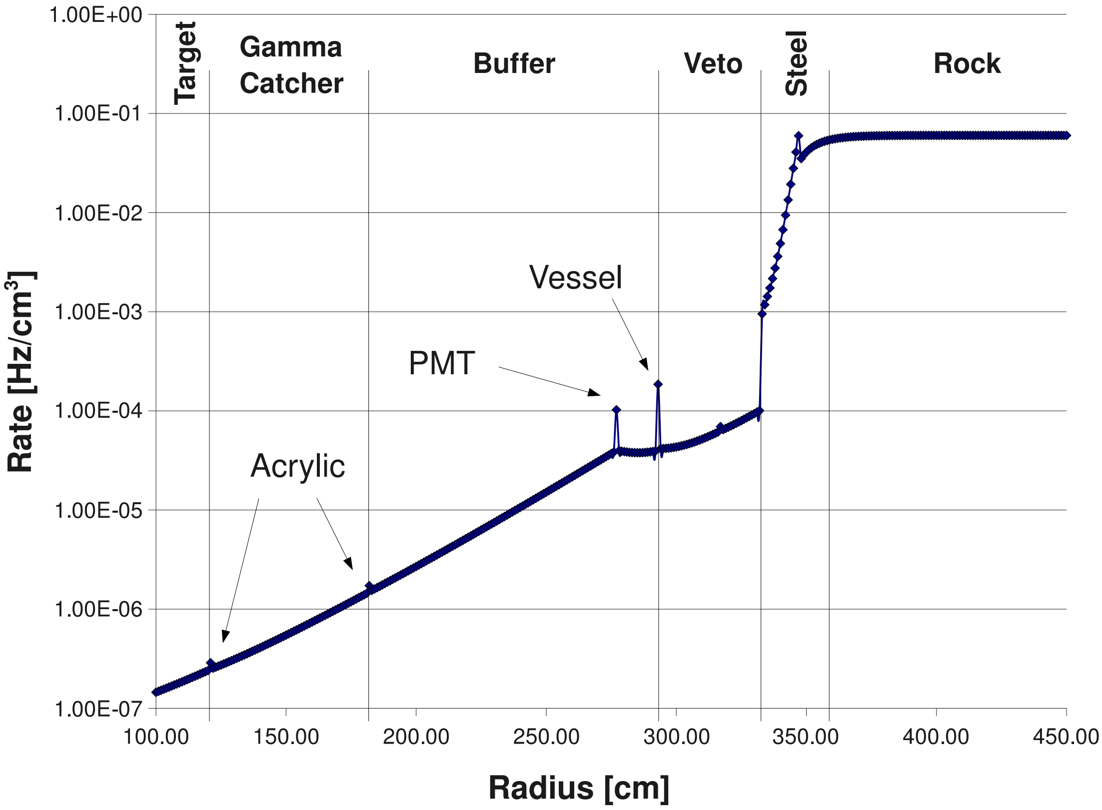

Figure 3.3: **The predicted low energy background rate as function of the distance from the center of the detector** For this simulation a spherical detector geometry is considered [42].

In conclusion, one can anticipate a trigger rate R $\simeq$ 66 Hz for the far detector and R $\simeq$ 270 Hz for the near detector.

3.4 Hardware Implementation

The hardware of the Double Chooz trigger is designed as VME[3] modules based on FPGA chips (figure 3.4). The FPGAs are reconfigurable (i.e. programmable) circuits used for the implementation of complex algorithms. The Double Chooz choice is the chip XC2V500 produced by Xilinx Inc. It provides 500 kB of memory, structured in 768 logic blocks and 172 Input/Output ports.

Figures (3.5) and (3.6) show a schematic view of the inner structure of the FPGAs involved in the trigger system. The main firmware component is the trigger logic unit. In total, there are 40 inputs to the logic units: 36 group discriminators

[3] VERSA-Module Eurocard

and 4 sum channel discriminators. The logic unit of the trigger master board receives inputs from trigger boards and the calibration system (external).

Additionally, the FPGA chip contains hardware structures for monitoring and diagnostics such as the rate monitors for the main inputs and outputs (figures 3.5 and 3.6).

All hardware components of the trigger system communicate with the data acquisition system through the VME bus. Therefore, each trigger board contains a PLD[4] chip for the processing of the VME operations. The role of PLD is to provide an interface between FPGA and VME. It also acts as a buffer for the FPGA data during the transmission via the VME bus.

The trigger boards contain an analog interface which receive the front-end signals. The analog part is based on the input discriminators. When analog and digital chips share the same PCB[5], a major concern is caused by influences on the analog signals, induced by the digital components. In such cases, a good strategy is a good separation between the involved parts.

The main task of the trigger master board is to summarize the information received from the trigger boards and the external inputs into a trigger word. It also contains a random trigger generator and a clock generator. The trigger word is delivered to the trigger system output after a logic AND with the trigger mask. The trigger mask allows the selection of subsets of triggers.

The trigger master board is entirely digital, and thus not affected by internal crosstalk.

The total power consumption of the trigger system is 62 W [41].

---

[4] Programmable Logic Device

[5] Printed Circuit Board

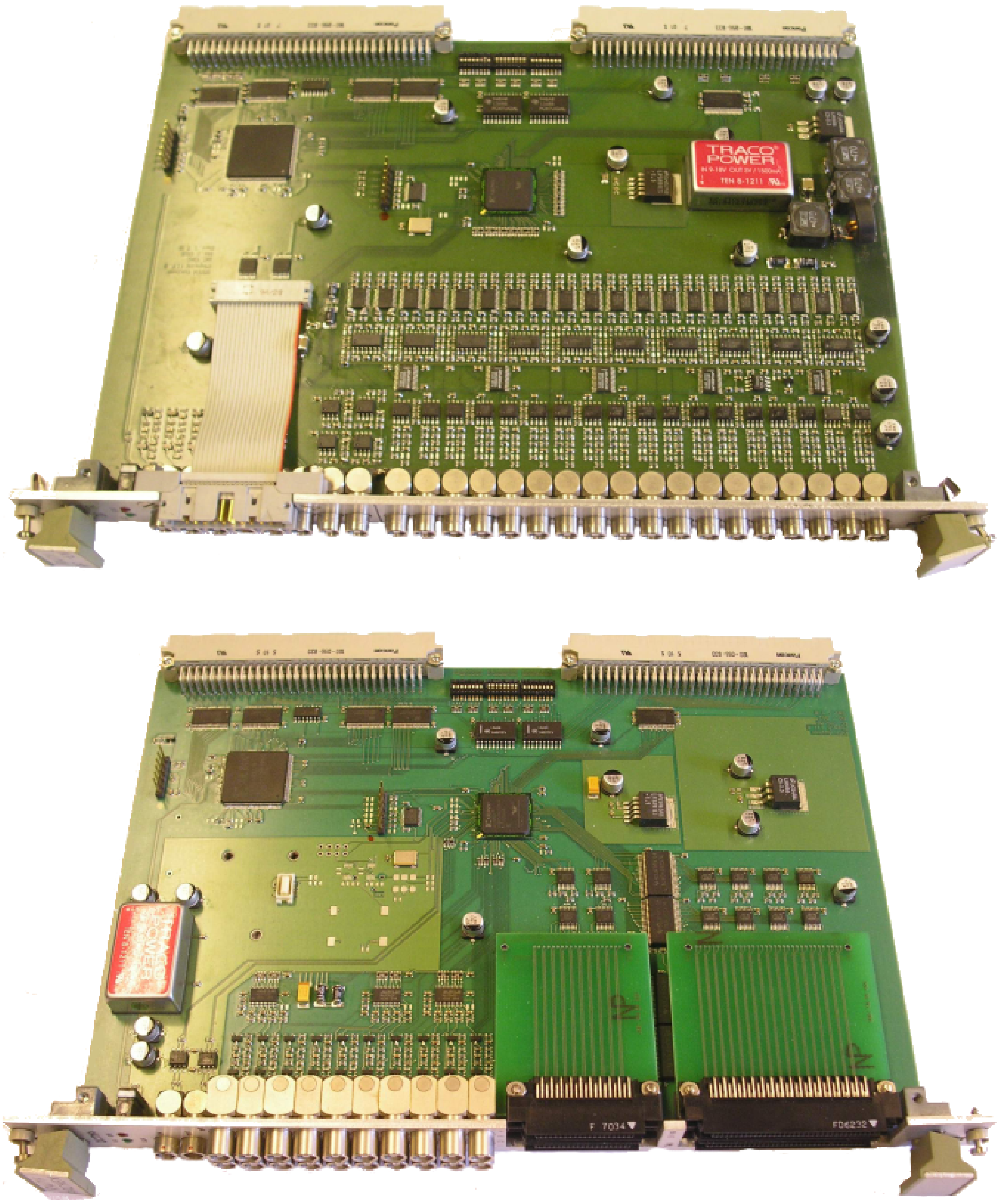

Figure 3.4: **The hardware implementation of the Double Chooz trigger system: trigger board (top) and trigger master board (bottom).**

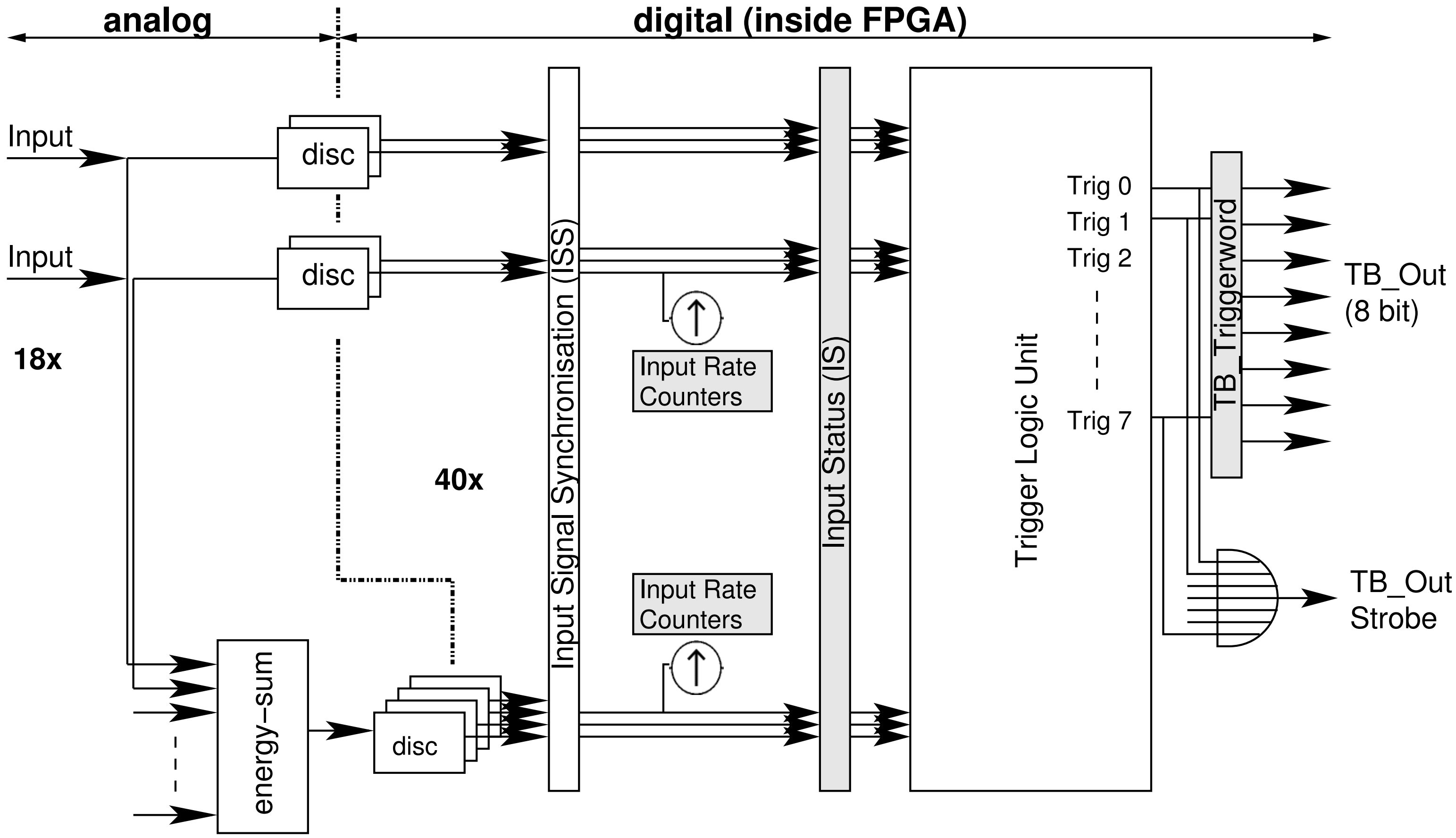

Figure 3.5: **Trigger board logic.** The inputs are connected to the front-end boards; the output information is processed by the trigger master board [54].

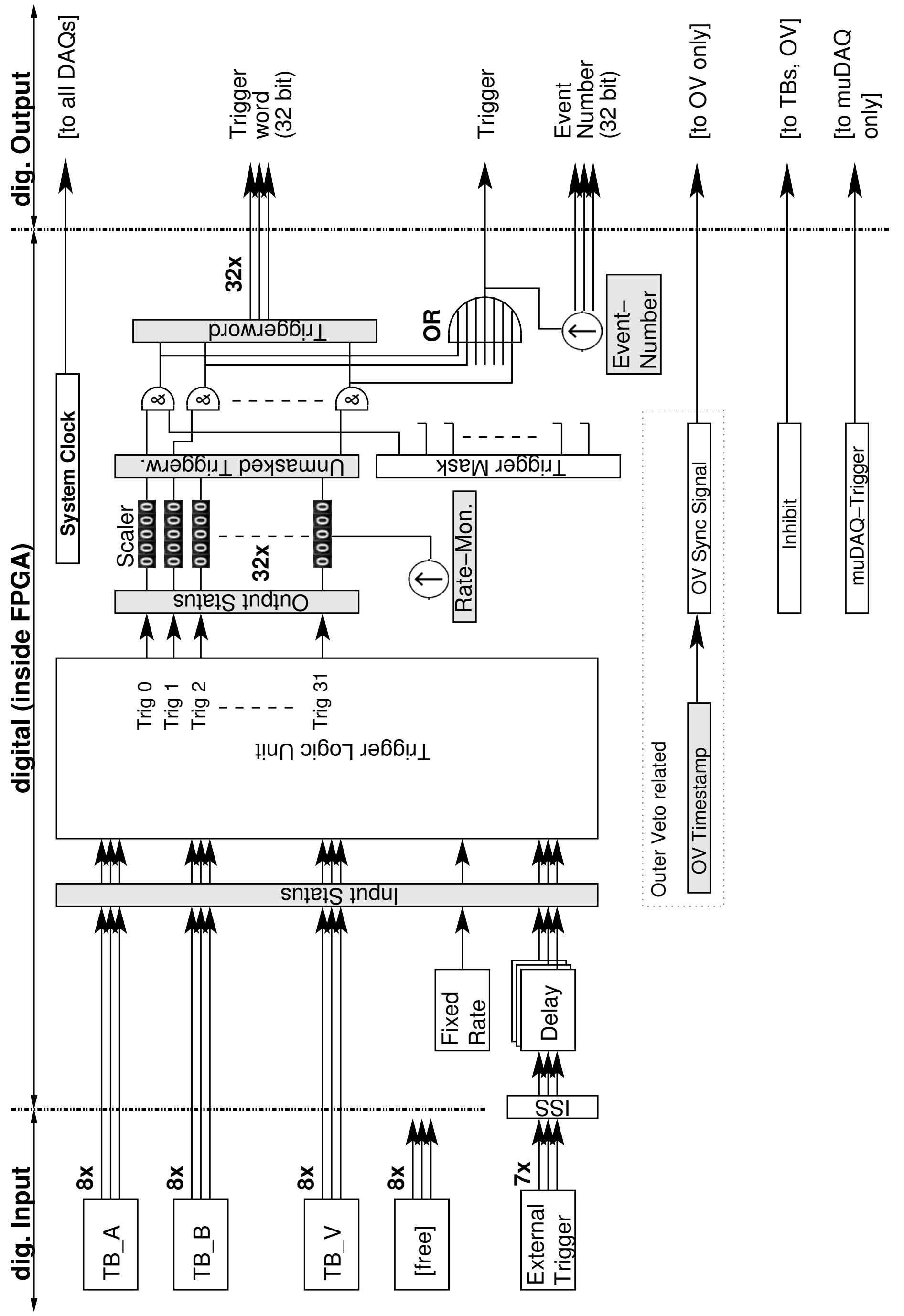

Figure 3.6: **Trigger master board logic** [54].

3.5 The Trigger Data

The trigger system has to be continuously monitored for the immediate detection of hardware failures. In addition, the trigger monitoring provides important information concerning the detector response such as the rate of PMT groups.

The information provided by the trigger system (the grey boxes in figures 3.5 and 3.6) can be divided into the following three categories:

Event-wise data is read out for each triggered event. This category includes the most important trigger parameters, such as the binary "words" of all trigger boards and the event timing. The event-wise data set is related to the following parameters:

Trigger word (32 bit) contains information on fulfilled trigger event classes.

Event number (32 bit) is a counter whose value is increased with each triggered event.

Trigger time (32 bit) is the time of the trigger decision. As described in this chapter, an absolute time reference based on GPS-clock will be used.

Trigger delta time (32 bit) is the time difference between two consecutive trigger times.

Input status trigger boards (120 bit) represents the status of the trigger board discriminators.

Input status master board (32 bit) is the status of the master board inputs, meaning the trigger board words and the external inputs.

Output status master board (32 bit) represents the output of the trigger master board logic: unscaled and unmasked trigger word.

Unmasked trigger word (32 bit) represents the trigger word before the application of the trigger mask.

Outer veto counter (32 bit) is the status of the counter used for the synchronization of the inner detector with the outer veto. A similar counter is placed inside the outer veto electronics. These two counters exchange synchronization signals as is shown in figure (3.6).

Run-wise data is read out one time for each run. It includes the following parameters:

- **Trigger thresholds** The entire set of the trigger thresholds for all the boards will be saved at the start of each run.
- **Trigger masks** The trigger mask will be applied to the trigger word and will be saved at the start of each run.
- **Down-scale factors** The values used by the trigger master board are saved at the start of each run.
- **Parameters of the trigger logic** It represents the description of the algorithms running on each trigger board.

Monitoring Data is used for trigger monitoring. The rates of input signals will be continuously monitored at time periods of the order of 1 s to 100 s. This information is read out, in a compressed form, one time for each run and includes the data from rate monitors of each input discriminator and all trigger outputs.

Overall, the most significant contribution to the trigger data is given by the event-wise data, $\sim$48 B/event. Considering the trigger rate at the Double Chooz near detector (section 3.3), it results $\sim$1.2 GB in 24 hours of saved trigger data. For the far detector, the amount of saved trigger data is considerably lower.

Chapter 4

The Grouping of the Photomultipliers

4.1 Introduction

As it was presented in chapter (3), the Double Chooz trigger uses two independent boards which analyze the energy depositions from the central region. The PMT sharing between these boards might influence the trigger efficiency. The grouping scheme of photomultipliers related to the trigger boards is optimized for the trigger algorithm and it is based on simulation studies described in chapter (5).

In addition, the PMT grouping scheme has to take care of influences from high voltage splitters and constrains from PMT cable routing. The front end electronics design considers a maximum of 16 PMT/FEE board, for each trigger input [45]. In order to reduce the costs, a maximum occupation of the front end boards will be performed. This is suitable only for the central region, for inner veto, the implementation of the muon recognition algorithm (described in chapter 5) requires a smaller number of photomultipliers per trigger input.

One might consider two points of view for the PMT grouping:

Macro-grouping is the overall selection of the central region photomultipliers which are connected to one or another trigger board (figure 4.1). For the actual configuration, there are 390 central region photomultipliers divided in two halves, each half corresponding to one trigger board. For inner veto, all the photomultipliers are connected to one board therefore macro-grouping is not relevant.

Micro-grouping is the selection of the photomultipliers which are added together for each trigger board input channel. There are 18 inputs for each trigger board.

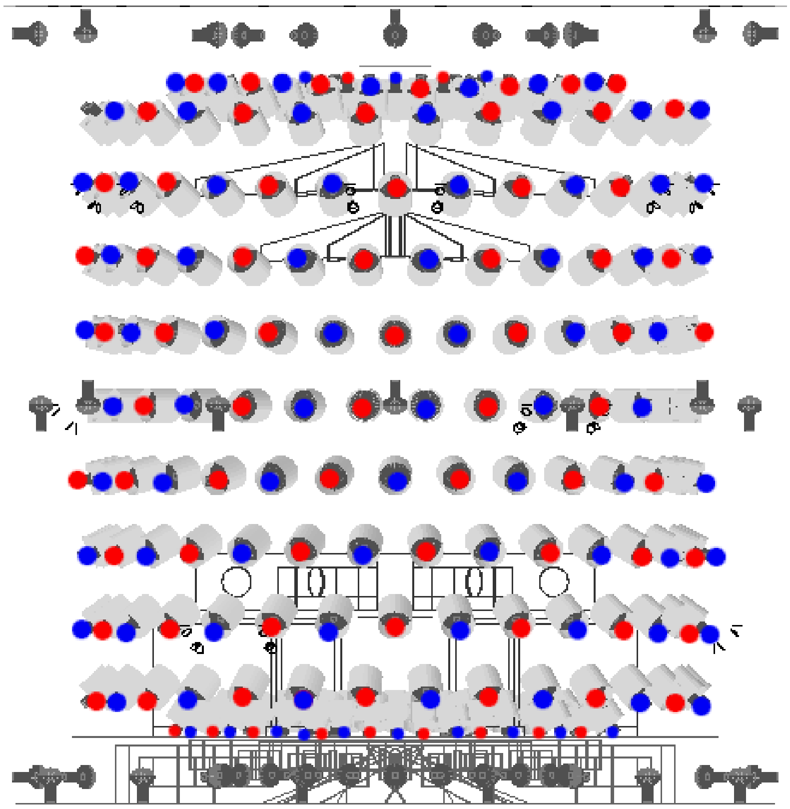

Figure 4.1: **The macro-grouping of the central region PMT.** The red and blue colors represent the sharing between trigger boards.

A general view on the photomultipliers distribution in Double Chooz is shown in figure (4.1). The inclination angles are chosen for an uniform response of the detector. In addition, the buffer region which isolates the PMT area from the gamma catcher (figure 2.4), increases the distance between the point of energy deposition and photomultipliers contributing to the detector uniformity. The orientation of the inner veto photomultipliers is shown in table (4.1).

4.2 Central Region PMT Grouping

For the central region, the macro-grouping is **"interlaced"** meaning that the selection of photomultipliers which belong to different trigger boards is alternating, as shown in figure (4.1) and in figure (4.2).

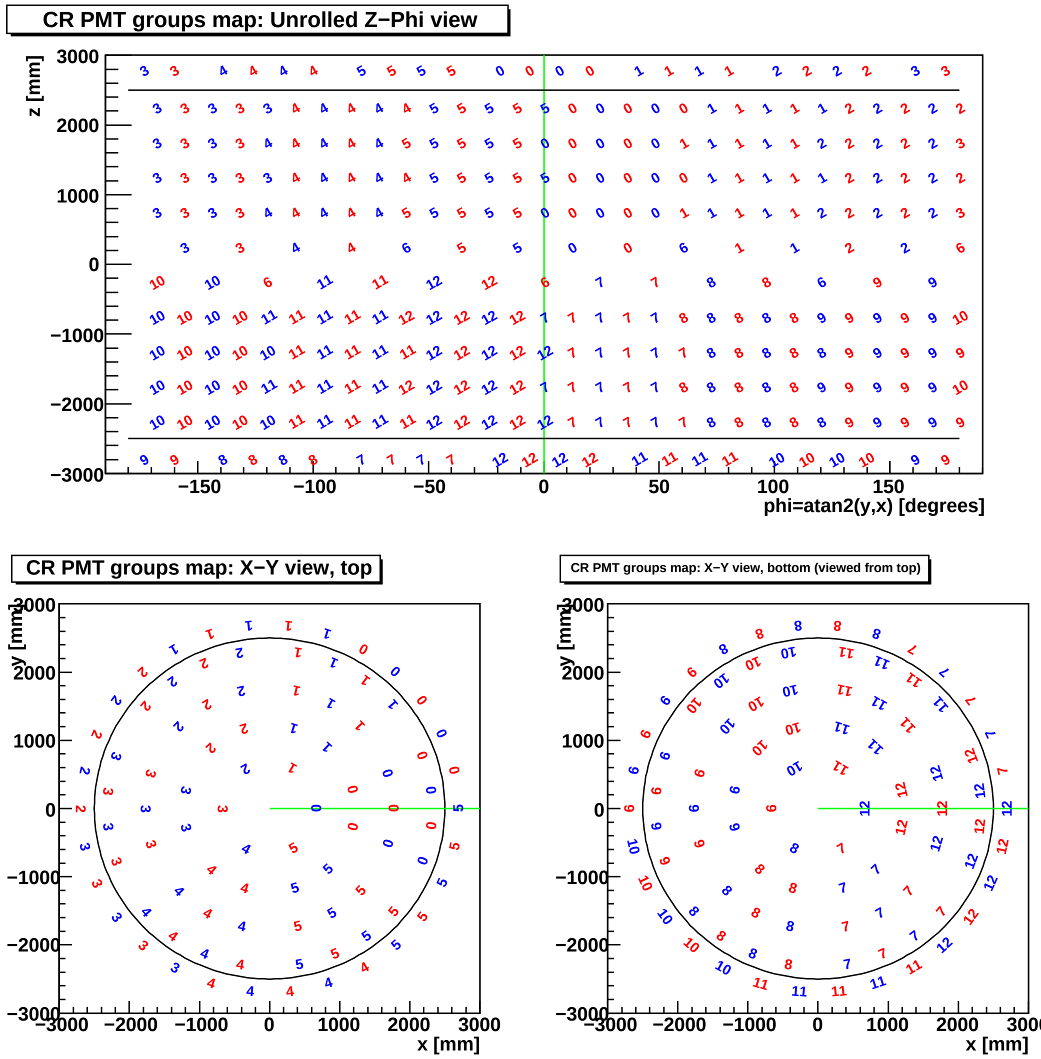

Figure 4.2: **Central region PMT groups map.** The red and blue colors correspond to the central region trigger boards. The plots represent the micro-grouping indexes of the photomultiplier groups as described in appendix (B).

Regarding the central region micro-grouping, each "interlaced" half is further divided into 12 groups, 6 of them belong to the upper side of the detector and the rest of 6 belong to the lower side of the detector. The PMT groups have 16 photomultipliers each and correspond to the trigger board inputs. There are two groups, one for each trigger board which contain only 3 photomultipliers. These groups are positioned in the middle ring.

4.3 The Grouping of the Inner Veto Photomultipliers

The inner veto grouping is used by the muon recognition algorithm, presented in chapter (5). The difference to the central region is that different PMTs do not observe the same volume.

The inner veto micro-grouping is based on **PMT group areas**. The PMT group areas are virtual structures containing one or more PMT groups. As will be shown in chapter (5), for background muons, the PMT group responses are similar inside a group area. The group areas distinguish the regions with energy depositions inside the inner veto.

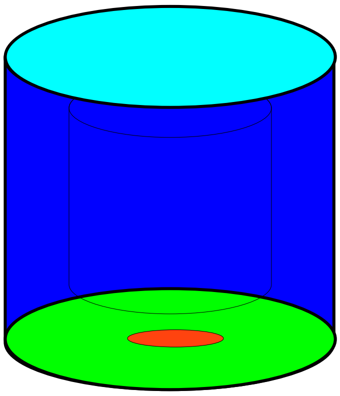

Figure 4.3: **Inner veto PMT group areas.** The inner cylinder indicates the central region. The color correspondence is the same as in text and in table (4.1).

In total, there are 18 PMT groups for inner veto, this number representing the maximum number of trigger board inputs. This "maximum granularity" is justified by the necessity of having groups of similar response for the given group area.

The general view on the distribution of the PMT group areas is shown in figure (4.3) and in table (4.1). Considering identical color notation, the group areas can be described as:

Top contains five groups, one group with 6 PMTs and four others with 3 PMT, each. This area is not used by the muon recognition algorithm presented in this thesis. Other muon recognition algorithms [60] require correlated information from the upper and the lower regions of the inner veto volume.

Lateral has six groups, each of them containing 5 PMT. As can be seen in table (4.1), the lateral area contains photomultipliers of all given orientations.

Down has six groups, each with 4 PMT.

Bottom is a special group area containing only one group with 6 PMT. The separation of the Bottom from the Down area is justified by the presence of the bottom walls of the central region support (figure 2.4).

The numbering scheme of the inner veto groups is shown in figure (4.4).

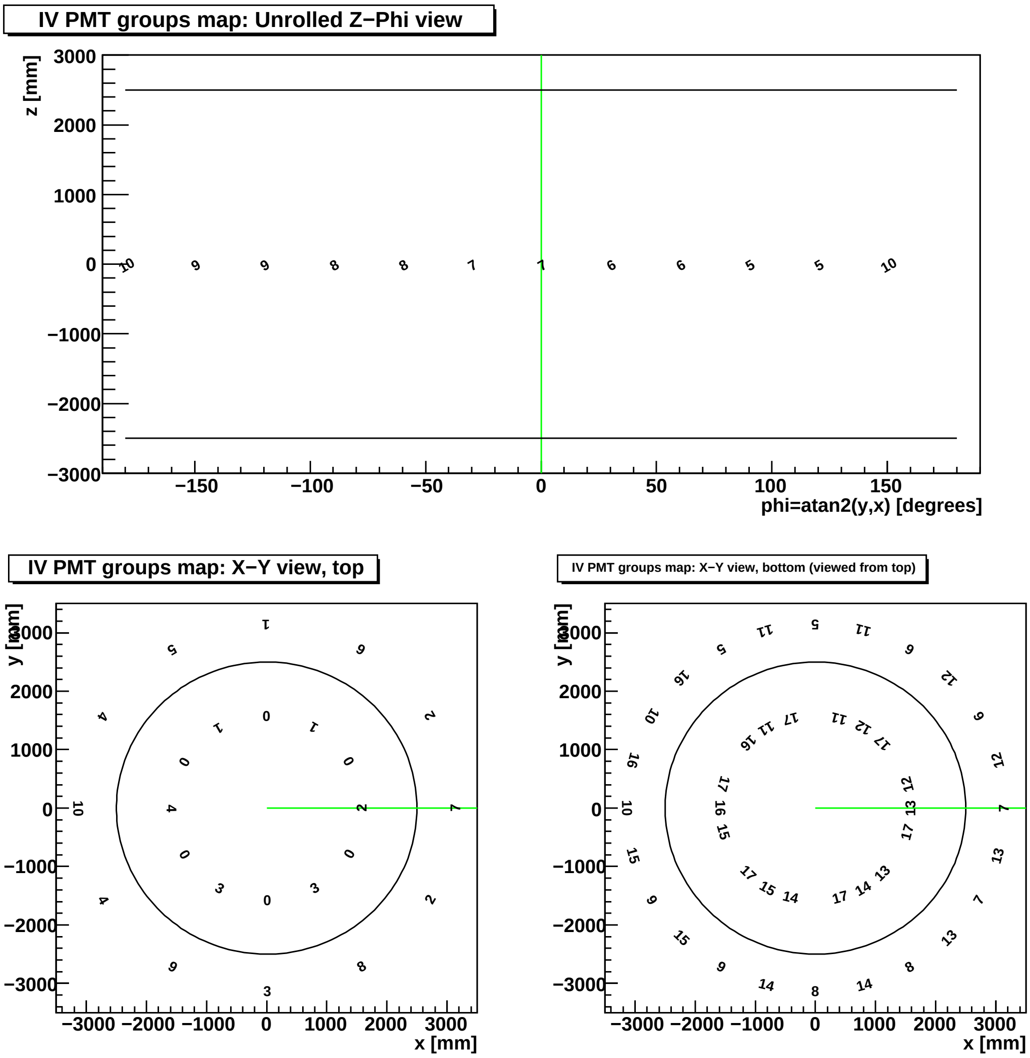

Figure 4.4: **The grouping map of the inner veto PMTs.** The numbers represent the indexes of the photomultiplier groups as described in appendix (B).

$\odot$		$\otimes$		$\odot$		$\otimes$		$\odot$		$\otimes$		$\odot$		$\otimes$		$\odot$		$\otimes$		$\odot$		$\otimes$		ring 0
$\downarrow$		$\otimes$		$\downarrow$		$\otimes$		$\downarrow$		$\otimes$		$\downarrow$		$\otimes$		$\downarrow$		$\otimes$		$\downarrow$		$\otimes$		ring 1
$\downarrow$		$\uparrow$		$\downarrow$		$\uparrow$		$\downarrow$		$\uparrow$		$\downarrow$		$\uparrow$		$\downarrow$		$\uparrow$		$\downarrow$		$\uparrow$		ring 2
$\uparrow$	$\otimes$	$\uparrow$	$\otimes$	$\uparrow$	$\otimes$	$\uparrow$	$\otimes$	$\uparrow$	$\otimes$	$\uparrow$	$\otimes$	$\uparrow$	$\otimes$	$\uparrow$	$\otimes$	$\uparrow$	$\otimes$	$\uparrow$	$\otimes$	$\uparrow$	$\otimes$	$\uparrow$	$\otimes$	ring 3
$\odot$	$\otimes$	$\odot$		$\odot$	$\otimes$	$\odot$		$\odot$	$\otimes$	$\odot$		$\odot$	$\otimes$	$\odot$		$\odot$	$\otimes$	$\odot$		$\odot$	$\otimes$	$\odot$		ring 4

Table 4.1: **The orientation of the inner veto photomultipliers** The symbols are considered from the outside view. $\otimes$ and $\odot$ are the PMT which "look" to the interior respectively to the exterior of the detector. The arrows represent the up-down orientation. The colors show the affiliation to the PMT group areas as shown in figure (4.3).

Chapter 5

Trigger Design Studies

5.1 Introduction

The simulation studies presented in this chapter aim to provide the optimization of the trigger algorithm and the determination of the trigger efficiency. The optimization of the trigger algorithm results from the analysis of various design parameters which can influence the trigger efficiency. For this purpose, the simulation packages within DOGS framework has been used. The Double Chooz simulation software has been described in chapter (2). The Geant4 based simulations are performed using DCGLG4sim, the component which is modeling the detector's response "from the interaction to the photomultiplier's photo-cathode". Further signal processing is simulated by the DCRoSS package, the read-out simulation software of the Double Chooz experiment.

Characteristic for physics events is an energy deposition by gamma in the target volume: the positron, released in an inverse beta decay, deposits its energy in scintillator and annihilates with an electron, releasing two 511 KeV gammas. On the other side, the neutron from the same reaction is captured after thermalization by gadolinium nuclei which, releases a burst of gamma rays with a total of 8 MeV. Hydrogen nuclei can also capture neutrons releasing 2.2 MeV energy. The gamma events will be used through the trigger design studies. The trigger efficiency for the other physics and background events will be presented and discussed later.

An important attention is given to events with energies in the region of the main trigger threshold, namely 0.5 MeV. All events releasing energies which fulfills the main trigger threshold condition (section 3.2) are further considered by the data acquisition system and stored. The higher threshold conditions for antineutrino and background events will also be analyzed. The low threshold (0.3 MeV) will be discussed for calibration events (section 3.2).

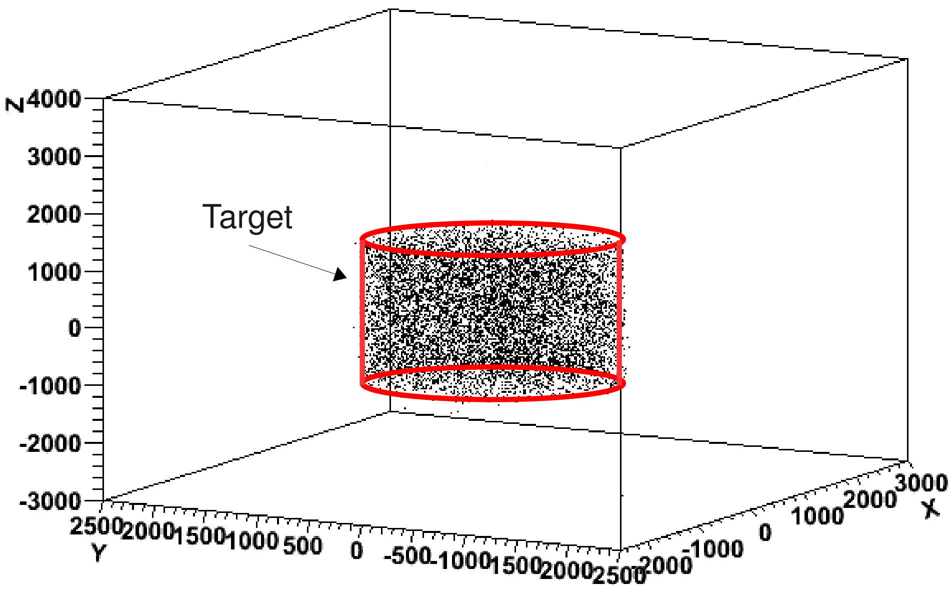

Figure 5.1: **The distribution of the fill-events.** The fill-events are generated randomly inside the detector target volume. The coordinates are given in millimeters.

For a better anticipation of the Double Chooz experimental conditions, two kinds of simulated events in the central region have been analyzed:

Central-events are generated in the center of the detector.

Fill-events are generated homogeneously, with a random positions inside the target volume (figure 5.1). This distribution of the event coordinates is a good approximation for the real events.

The differences in the detector response between the central- and the fill-events are shown in figure (5.2) for detected photoelectrons versus visible energy, using 1 MeV gamma. The visible energy is proportional to the light released by scintillator, and is smaller than the total energy deposed. This difference is given by the quenching effect expressed by the Birk's semi-empirical law [55]:

$$L(E) \propto \int_0^E \frac{1}{1 + k_B \frac{dE}{dx}} dE \tag{5.1}$$

where dE/dx denotes the specific energy loss and k_B, the Birk's constant. L, is the total amount of light emitted by the scintillator and is proportional to the number of the photon obtained from an energy deposition. The number of the obtained photoelectrons depends on other parameters such as the position of the energy deposit in the detector, the attenuation length, the orientation of photomultipliers, etc. [46].

At this point a distinction is made between the energy measured in detector and the "generated" energy, used in the following trigger simulations. The "generated" energy is the input energy of the simulated event.

It is a general approach to associate the trigger thresholds with a physical quantity directly related to the detector performance. In the case of Double Chooz, it is convenient to express the threshold voltage in terms of photoelectrons emitted by the photo-cathode of photomultipliers.

The plot (5.2) shows few small energy depositions for the fill-events. These are the events in the detector chimney or escaping gammas with interaction vertexes close to the target boundary. A subset of these events does not fulfill the triggering conditions and in consequence will lower the trigger efficiency as it will be shown later.

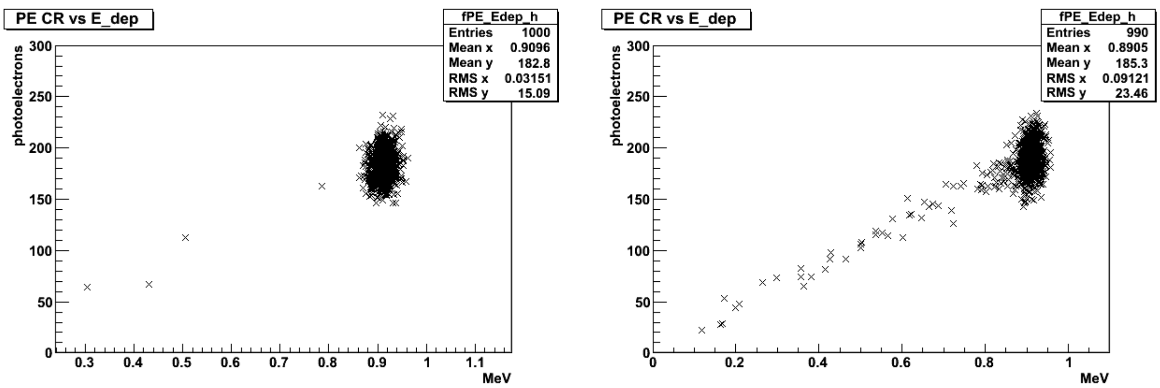

Figure 5.2: **The number of detected photoelectrons function of the visible energy for the central- (left) and fill- (right) events.** See the text for the description of the events particularities.

Figure (5.3) presents the number of photoelectrons detected by each PMT in the central region, for 1 MeV fill-events. This distribution reflects the cylindrical geometry of the detector. The photomultipliers which are situated closer to the detector center collect, in average, more light. These are the PMT from the median, the center-top and the center-bottom regions. Analogously, the photomultipliers receiving less light are those from corners. For the goal of an identical response of both trigger boards, the distribution of photomultipliers between boards will depend on their positions as shown in chapter (4).

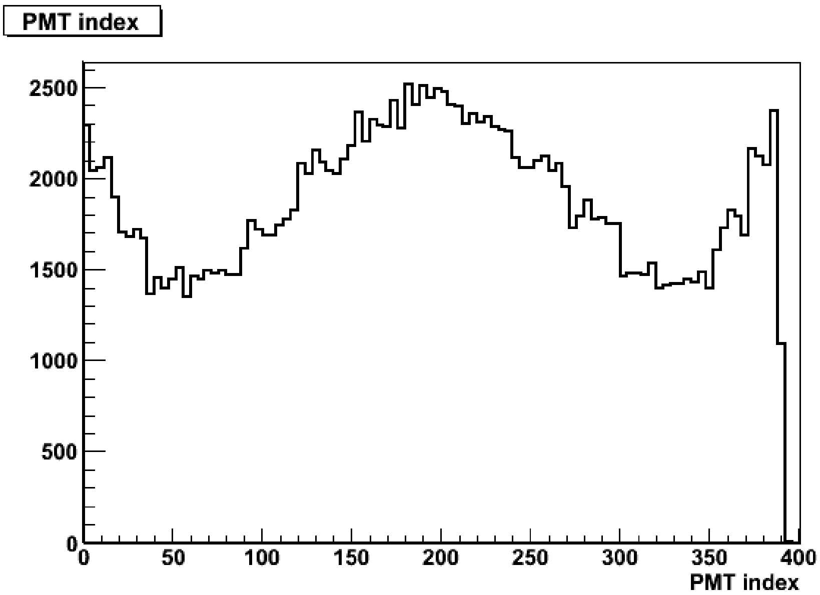

Figure 5.3: **The photoelectrons distribution for the central region photomultipliers.** The events are 1 MeV gamma, filling the target region.

The distribution of arrival times for photoelectrons released in fill-events, is plotted in figure (5.4). The arrival times are influenced by the decay time of scintillator and by the detector geometry. For Double Chooz, decay time of scintillator is of the order of 200 ns depending on the type of particle which produces the interaction (equation 5.1). It is assumed 256 ns as the event window [56], meaning the typical duration of a physics event. The event window is defined by waveform digitizers based on timing information provided by the trigger system.

In order to study how the trigger efficiency is influenced by electronics components, a trigger model included included in the Double Chooz read-out simulation software (DCRoSS) will be used. The implementation details will be discussed in section (5.2.5).

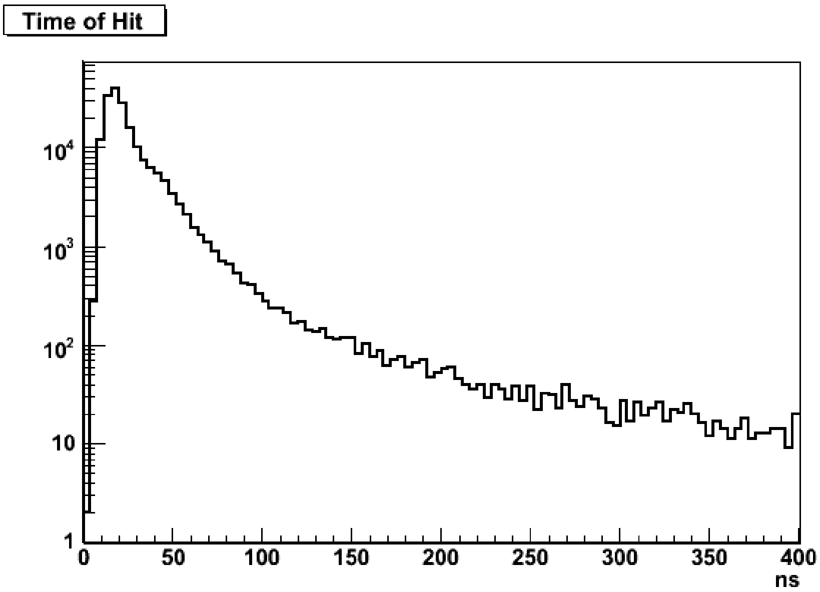

Figure 5.4: **The arrival times of photoelectrons for 1 MeV gamma fill-events.** The main influence is given by the decay time of the scintillator for the given detector geometry.

5.2 The Trigger Efficiency

The trigger efficiency is defined as the ratio between the events selected by the trigger and the total number of events that the trigger is intended to select:

$$\varepsilon = \frac{N_{fired}}{N_{all}} \tag{5.2}$$

If the efficiency depends on several independent triggering conditions, then the total trigger efficiency is the product of the independent efficiencies.

In fact, here one considers only those events which release a visible energy deposition, so that equation (5.2) becomes:

$$\varepsilon = \frac{N_{triggered}}{N_{all} - N_{null}} \equiv \frac{N_{triggered}}{N_{all>0}} \tag{5.3}$$

The error in the determination of the trigger efficiency is binomial and can be written as:

$$\delta\varepsilon = \sqrt{\frac{N_{triggered} \cdot N_{non-triggered}}{N^3_{all>0}}} = \sqrt{\frac{\varepsilon(1-\varepsilon)}{N_{all>0}}} \tag{5.4}$$

Considering relation (5.4), a small uncertainty can be achieved for a trigger efficiency close to one. In addition, an efficiency close to the unity will minimize the time necessary for the wanted statistics of the Double Chooz experiment.

In order to compute the analytical expression of the trigger efficiency for central region events, one assumes an identical behaviour of the related trigger boards. In addition, the multiplicity condition is set to a low level so that its effect on the trigger efficiency can be neglected. With these conditions fulfilled, for each of the central region trigger boards the efficiency can be regarded as a convolution between the Gaussian function and the Heaviside (step) function:

$$\varepsilon^{A}(E) = \varepsilon^{B}(E) \equiv \varepsilon^{A,B}(E) = \mathrm{G} \otimes \mathrm{H} = \frac{\varepsilon_{\infty}^{A,B}}{2}\left(1 + \mathrm{erf}\left(\frac{E - E_{th}^{A,B}}{\sqrt{2}\sigma^{A,B}}\right)\right) \tag{5.5}$$

$E_{th}^{A,B}$ is the threshold energy, given by the step function and $\sigma^{A,B}$ is the standard deviation of the Gaussian function. E is the specific energy of the related event and $\varepsilon_{\infty}^{A,B}$ is the amplitude of the efficiency function. E is proportional but lower than the measured energy in the detector as mentioned in section (5.1). erf is the error function, described in appendix (C).

The efficiency of a central region trigger board can be obtained from a sample of simulated events. Expression (5.5) is used in this case to fit the simulated data as shown in figure (5.5) and table (5.1) line 3.

The same formalism can be applied when all the inner detector photomultipliers are grouped together in one "virtual" trigger board (figure 5.6). This is foreseen for Double Chooz, but it is discussed here in order to evaluate the differences in the trigger efficiency which are introduced by a design based on two independent central region boards. However, as it is described in chapter (3) and in section (5.3), the actual trigger concept provides a series of advantages related to redundancy and the possibility to monitor the trigger efficiency from offline data. The efficiency parameters for "all the photomultipliers together" case are those from table (5.1) and figure (5.6). One can notice that, in this situation, the trigger efficiency is equivalent to the detection efficiency for the given threshold. As in the case represented in figure (5.5), the amplitude smaller than unity is justified by the events which do not have interactions in the central region. The fraction σ/μ is smaller, due to the increased number of photomultipliers with respect to the single trigger board case.

Considering the logic "OR" function between the individual responses of the central region boards, the entire trigger system efficiency can be expressed in terms

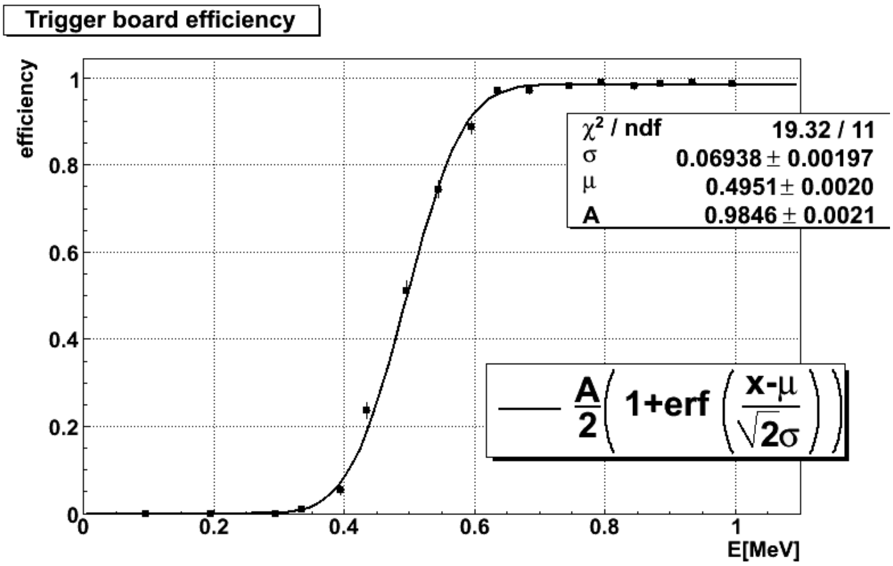

Figure 5.5: **The central region trigger board efficiency.** The board threshold is set to 0.5 MeV, the multiplicity is ≥2 PMT groups (M_2) and the grouping of the photomultipliers is interlaced. The interlaced grouping was described in chapter (4) Note: This plot do not represent the trigger system efficiency, because the logic OR between the trigger boards decisions will be considered. The amplitude (A parameter) is smaller than 1 due to few events that do not have interaction in the central detector. $\sigma/\mu \simeq 14\%$.

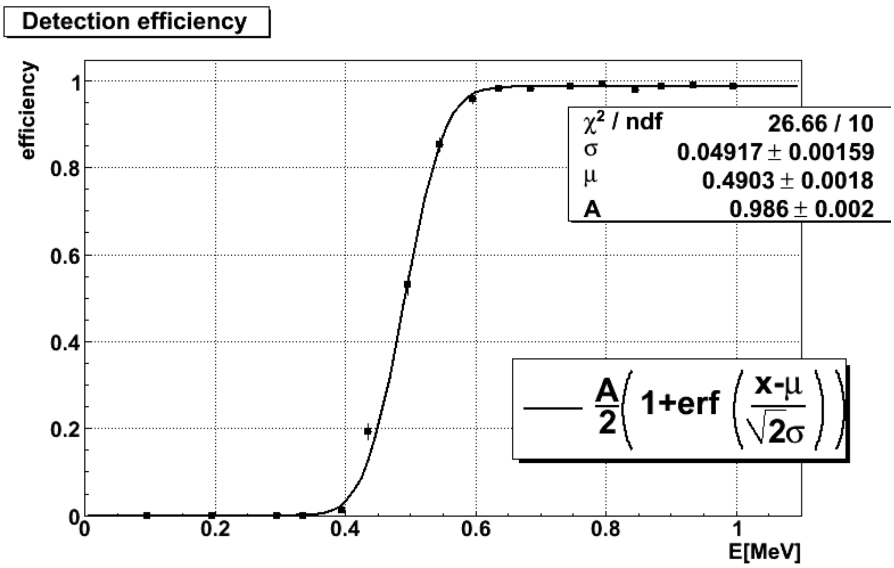

Figure 5.6: **The efficiency for "all photomultipliers grouped together" case.** The events considered are gammas filling the target region. The trigger board threshold is 0.5 MeV and the multiplicity condition is M_2.

of individual boards efficiencies, assumed equal:

$$\begin{aligned} \varepsilon(E) = & \quad \varepsilon^A(E) \vee \varepsilon^B(E) & (5.6) \\ = & \quad \varepsilon^A(E) + \varepsilon^B(E) - \varepsilon^A(E) \cdot \varepsilon^B(E) & (5.7) \\ = & \quad 2\varepsilon^{A,B}(E) - \left(\varepsilon^{A,B}(E)\right)^2 & (5.8) \end{aligned}$$

where $\varepsilon^{A,B}(E) = \varepsilon^A(E) = \varepsilon^B(E)$ is the efficiency of one central region trigger board. Inserting (5.5) into (5.8), one obtains:

$$\varepsilon \cong \frac{\varepsilon_\infty}{4}\left(-erf^2\left(\frac{E-E_{th}^{A,B}}{\sqrt{2}\sigma^{A,B}}\right) + 2erf\left(\frac{E-E_{th}^{A,B}}{\sqrt{2}\sigma^{A,B}}\right) + 3\right) \quad (5.9)$$

$$= \frac{\varepsilon_\infty}{4}\left(1 + erf\left(\frac{E-E_{th}^{A,B}}{\sqrt{2}\sigma^{A,B}}\right)\right)\left(3 - erf\left(\frac{E-E_{th}^{A,B}}{\sqrt{2}\sigma^{A,B}}\right)\right) \quad (5.10)$$

For expression (5.10) it is assumed that $\varepsilon_\infty = \varepsilon_\infty^{A,B} \cong (\varepsilon_\infty^{A,B})^2$.

At this point one can compute the so called "the effective parameters" of the trigger system efficiency, representing the threshold value, the standard deviation and the amplitude for expression (5.10):

For relation (5.10), one obtains numerically:

$$\sigma = \frac{E_{\varepsilon=84.1\%\varepsilon_\infty} - E_{\varepsilon=15.9\%\varepsilon_\infty}}{2} \cong 0.82\,\sigma^{A,B} \quad (5.11)$$

and further:

$$E_{th} = E_{\varepsilon=50\%\varepsilon_\infty} \cong E_{th}^{A,B} - 0.545\,\sigma^{A,B} \quad (5.12)$$

As in the trigger board case, the trigger efficiency parameters are obtained using simulated data samples. The events considered are gamma having energies below 1 MeV. The central-events case is shown in figure (5.7) and the fill-events case in figure (5.8).

As described in section (5.1), some of the fill events which do not have interaction in the central detector may have small energy depositions even if the generated energy was much higher. This results in the deviation of the efficiency amplitude

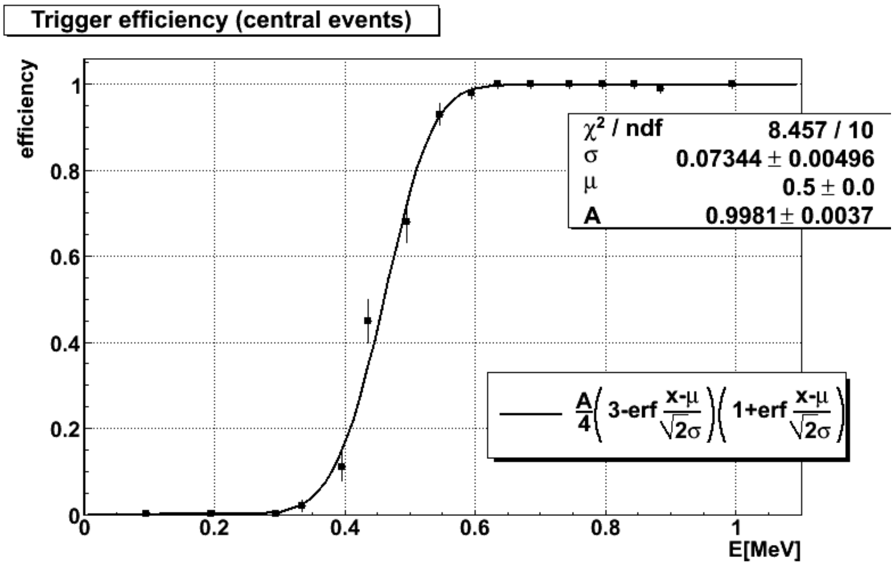

Figure 5.7: **The trigger system efficiency for gamma central-events.** The trigger board threshold is 0.5 MeV and the multiplicity condition is M_2 ($\geq$2 PMT groups).

parameter A$\leq$1. So, this is not a loss of the trigger system but rather a consequence of the Double Chooz detectors design.

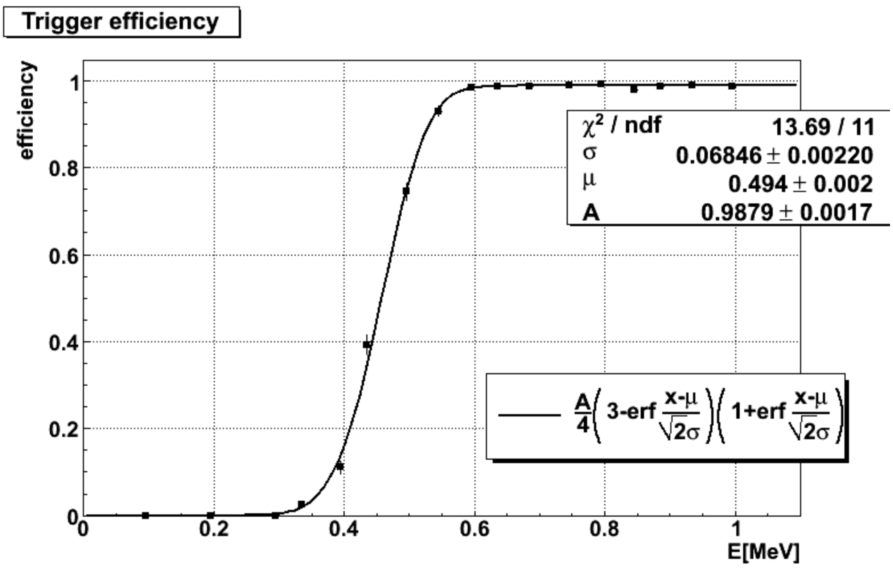

Figure 5.8: **The trigger system efficiency for gamma fill-events.** The trigger board threshold is 0.5 MeV and the multiplicity condition is M_2.

The cases considered before, are summarized in table (5.1). For one trigger board case and the "all PMT together" case, the fitting parameters are the same as the effective parameters. This table also shows the variance-to-mean ratio (VMR) for each considered case. The variance-to-mean ratio is a measure of the dispersion of the efficiency function at threshold:

$$VMR \equiv \frac{\sigma}{\mu} \tag{5.13}$$

σ is equal with $\sigma^{A,B}$ for the single trigger board case. Using equation (5.11), σ becomes $0.82\,\sigma^{A,B}$ for the entire trigger system. μ is equal with $E_{th}^{A,B}$ for the single trigger board case. Using relation (5.12), μ becomes $E_{th}^{A,B} - 0.545\,\sigma^{A,B}$ for the entire trigger system.

Case	σ [KeV]	E_{th} [KeV]	Ampl.	VMR
2 boards, fill-events (reference)	55.76	456.44	98.6	0.12
All PMT together	49.9	490.2	98.3	0.1
One trigger board	69.9	495.4	98.2	0.14
2 boards, central-events	60.19	460	99.8	0.13

Table 5.1: **The trigger efficiency parameters for the general cases considered.** σ, E_{th} and amplitude are obtained by fitting the efficiency functions. For two trigger boards cases, relations (5.11) and (5.12) has been used. An extended comparison including also other design cases is presented in appendix D.

In general, the efficiency parameters for two boards fill-events (reference) case show better values with respect to the other considered cases. The efficiency parameters reflect the effect introduced by the trigger design based on logical OR between the decisions of two central region boards.

The exceptions are given by σ for the "all PMT together" case and by amplitude for the central-events case. The threshold value for central-events is justified by a larger absorption of the emitted photoelectrons with respect to the reference case. This is due to bigger distances between the interaction points and photomultipliers with respect to the reference case.

The amplitude parameter for central-events is bigger than for fill-events, due to a smaller number of events which have low energy depositions (figure 5.2). The amplitude smaller than the unity in this case is due to the events in the detector "chimney".

One can also see that even if only one trigger board is used, accordingly one half of all photomultipliers, the efficiency at energies inside the physics event range is high. In the eventuality of a hardware failure related to one trigger board, the other board has high efficiency for physics events.

5.2.1 Influences of the Central Region PMT Grouping

The actual photomultipliers grouping scheme for Double Chooz is described in chapter (4) and in appendix (B). One retains here the steps which concluded to the present PMT grouping configuration.

Two PMT grouping cases for the central region (figure 5.9) have been considered, in order to study the effect on the trigger efficiency:

Interlaced is the case where every two adjacent photomultipliers belong to different trigger boards.

Up-Down considers the upper region PMTs as belonging to one trigger board, and the lower region PMTs as belonging to the other trigger board.

In both cases, the number of photomultipliers per board is the same and is equal to half of the total number of photomultipliers.

The trigger efficiency for the interlaced grouping is shown in figure (5.8) and for the up-down grouping in figure (5.10). For both cases, the efficiencies parameters are given in table (5.2).

Case	σ	E_{th}	Ampl.	VMR
Interlaced (reference)	55.76	456.44	98.6	0.12
Up-down	64.37	403.12	98.9	0.16

Table 5.2: **The trigger efficiency parameters for interlaced and up-down PMT grouping.** For both cases, gamma fill-events are considered.

There is a decrease of the effective threshold value for up-down with respect to the interlaced case. This is a consequence of small attenuation distances for events placed at the top or at the bottom of the detector, where either the up or the down coverage is good. The σ parameter is bigger for up-down than for interlaced due to a larger dispersion of the trigger boards responses. As is shown in figure (5.11), the spread of the photoelectrons response for fill-events is much larger for the up-down case.

Due to these large differences in the trigger boards responses for fill-events, one cannot consider the equivalency of the central region trigger boards for up-down grouping. The trigger system efficiency cannot be approximated in this case using

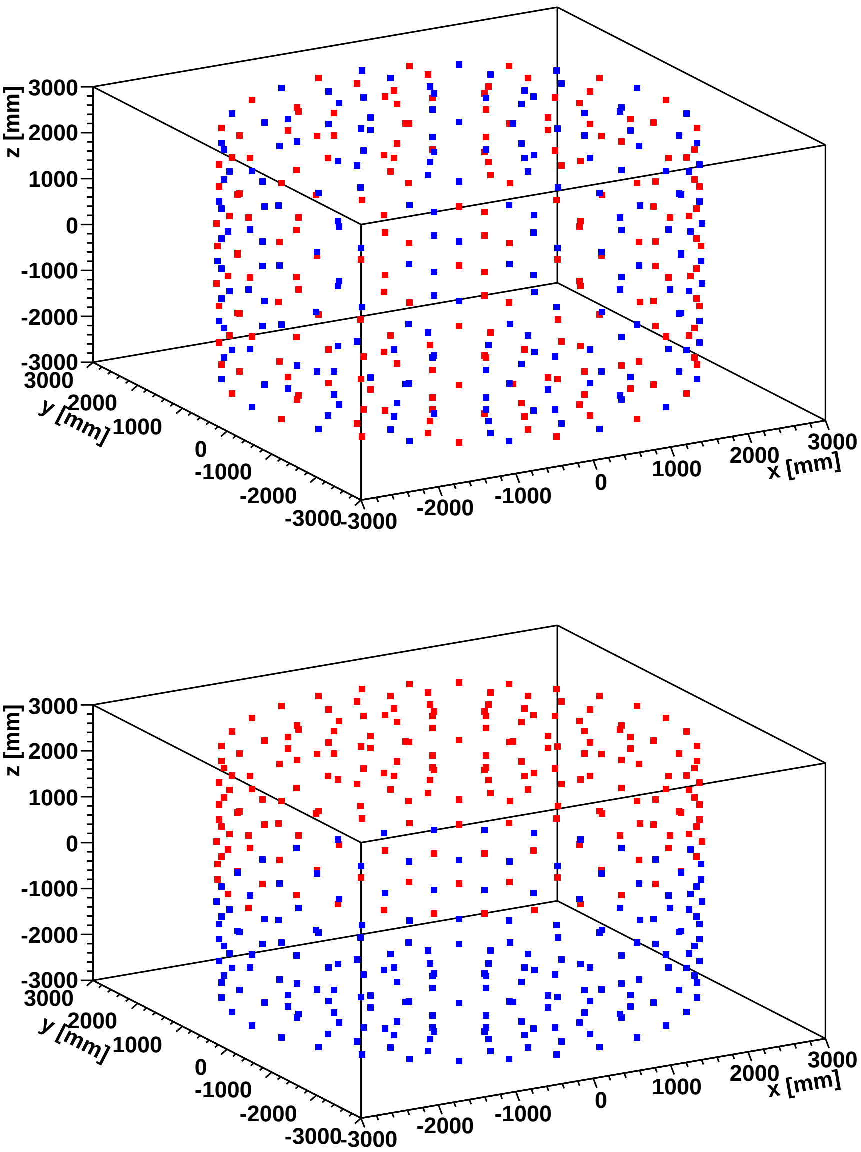

Figure 5.9: **Two configurations of the PMT grouping: interlaced (upper side) and up-down (down side).** The colors correspond to the trigger boards and the coordinates to the central region PMT.

relation (5.10) because $\varepsilon^A \neq \varepsilon^B$. Moreover, if a hardware failure occures in one trigger board, the efficiency of the remaining board is low for events situated in the other half of the detector.

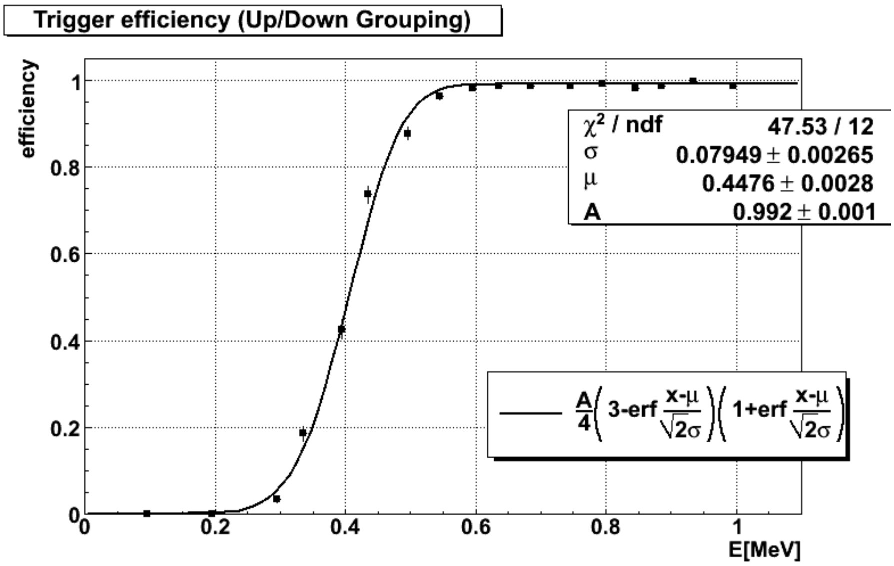

Figure 5.10: **The trigger efficiency for gamma fill-events, considering up-down PMT grouping.** The trigger board threshold is 0.5 MeV and the multiplicity condition is M_2.

5.2.2 The Multiplicity Effect

The multiplicity of the PMT groups is introduced in the Double Chooz trigger as a measure against noisy photomultipliers. By asking for, at least, two PMT groups to be above the group threshold, the probability that an unusual PMT behavior to trigger the detector is decreased. The multiplicity is used by the algorithm of each trigger board as a necessary condition.

Figure (5.8) considers multiplicity M_2 (i.e. at least two groups above the group threshold E_{gr}) and $E_{gr} = 0.25$ photoelectrons/PMT. The influence of multiplicity in this case is shown in figure (5.12). Here, the effect is demonstrated by the events which do not fulfill the multiplicity condition, but fulfill the total energy condition. The events letting low energy depositions do not fulfill the energy sum condition (less than 0.3 MeV in figure 5.12). The events letting high energy depositions, trigger the multiplicity condition (greater than 0.9 MeV in figure 5.12). For the energy region of the physics events, the multiplicity condition is always fulfilled.

The influence of the multiplicity on the trigger efficiency can be also understood from the following two cases. In the first case, the multiplicity is set at M_4 and $E_{gr} = 0.25$ photoelectrons/PMT and is represented in figure (5.13). The second case, the group threshold is set at $E_{gr} = 0.5$ photoelectrons/PMT (figure 5.14). The trigger efficiency parameters for these cases are given in table (5.3).

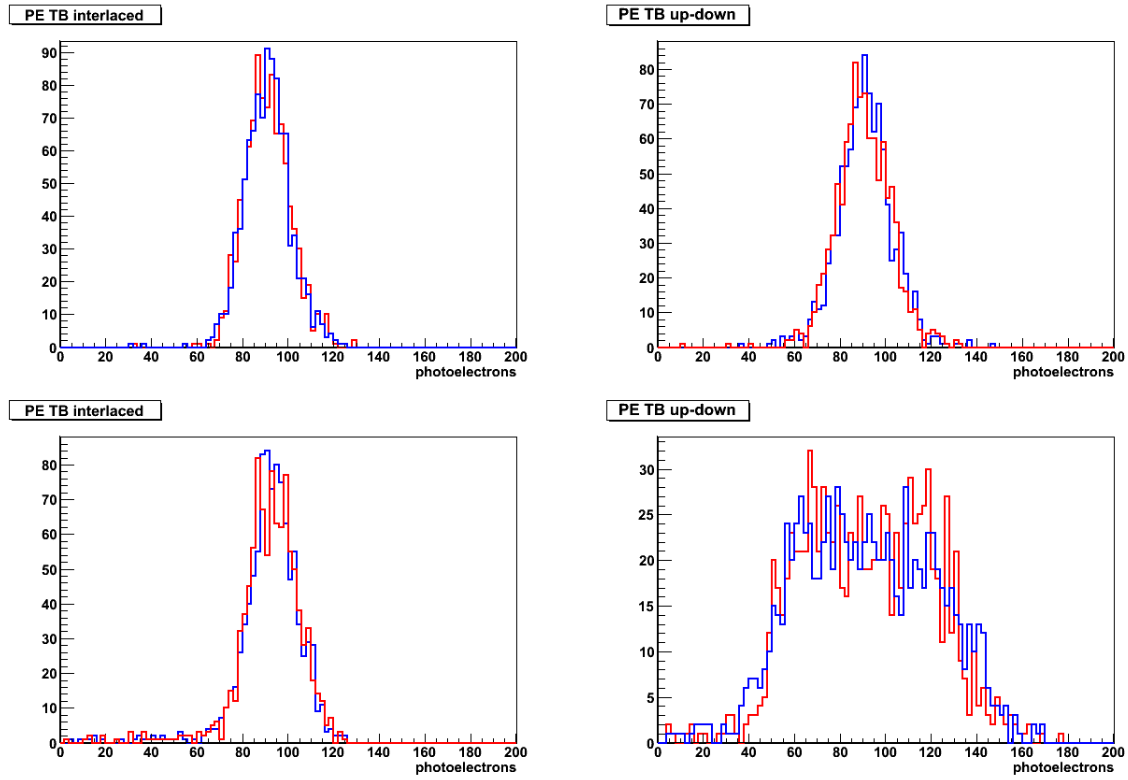

Figure 5.11: **The photoelectron distributions "seen" by trigger boards for different PMT grouping configurations: interlaced and central-events (up-left), interlaced and fill-events (down-left), up-down and central-events (up-right), up-down and fill-events (up-right).** The colors represent the trigger boards. The events considered are 1 MeV gamma, fill-events.

Case	σ	E_{th}	Ampl.	VMR
M_2, $E_{gr} = 0.25\,\mathrm{pe/PMT}$ (reference)	55.76	456.44	98.6	0.12
M_4, $E_{gr} = 0.25\,\mathrm{pe/PMT}$	58.71	464.28	98.3	0.13
M_2, $E_{gr} = 0.5\,\mathrm{pe/PMT}$	109.22	636.21	95.1	0.17

Table 5.3: **The influence of the multiplicity and of the group threshold on the trigger efficiency.** The values are obtained fitting the corresponding efficiency functions.

From the results presented in table (5.3), one can notice a significant influence on the trigger efficiency when the group threshold is increased to 0.5 pe/PMT. In conclusion, the group threshold value has to be carefully controlled and calibrated, having an important impact on the trigger efficiency. Increasing the multiplicity condition to M_4, it results also in worst values of the efficiency parameters.

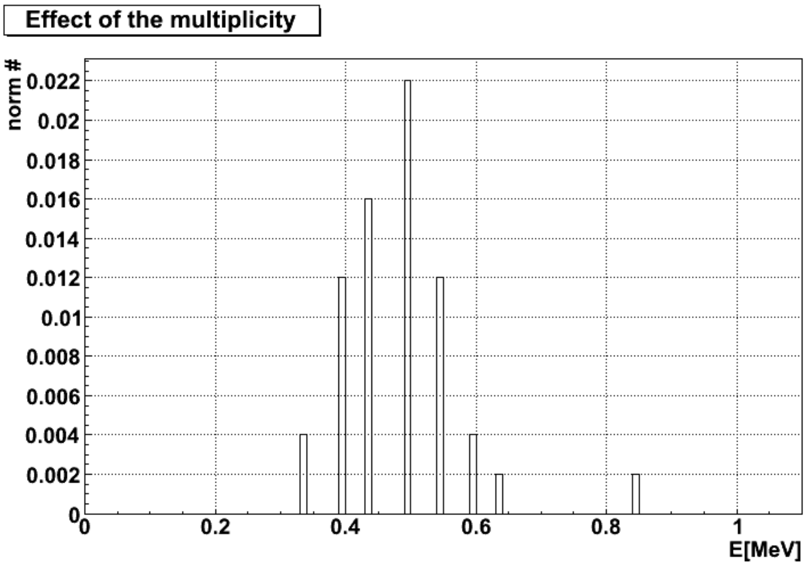

Figure 5.12: **The multiplicity effect on the trigger efficiency.** The plot represents the events which not fulfill the M_2 condition, but fulfill the sum threshold condition. The events are normalized to unity. The trigger set-up and the type of events are the same as in figure (5.8).

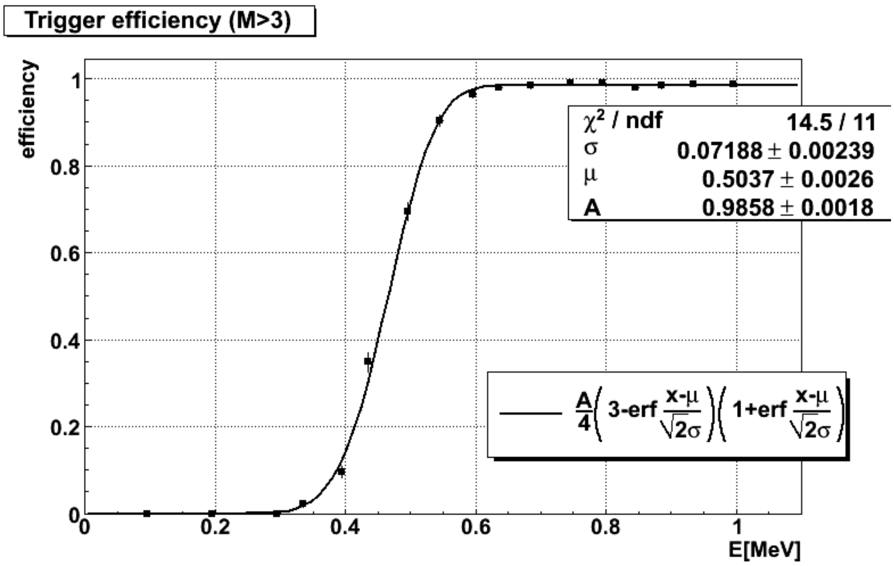

Figure 5.13: **The trigger system efficiency for multiplicity M_4 (i.e. more than 3 PMT groups).** The other trigger parameters are set to the same values as in figure (5.8).

The reference case considers low value for the group threshold and the minimum multiplicity such that the effect on the trigger efficiency to be minimal.

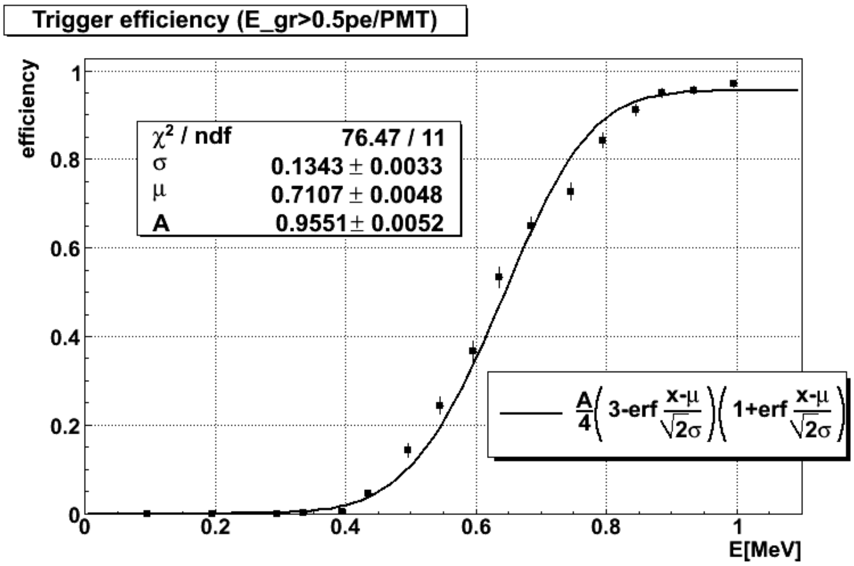

Figure 5.14: **The trigger system efficiency for the group threshold (E_{gr}) set to 0.5 photoelectrons/PMT.** The other trigger parameters are set to same values as in figure (5.8).

5.2.3 The Event Position and the Trigger Efficiency

The trigger efficiency is different in different detector regions. This fact increases the difficulty of the trigger thresholds calibration. As shown in figure (5.15), the efficiency is constant for events in the target region. In the gamma catcher, the smaller values of the efficiency are caused by escaping gammas.

One may also consider an effect related to the energy depositions inside the vessel walls. This deviation of the trigger efficiency is better seen in figure (5.15-left) for the boundary between target and gamma catcher, at $\simeq$1.1 m from the detector center. Here, the considered events are related to ^{137}Cs sources and used for the calibration of the 0.5 MeV trigger threshold, as discussed in section (5.3.5). The study of spatial variations of the trigger efficiency is an important step in the calibration for Double Chooz.

5.2.4 The PMT Failure Case

During the operation of the experiment, some of the photomultipliers tubes could become defective. The identification of the dead PMT channels is not a difficult task, but the replacement is impossible. The causes of the PMT malfunctioning are numerous [58]. In such cases, one has to reconsider the detector response for

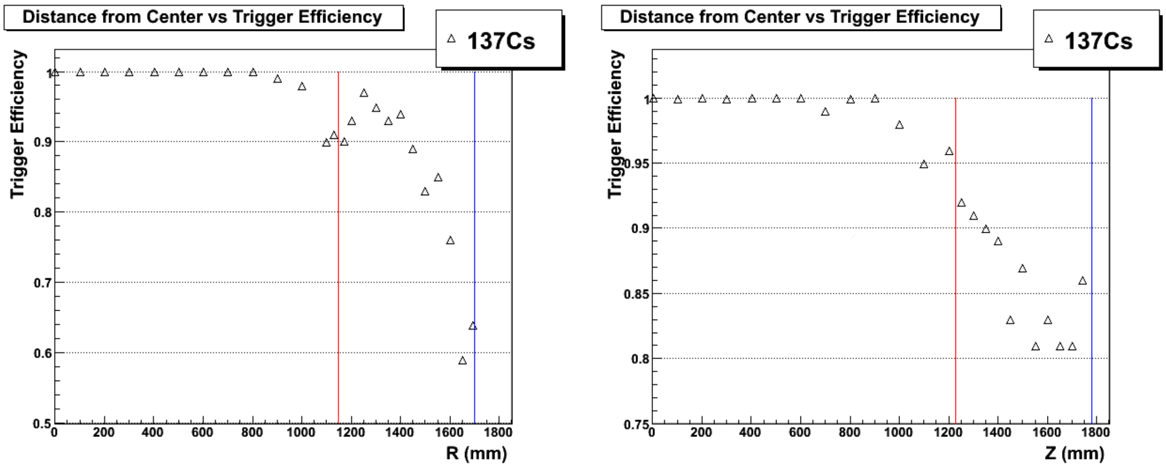

Figure 5.15: **The trigger efficiency versus distance from the detector center for events in the horizontal median plane (left) and the vertical axis of the detector (right).** The efficiency values are normalized to the trigger efficiency for the central events. The vertical color lines represent the target and the gamma catcher boundaries.

less PMT.

In figure (5.16) and in table (5.4) simulations results are presented for the scenario when 20 photomultipliers (∼5 % from the total for one detector) are not considered by the central region trigger boards.

Case	σ	E_{th}	Ampl.	VMR
all PMT available (reference)	55.76	456.44	98.6	0.12
20 PMT out of order	57.48	480.9	98.6	0.12

Table 5.4: **The influence of the dead PMTs on the trigger efficiency parameters.** The values are obtained from the fit of the corresponding efficiency function.

The decrease of the trigger efficiency performances as consequence of the PMT failures depends on the number and the position of the unconsidered channels.

5.2.5 Corrections from Electronics Simulation

As it was previously described, the trigger efficiency represents the probability of detecting a given event by the trigger system. The trigger efficiency depends on the variables that describe the event but may also depend on the effects related to the processing of the PMT signals.

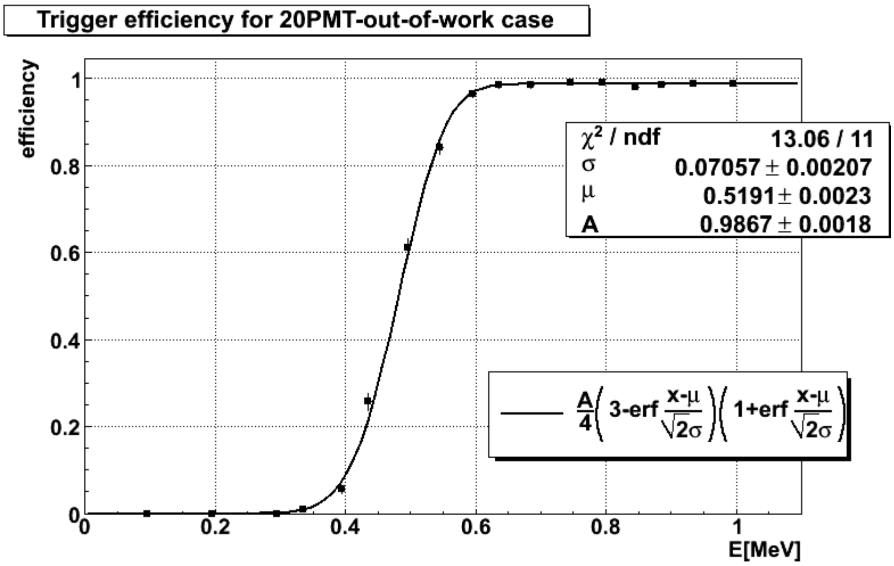

Figure 5.16: **The trigger system efficiency for gamma fill-events when 5% of the central region PMT are not taken into account.** The trigger parameters are set to same values as in figure (5.8).

Within the Double Chooz simulation software, the DCRoSS package (see chapter 2) is able to simulate the detector read-out response and the related effects. DCRoSS aims to process the Monte Carlo events in the same way as the real events are processed by the hardware read-out. The simulations will be compared with the real events during the data taking phase of the experiment. Beside other components, DCRoSS contains a trigger model which describes the hardware of the trigger system.

Following the same procedure as in the previous analysis, the effects related to the electronics read-out are determined from the trigger efficiency parameters. In this case, all the software models of the read-out components within DCRoSS are taken into consideration. The parameters of the electronics components including the trigger system are set to the foreseen values.

The results are shown in figure (5.17) and table (5.5). The comparison with the case when any influence of the electronics components is considered, can also be seen in table (5.5).

The front-end electronics might induce a deviation from the linearity of the PMT signals, and in consequence, might change the parameters of the trigger efficiency. As was shown in chapter (3), the front-end stretcher builds the trigger input signals from the photoelectron pulses from PMT. The stretcher provides

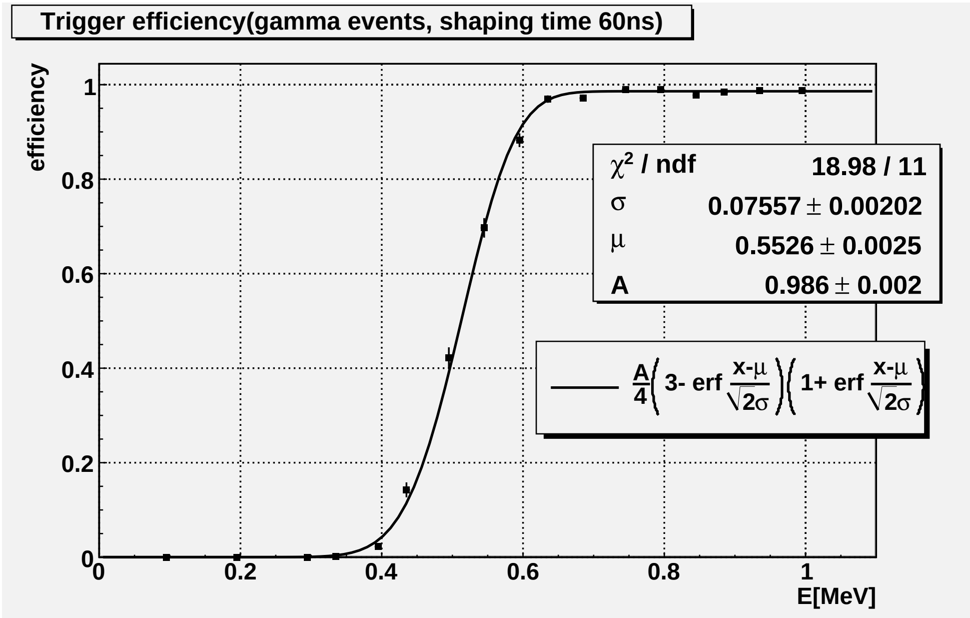

Figure 5.17: **The trigger efficiency when effects from read-out electronics are considered.** The values of the electronics components are measured by different groups within the Double Chooz collaboration and are included into the simulation software.

Case	σ	E_{th}	Ampl.	VMR
No electronics included	55.76	456.44	98.6	0.12
Electronics included	61.97	511.41	98.6	0.12

Table 5.5: **The influence of the electronics chain components on the trigger efficiency parameters.** The values are obtained from the fit with the corresponding efficiency function.

signals having amplitude proportional to their charge. The timing of the stretcher signals proportional to the stretcher time and with the photoelectrons time of arrival at photomultipliers. Therefore, the number of photoelectrons considered by stretcher is lower if the stretcher time decreases. On the other side, increasing the stretcher time, one increases the probability that a background event to be overlapped with the physics events. The stretcher time has to be proportional to the target dimensions. The reference case from table (5.5) considers as trigger inputs, the total number of photoelectrons for the related PMT channels. One can conclude that the worst trigger efficiency parameters introduced by electronic simulation (table 5.5) are due to the late photoelectrons which are not considered by the front-end stretcher.

5.3 Measuring the Trigger Efficiency

For Double Chooz, multiple possibilities to measure the trigger efficiency are foreseen. The results provided by various methods can be cross-checked and the differences, better understood.

In order to compute the minimum number of triggered events needed for measuring the trigger efficiency, one assumes that the maximum uncertainty on the absolute energy scale for physics events is 1 % [42]. The uncertainty of the threshold position (err) is considered to be 0.2 % and the VMR parameter of the trigger efficiency function is 12 % (5.1). The minimum number of triggered events is:

$$n = \left(\frac{2.58 \cdot \mathrm{VMR}}{\mathrm{err}}\right)^2 \tag{5.14}$$

For the values previously mentioned, n is of the order of 10^4 events.

5.3.1 Measuring the Trigger Efficiency With Calibration Sources

The trigger efficiency can be determined from calibration events. For this purpose, radioactive calibration sources such as ^{137}Cs and ^{203}Hg (figures 5.22 and 5.23) provide events having the same energy range as the trigger thresholds. In addition, the using of the tagged radioactive sources provide known number of events and energy. The laser pulses will be used in Double Chooz for measuring the trigger efficiency for events which exceed the energy range of the radioactive sources. The radioactive sources play a major role in the calibration of the trigger thresholds, as discussed in section (5.3.5).

5.3.2 Measuring the Trigger Efficiency Using the Low Energy Threshold

In addition to the trigger thresholds for physics and background events, a the low energy threshold, at 0.3 MeV, is applied by the central region trigger boards. The low energy threshold allows the expression of the trigger efficiency as the ratio of the events triggering the normal trigger threshold (0.5 MeV) to those triggering the low energy threshold:

$$\varepsilon(E) \equiv \frac{N_{fired\ at\ 0.5\,MeV}}{N_{all}} \simeq \frac{N_{fired\ at\ 0.5\,MeV}}{N_{fired\ at\ 0.3\,MeV}} \tag{5.15}$$

If the radioactivity rate "in situ" has large values, the low energy threshold will be prescaled. In this situation, the efficiency expression (5.15) has to consider this scaling factor.

Using the trigger efficiency expression from relation (5.15), one obtains the plot (5.18). The trigger configuration and the type of events are the same as in the case depicted in figure (5.8), therefore the method of measuring the trigger efficiency can be compared with this case (table 5.6).

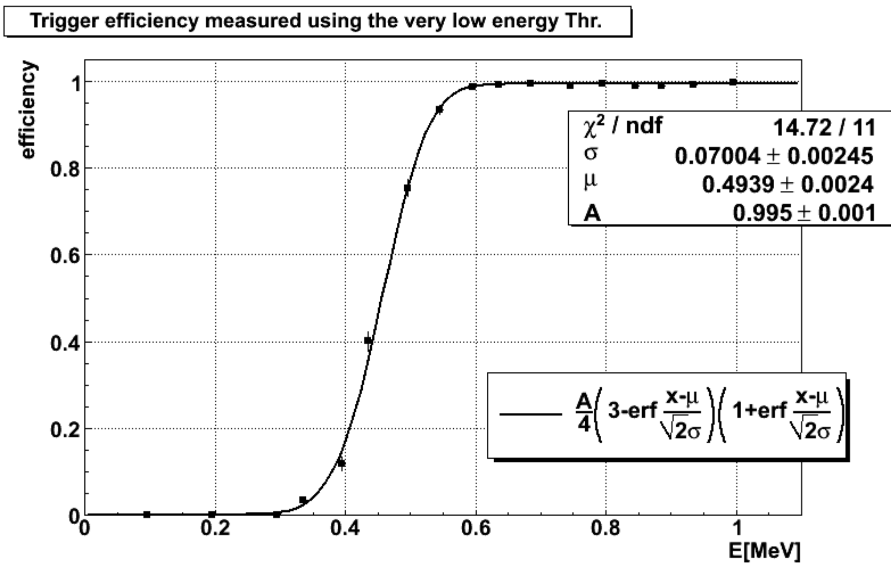

Figure 5.18: **The simulated trigger system efficiency for gamma fill-events, using the measuring method based on the low energy threshold.**

Case	σ	E_{th}	Ampl.	VMR
Reference(fill)	55.76	456.44	98.6	0.12
MeasLowThr(fill)	57.4	455.75	99.5	0.13

Table 5.6: **The simulated trigger system efficiency parameters for gamma fill-events, using the measuring method based on the low energy threshold**.

5.3.3 Measuring the Trigger Efficiency With Random Triggers

Another possibility for measuring the trigger efficiency foresees the using of random triggers generated by the trigger master board. The random triggers have a fixed rate therefore are not connected to the physics events. As in the case of the low energy triggers, a higher background rate may limit the frequency of the random trigger due to the DAQ read-out limitations. When the DAQ system receives a random trigger, a full read-out of the detector is performed. In this way, the deposited energy is known. Using this information, the trigger efficiency is the fraction of the events triggered at a given threshold from the total random trigger events at a given energy.

5.3.4 Measuring the Trigger Efficiency Using the Redundancy of the Central Region Trigger Boards

The particularities of the Double Chooz trigger design suggest a method to measure the trigger efficiency based on the redundancy of the central region boards. In order to describe this method, we are referring to the central region trigger boards as the boards A and B.

Let's suppose that the board A triggers on N_A from a "total" of N_B^{tot} events triggered by the other board, B. One can define the board A efficiency relative to the board B as:

$$\varepsilon_A = \frac{N_A}{N_B^{tot}} \tag{5.16}$$

And analogue for the board B:

$$\varepsilon_B = \frac{N_B}{N_A^{tot}} \tag{5.17}$$

Supposing uncorrelated data between boards, the trigger efficiency is given by the following relation:

$$\varepsilon_{A \vee B} = \varepsilon_A + \varepsilon_B + \varepsilon_A \varepsilon_B = 1 - (1 - \varepsilon_A)(1 - \varepsilon_B) \tag{5.18}$$

The triggered events belong to one of the following categories:

$\widehat{A}$ are the events triggered by board A, and not triggered by board B.

$\widehat{B}$ are the events triggered by board B, and not triggered by board A.

$\widehat{AB}$ are the events triggered by both boards, A and B.

Using this event classification, relations (5.16) and (5.17) can be rewritten as:

$$\varepsilon_A = \frac{\widehat{AB}}{\widehat{A} + \widehat{AB}} \tag{5.19}$$

$$\varepsilon_B = \frac{\widehat{AB}}{\widehat{B} + \widehat{AB}} \tag{5.20}$$

Replacing (5.19) and (5.20) in (5.18), delivers:

$$\varepsilon_{A \vee B} = 1 - \frac{\widehat{A}\widehat{B}}{(\widehat{A} + \widehat{AB})(\widehat{B} + \widehat{AB})} \tag{5.21}$$

Using equation (5.21) on simulated Double Chooz data one obtains the plot from figure (5.19).

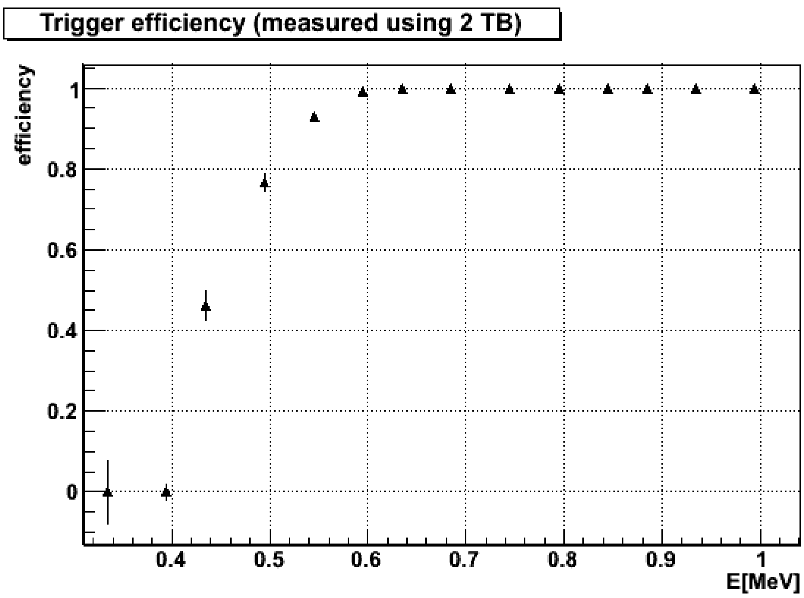

Figure 5.19: **The simulated trigger system efficiency for gamma fill-events, using the measuring method based on the redundancy of the central region trigger boards.** The trigger parameters are set to same values as in figure (5.8).

This method of measuring the trigger efficiency is based on the independence of the trigger boards and considers non correlation between the decisions of the central region trigger boards. The events letting energy depositions much smaller respectively much bigger than the threshold energy produce opposite decisions of the trigger boards. The low energy events trigger any trigger board respectively the high energy events trigger both trigger boards.

The plot (5.19), shows that for energies below 400 KeV, efficiency values are close to zero therefore the triggered events belong in general to the categories $\widehat{A}$ or $\widehat{B}$. For energies above 600 KeV the trigger efficiency from figure (5.21) becomes close to one. This effect is given by events belonging to the $\widehat{AB}$ category.

The difference between the trigger efficiency from figure (5.8) and the trigger efficiency from figure (5.19) is shown in figure (5.20). This correction aims to adjust the measured trigger efficiency to the value given by the Monte Carlo simulations.

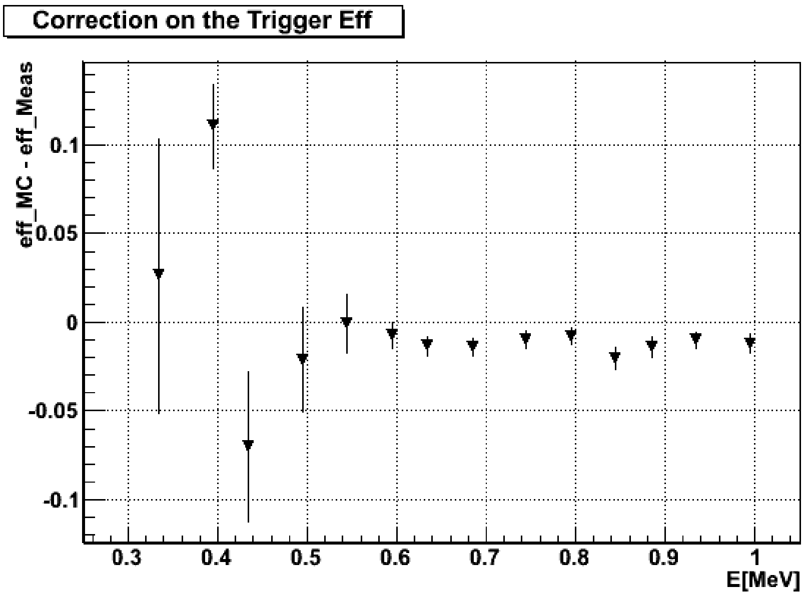

Figure 5.20: **Correction for the method based on the redundancy of the central region boards.** This figure shows the difference between the trigger efficiency represented in figure (5.8) and the method based on the redundancy of the central region trigger boards represented in figure (5.19).

At this point one has to notice the distinction between the simulated efficiency represented in figure (5.8) and the measured trigger efficiency from figure (5.19). The measured efficiency is, in fact, the efficiency of the algorithm based on expression (5.21) for **already triggered** events. The efficiency close to unity for high energy in figure (5.19) means "almost all the triggered events at this energy".

5.3.5 The Trigger Calibration

The calibration of the normal and low trigger thresholds can be archived by using radioactive sources. For higher energies, the threshold values can be linearly deduced from those at lower energies (figure 5.21). In addition, the laser systems deployed in different detector regions are used for the calibration of detector beyond the energy range of the radioactive sources [42].

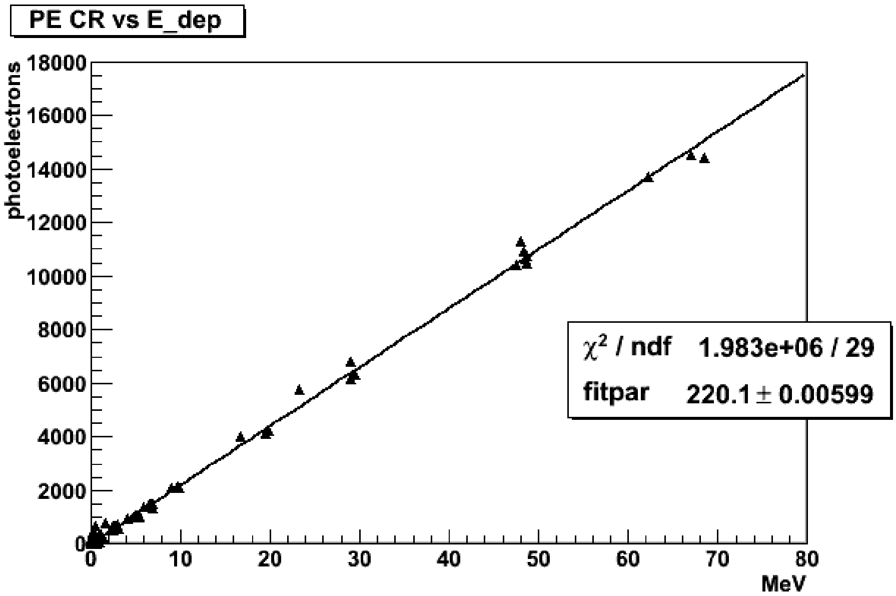

Figure 5.21: **The Double Chooz photoelectron response versus visible energy for central region gamma events**.

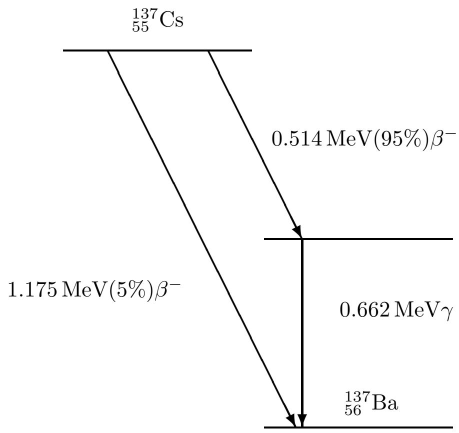

Figure 5.22: **The decay scheme of** ^{137}Cs [59].

The main trigger threshold for central region events, 0.5 MeV, can be established using the ^{137}Cs radioactive source. The low trigger board threshold foreseen at 0.3 MeV can be established using a ^{203}Hg source. The decay schemes of these radioactive isotopes are shown in figures (5.22) and (5.23). The ^{137}Cs and ^{203}Hg

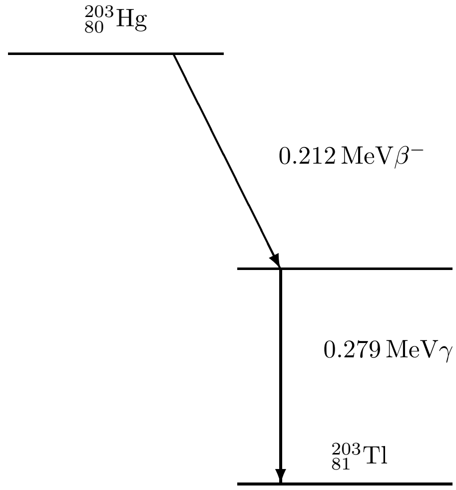

Figure 5.23: **The decay scheme of** ^{203}Hg [59].

sources used for calibration are encapsulated, thus only the gammas generated in their decay chains generate photoelectrons in the detector. ^{137}Cs will generate 0.662 MeV gamma energy deposition and ^{203}Hg will generate 0.279 MeV gamma energy deposition.

The trigger efficiency for central deployment is given in figure (5.7). For 0.5 MeV threshold and 0.662 MeV events, the trigger efficiency has to be close to one. For 0.3 MeV threshold and 0.279 MeV events, the trigger efficiency is close to 4 % due to the multiplicity condition.

5.4 Trigger Efficiency for Central Region Events

As it has been previously discussed, the Double Chooz trigger system is designed to be highly efficient for all kinds of predicted events. The main threshold will be about 0.5 MeV, substantially below the energy depositions related to antineutrino events.

5.4.1 Antineutrino Events

Reactor antineutrinos are detected by the inverse beta decay reaction, as mentioned previously. The two reaction products are detected as an initial event: the positron annihilation, and a delayed event: the neutron capture. The time difference between them is given by the thermalization time of the neutron, 10 to 100 μs. The visible energy released by the positron allows to measure the antineutrino energy using relation (2.3). This energy represents only a fraction of the visible energy released by the positrons inside the scintillator. The other contribution comes from the positron annihilation, yielding two 511 KeV gammas. The detector response for positrons from the inverse beta decay is represented in figure (5.24). The trigger system efficiency in this case is 100 % − 0.1 % (stat.) considering a 0.5 MeV threshold and events homogeneously distributed in the target volume.

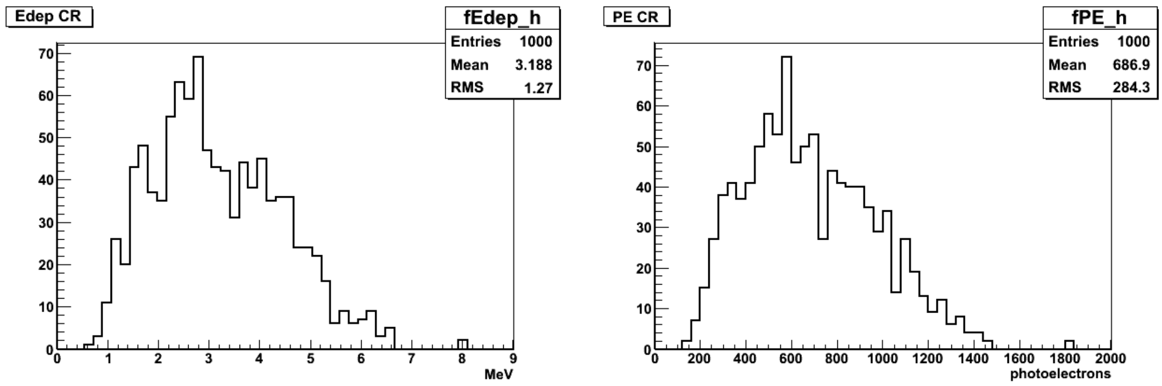

Figure 5.24: **The simulated Double Chooz response to the inverse beta decay positrons.** The left side represents the visible energy and the right side, the amount of light observed in units of photoelectrons. The events are homogeneously distributed in the target volume. The visible energy released by the positrons is correlated with the antineutrino energy as shown by relation (2.3).

The detector response to neutrons is different, depending on whether hydrogen (free proton) or gadolinium captures the neutron. This situation is shown by figure (5.25). The peak at 2.2 MeV corresponds to the gamma radiation released in deuteron formation. The gammas released by the neutron capture on gadolinium nuclei correspond to the high energetic peak in figure (5.25).

As shown in chapter (3), the Double Chooz trigger anticipates a neutron threshold at 5 MeV. In consequence, the neutrons captured on hydrogen are seen in the the same events class as the inverse beta decay positrons. The distinction between the antineutrino related particles is a task of the online data reducer (presented in chapter 2), and further, of the offline event reconstruction. The energy released from the neutron capture on gadolinium is usually large enough to trigger the 5 MeV threshold and these events are included in the neutron class. The trigger efficiency for neutrons is 100 % − 0.2 % (stat.) for the 0.5 MeV threshold and 75 % ± 0.2 % (stat.) for the neutron threshold.

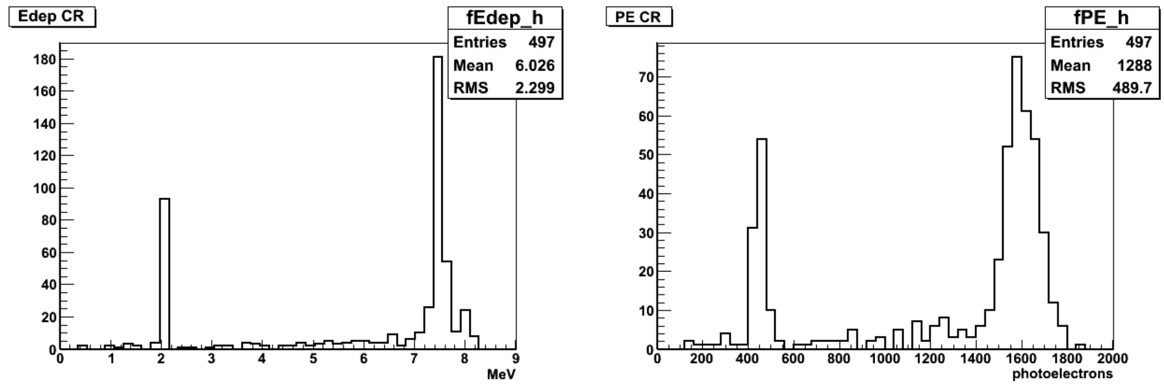

Figure 5.25: **The Double Chooz response to the inverse beta decay neutrons.** The left side represents the visible energy, the right side, the amount of light observed in units of photoelectrons. The events are homogeneously distributed in the target volume.

5.4.2 Background Events

The background rate from cosmic ray muons is large, especially for the near detector. Here, the aim is not to reject the background, but to properly tag it, allowing for the later data analysis a more elaborated background handling.

This increases the importance to have a fast and efficient trigger for all types of background events. Since the event rates from natural radioactivity and cosmic rays are not precisely known prior to the experimental start up, the trigger hardware implementation has to be flexible enough to accommodate a reconfiguration of the algorithm during the Double Chooz commissioning phase.

External Background

The cosmogenic background is the most abundant component of the trigger rate. The cosmogenic muons can traverse one or more detector regions with significant energy depositions in the form of scintillator light and Cherenkov radiation. The muons might produce fast neutrons via spallation process. In muon spallation, an incoming muon interacts with a nucleus via an exchange of a virtual photon. The nucleus subsequently emits neutrons (or pions) [62]. The Feynman diagram of this process is shown in figure (5.26).

In addition, fast neutrons might be produced by negative muons which stop in the detector or in the neighbouring rock of the detector and interact with protons via the reactions [61]:

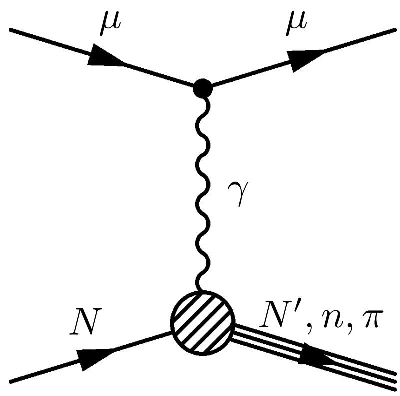

Figure 5.26: **Muon spallation**.

$$\text{OMC:} \qquad \mu^- + p \rightarrow n + \nu_\mu \tag{5.22}$$

$$\text{RMC:} \qquad \mu^- + p \rightarrow n + \nu_\mu + \gamma \tag{5.23}$$

Reaction (5.22), called "ordinary muon capture" (OMC) is the capture of a negative muon from the atomic orbital without emission of a gamma photon. Reaction (5.23), is called "radiative muon capture" (RMC) and is a rare process.

These processes are hard to quantify analytically. Thus a Monte Carlo treatment is needed to simulate the neutron yields. For Double Chooz, the production rate of neutrons generated from cosmogenic muons is presented in table (2.1).

As shown in chapter (3), the predicted muons event rate at the near site is $\sim$80 Hz for central region events. The data acquisition system is not able to digitize all photomultipliers pulse shapes at this rate, therefore a selection of the most important categories of background events has to be done [51].

The trigger algorithm has the ability to tag different muon signatures in the inner veto, as will be discussed in section (5.5.1). For the central region, the visible energy is far above the muon trigger threshold (50 MeV) for the muons traversing the scintillator volumes. The muons which hit only the inner veto and the buffer regions can generate a PMT signal by Cherenkov radiation inside the central region. If the muon path inside the buffer is sufficiently long, the visible energy deposition might be above the muon threshold. Otherwise, the muon events will be triggered by the inner veto as shown in figure (5.27).

The trigger system efficiency for cosmogenic muons is $100\,\% - 0.1\,\%$ (stat.).

As previously described, muons can create fast neutrons in the neighboring

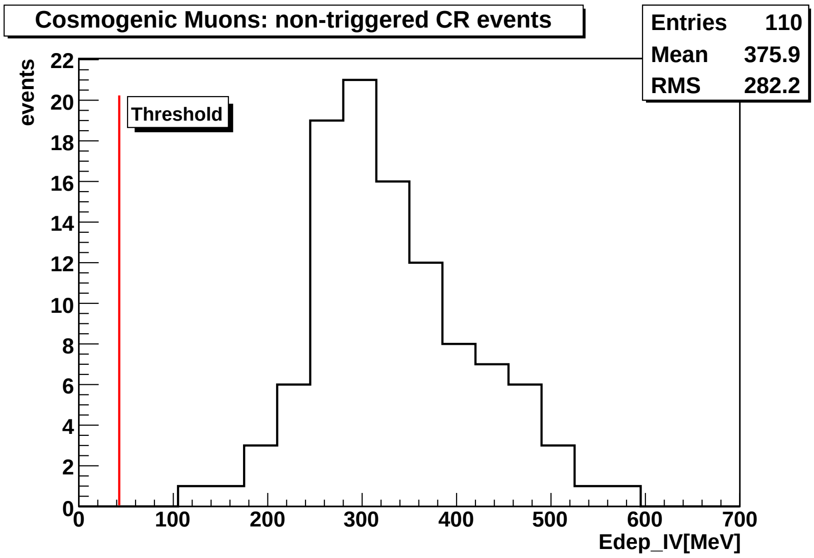

Figure 5.27: **The visible energy generated inside the inner veto by the cosmogenic muons which do not trigger the central region muon threshold.** The vertical red line shows the inner veto trigger threshold for muons events.

rock, close to detector. The neutrons deposit their energy via multiple scatterings, and, after thermalization, can mimic the delayed signal of antineutrino events. The energy depositions created by neutron scatterings might have the same energy range as the prompt signal of antineutrino events.

The simulated trigger efficiency for neutrons generated by cosmogenic muons is $94\,\% \pm 1.5\,\%$ (stat.).

For this simulation, only those events which release a visible energy deposition inside the central region volumes have been considered.

Internal Background

Another source of background is given by the gamma emissions of decaying isotopes. The Double Chooz detector design considers passive elements aiming to substantially reduce the contribution from these gammas reaching the active volumes. A measure against gamma emissions generated by radioactive elements in the exterior of the detector is the passive steel shield (figure 2.5). The allowed concentrations of the radioactive elements inside the detectors components are strictly controlled at a low level.

A major contribution to the low energy background is expected to be provided by radioactive elements in the glass of the photomultipliers [42]. It is known that the

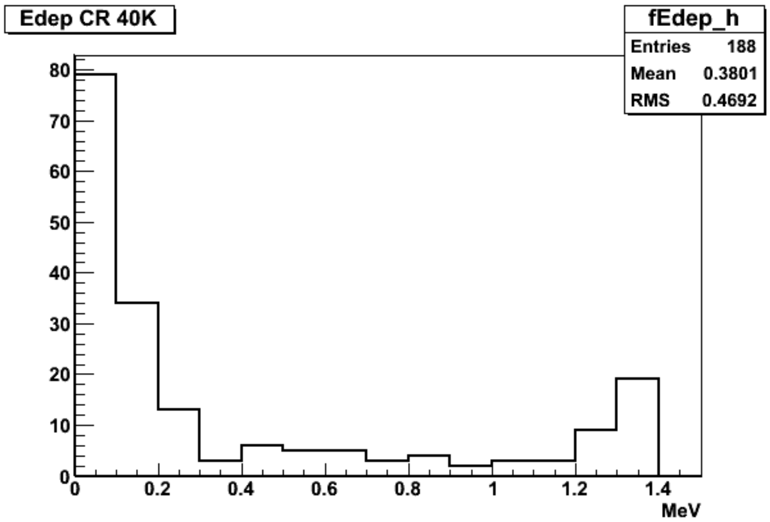

Figure 5.28: **The visible energy created by the ^{40}K from photomultipliers glass in the central region volumes.** The peak at ∼1.4 MeV is the 1.461 MeV gamma emission of the ^{40}Ar branch of the decay.

PMT glass contains radioactive potassium, uranium and thorium impurities. Due to the non-scintillating buffer which surrounds the active volumes of the central region, the rate of these energy depositions is expected to be low, as shown in chapter (3).

In order to simulate the trigger efficiency for low energy background events, one considers only those events which release a visible energy deposition inside the central region volumes. This is shown in figure (5.28) for ^{40}K events and in figure (5.29) for ^{232}Th events. The radioactive impurities have been generated inside the glass of photomultipliers.

For the 0.5 MeV threshold, the trigger efficiency for ^{232}Th events is 32% ± 2.9 % (stat.), and for ^{40}K events is 31% ± 3.4% (stat.).

5.5 The Trigger Efficiency for Inner Veto Events

As shown in chapter (3), the trigger system identifies incoming muons and neutrons by their energy depositions.

For the same deposited energy, the number of visible photoelectrons is smaller for the inner veto than for the central region due to the smaller coverage of the inner veto PMT. In figure (5.33), the inner veto response in terms of photoelectrons versus visible energy is shown for cosmogenic muons which hit the detector. These

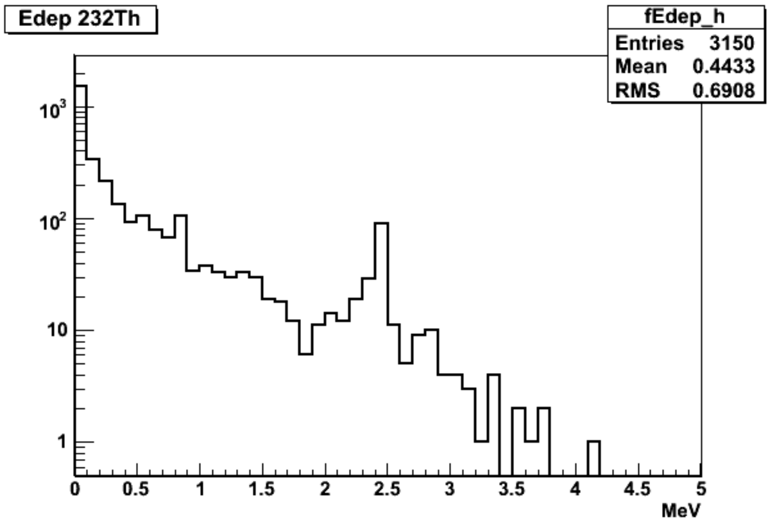

Figure 5.29: **The visible energy created by ^{232}Th from photomultipliers glass in the central region volumes.** The peak at ∼2.4 MeV correspond to the 4.99 MeV β^- emmision of the ^{208}Tl from the ^{232}Th decay chain. The peak at ∼0.8 MeV is the 2.13 MeV β^- emission of the ^{228}Ac.

energy depositions are proportional to the length of the muon paths inside the inner veto. The maximum lies around $E_{vis} = 290$ MeV and $18 \cdot 10^3$ photoelectons (figure 5.33-left) and is related to the angular dependence of the muon flux. Assuming an average energy deposition by muons $\epsilon_{dep} \simeq 2$ MeV/cm [63] and the thickness of inner veto: th = 60 cm [42], the average angle Â of the incoming muons (figure 5.30) can be computed as:

$$\hat{A} = \arccos\left(\frac{2 \cdot th \cdot \epsilon_{dep}}{E_{vis}}\right) \tag{5.24}$$

and is found to be $\simeq$ 34 degrees. In relation (5.24), it is assumed that the energy depositions around E_{vis} are made by muons which cross two times the inner veto (figure 5.30).

Figure (5.31) shows the inner veto trigger board efficiency as function of the threshold for cosmogenic muons and neutrons. A high efficiency of triggered muons (98%) and a low efficiency of miss-triggered neutrons as muons (43%) is achieved with a muon threshold at 3000 photoelectrons. This value corresponds to ∼ 45 MeV visible energy (figure 5.33-right), well below the minimum energy deposited by a muon which reaches the central region, (∼ 120 MeV). This is valid only for the muons which do not create energy depositions inside the detector chimney. In such cases the muons are properly tagged by the Double Chooz outer veto system.

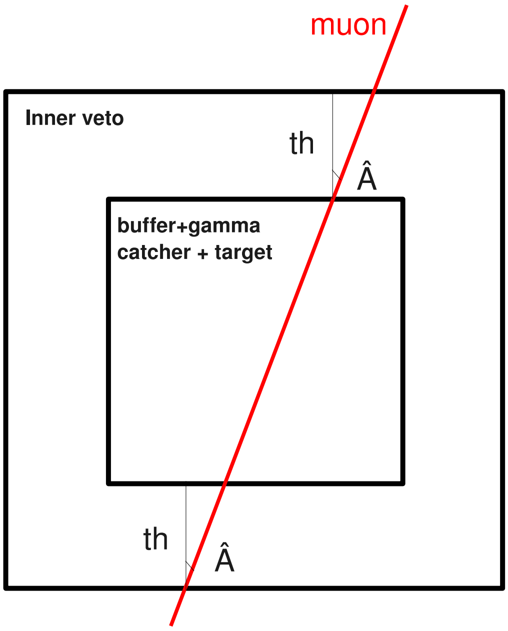

Figure 5.30: **The average angle of incoming muons.**

In conclusion, all the muons which hit the central region volume are triggered by the inner veto board as shown in figure (5.27).

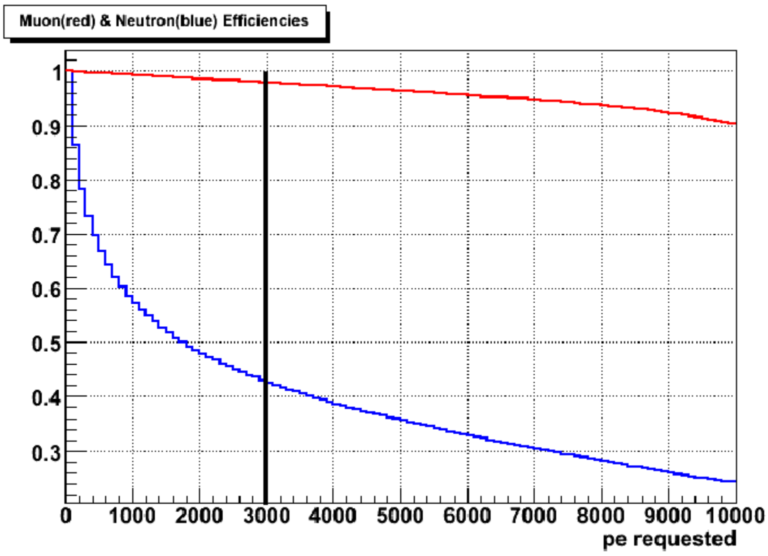

Figure 5.31: **The inner veto trigger board efficiency versus threshold for cosmogenic muons (red) and induced neutrons (blue).** The black vertical line represents the foreseen muon threshold of the inner veto trigger board.

The threshold which distinguishes the neutrons from the gammas rays generated by radioactive impurities is analyzed in figure (5.32). For this case, the trigger efficiency for gammas must be keep at a low level, typically below 10 %. A small value of the trigger efficiency for gammas from radioactive impurities results in a decrease of the trigger rate. The neutron threshold is established at 250 photoelectrons, such that the trigger efficiency for neutrons in the inner veto is better than 75 %.

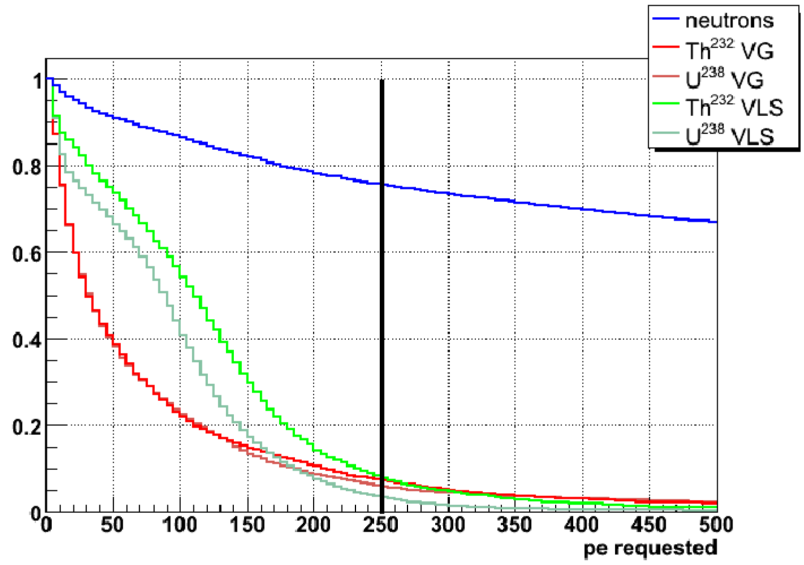

Figure 5.32: **The inner veto trigger board efficiency versus threshold for background neutrons and radioactive impurities.** For this simulation, the radioactive isotopes has been generated inside the glass of the inner veto PMT (VG) and inside the inner veto liquid scintillator (VLS). The black vertical line represents the foreseen neutron threshold of the inner veto trigger board.

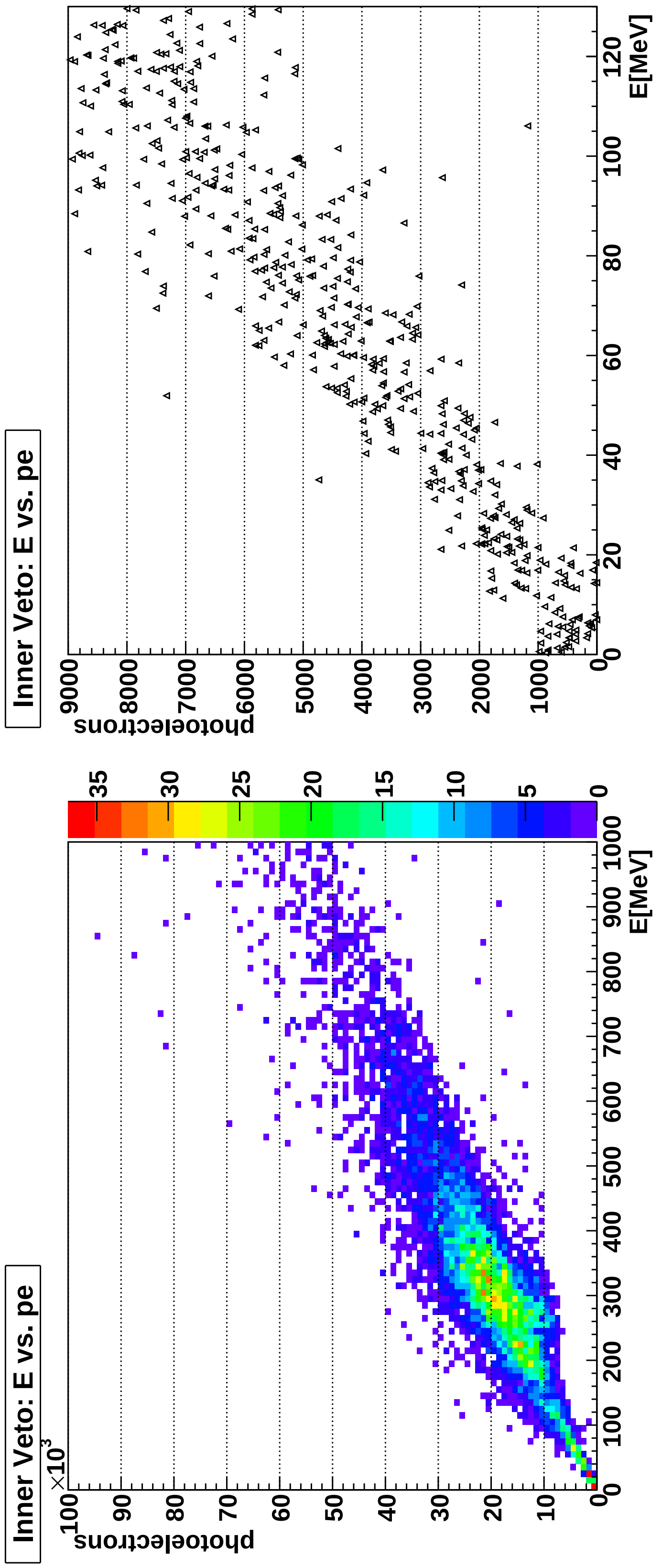

Figure 5.33: **The inner veto photoelectrons response versus visible energy for cosmogenic muons.** The plot from the right side shows the low energy depositions. These are typically made by muons which do not hit the inner detector.

5.5.1 The Inner Veto Muon Pattern Recognition Algorithm

The online identification of different muon categories was first time proposed inside the Double Chooz collaboration in 2005. Since then, two algorithms aiming to identify inner veto muon classes have been presented.

Chronologically, the first algorithm [60] was planned to be implemented inside the online data reducer and to use information from the trigger system.

The muon identification algorithm presented in this thesis [64] called Inner Veto Muon Pattern Recognition (IVMPR) is designed to be implemented inside the Double Chooz trigger system, as part of the trigger algorithm. The decisions provided by the IVMPR are transmitted via the trigger word and are used by the online data reducer for adjusting the amount of information which is saved.

The aim of IVMPR is the identification of the following muons categories (figure 5.34):

Crossing muons are those muons which cross the active volumes of the central region. The crossing muons can produce energy depositions inside the target volume and/or inside the gamma catcher. They enter the inner veto and the buffer volume, two times: first time, before reaching the buffer region and second time after leaving the buffer.

Passing muons are the muons which do not enter in the buffer region. The passing muons create light only inside the inner veto.

Stopping muons are the muons which enter and stop in the gamma catcher or in the target. These muons enter the inner veto region only once.

The muons which cross only the inner veto and the buffer region are not included in the previous classification. This kind of muons, called **buffer muons**, do not generate clear signatures due to the non-scintillating buffer liquid. However, they can generate, through Cherenkov radiation, large energy depositions which may be misidentified as crossing or stopping muons. Otherwise, they are identified as passing muons.

In order to test the muon recognition algorithm, a sample of simulated cosmogenic muons has been used [65]. The previous muon categories including the buffer muons can be identified directly from the simulated data (**generated muons**). This way provides a reference for the algorithm testing. The muons categories from the simulated data sample, in this case without the buffer muons, are also identified by IVMPR (**recognized muons**).

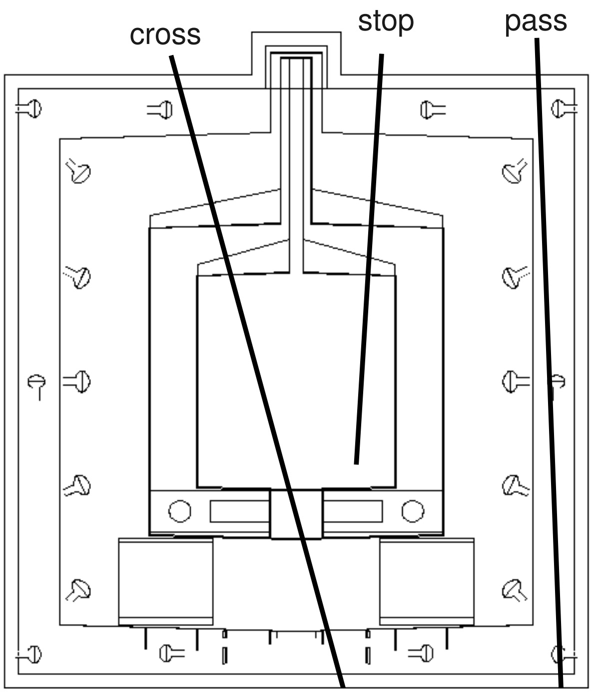

Figure 5.34: **The muon categories considered by the Inner Veto Muon Pattern Recognition.**

In conclusion, there are 4 generated muons categories: passing, crossing, stopping and buffer muons, and three recognized muons categories, namely: passing, crossing and stopping muons.

The Formalism

The number of events present in each of the generated (gen) or the recognized (rec) categories is N_i^{gen}, with i = p,c,s,b (i.e. pass, cross, stop, buffer) respectively N_j^{rec}, with j = p,c,s (i.e. pass, cross, stop). The total number of events is the same:

$$\sum_{i=p,c,s,b} N_i^{gen} = \sum_{j=p,c,s} N_j^{rec} \tag{5.25}$$

The testing foresees a comparison of the results from the generated and the recognized categories in order to select the correctly and the wrong recognized events.

The notation considers N_{pc} as the events which are identified by the IVMPR as being passing muons (rec = p), but are generated as crossing muons (gen = c). The similar convention is used for all the cases. By this way, the migration between muons classes of events can be estimated. As a rule of notation, the first index runs over rec and the second index runs over gen.

The good reconstructed events (i.e. found passing/stopping/crossing in both, rec and gen) are included in the categories: N_{pp}, N_{ss} and N_{cc}. Overall, one can consider that:

$$\begin{pmatrix} p \\ c \\ s \end{pmatrix}_{rec} = \begin{pmatrix} N_{pp} & N_{pc} & N_{ps} & N_{pb} \\ N_{cp} & N_{cc} & N_{cs} & N_{cb} \\ N_{sp} & N_{sc} & N_{ss} & N_{sb} \end{pmatrix} \begin{pmatrix} p \\ c \\ s \\ b \end{pmatrix}_{gen} \tag{5.26}$$

with

$$N_i^{gen} = \sum_j N_{ji} \quad ,i = p, s, c, b \tag{5.27}$$

$$N_j^{rec} = \sum_i N_{ji} \quad ,j = p, s, c \tag{5.28}$$

In the end, two types of normalizations on relation (5.26) have been applied. The first normalization is:

$$\begin{pmatrix} p \\ c \\ s \end{pmatrix}_{rec} = 100 \begin{pmatrix} \frac{N_{pp}}{N_p^{rec}} & \frac{N_{pc}}{N_p^{rec}} & \frac{N_{ps}}{N_p^{rec}} & \frac{N_{pb}}{N_p^{rec}} \\ \frac{N_{cp}}{N_c^{rec}} & \frac{N_{cc}}{N_c^{rec}} & \frac{N_{cs}}{N_c^{rec}} & \frac{N_{cb}}{N_c^{rec}} \\ \frac{N_{sp}}{N_s^{rec}} & \frac{N_{sc}}{N_s^{rec}} & \frac{N_{ss}}{N_s^{rec}} & \frac{N_{sb}}{N_s^{rec}} \end{pmatrix} \begin{pmatrix} p \\ c \\ s \\ b \end{pmatrix}_{gen} \tag{5.29}$$

and the second normalization:

$$\begin{pmatrix} p \\ c \\ s \end{pmatrix}_{rec} = 100 \begin{pmatrix} e_p & \frac{N_{pc}}{N_c^{gen}} & \frac{N_{ps}}{N_s^{gen}} & \frac{N_{pb}}{N_b^{gen}} \\ \frac{N_{cp}}{N_p^{gen}} & e_c & \frac{N_{cs}}{N_s^{gen}} & \frac{N_{cb}}{N_b^{gen}} \\ \frac{N_{sp}}{N_p^{gen}} & \frac{N_{sc}}{N_c^{gen}} & e_s & \frac{N_{sb}}{N_b^{gen}} \end{pmatrix} \begin{pmatrix} p \\ c \\ s \\ b \end{pmatrix}_{gen} \tag{5.30}$$

with $e_p \equiv N_{pp}/N_p^{gen}$, $e_s \equiv N_{ss}/N_s^{gen}$ and $e_c \equiv N_{cc}/N_c^{gen}$.

One can notice as a first observation, the unitarity of the matrix lines for the first normalization (5.29) and of the columns for the second normalization (relation 5.30). As previously mentioned, for each normalization, the good recognized events are those from the first diagonal.

Expression (5.29) represents the sample decomposition, indicating the generated sources of the recognized events. For example the first line of the matrix from expression (5.29) shows that all the N_p^{rec} events (i.e. identified by the algorithm as being passing muons) represents a sum of events which was generated as passing muons (N_{pp}), as crossing muons (N_{pc}), as stopping muons (N_{ps}) or as buffer (N_{pb}) muons.

Expression, (5.30) represents the algorithm efficiencies, indicating the recognized destination categories of the generated events. It is an opposite approach to expression (5.29). As an example, the first column of the matrix from expression (5.30) shows that all the N_p^{gen} events (i.e. generated as passing muons) represents a sum of events which was identified by the algorithm as being passing muons (N_{pp}), as being crossing muons (N_{cp}), or as being stopping muons (N_{sp}).

The Algorithm

The IVMPR algorithm is expressed as:

$$Pass : \overline{Ecr} \wedge Eiv$$

$$Cross : Ecr \wedge Eiv \wedge Topology$$

$$Stop : Ecr \wedge Eiv \wedge \overline{Topology}$$

with

Topology = ($>$ 3 Lateral groups) $\vee$ ($\geq$ 1 Down group) $\vee$ (Bottom)

where:

Ecr and Eiv are the muon thresholds for central region and for inner veto. As has been previously discussed, Ecr will be set at 50 MeV energy deposition and Eiv at ∼45 MeV.

Lateral, Down, Bottom from the Topology condition are the inner veto PMT group areas as presented in chapter (4). The group thresholds are specific for each PMT group area. The values are given in table (5.7) and in figures (5.37), (5.36) and (5.35).

Group Area	Lateral	Down	Bottom
Threshold[photoelectrons/PMT]	120	96	12

Table 5.7: **The threshold values for inner veto group areas.**

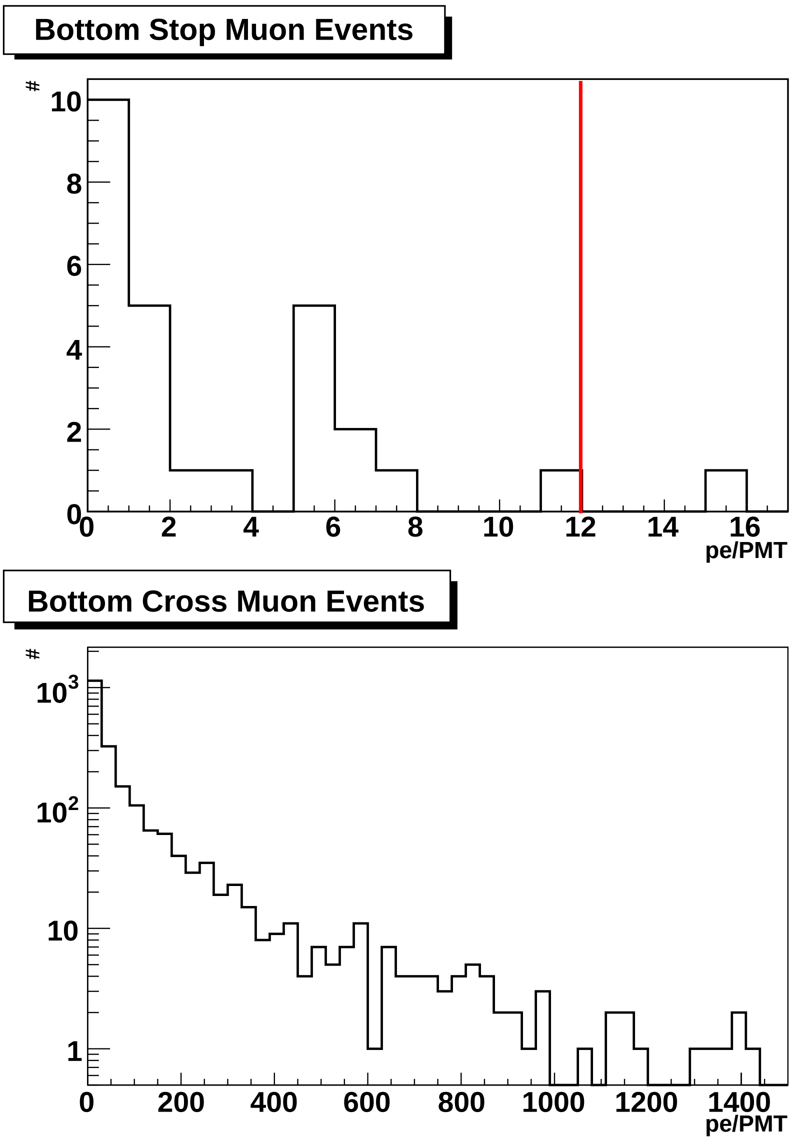

Figure 5.35: **The photoelectrons response generated by the crossing and by the stopping muons in the bottom group area.** The red vertical line indicates the foreseen group threshold.

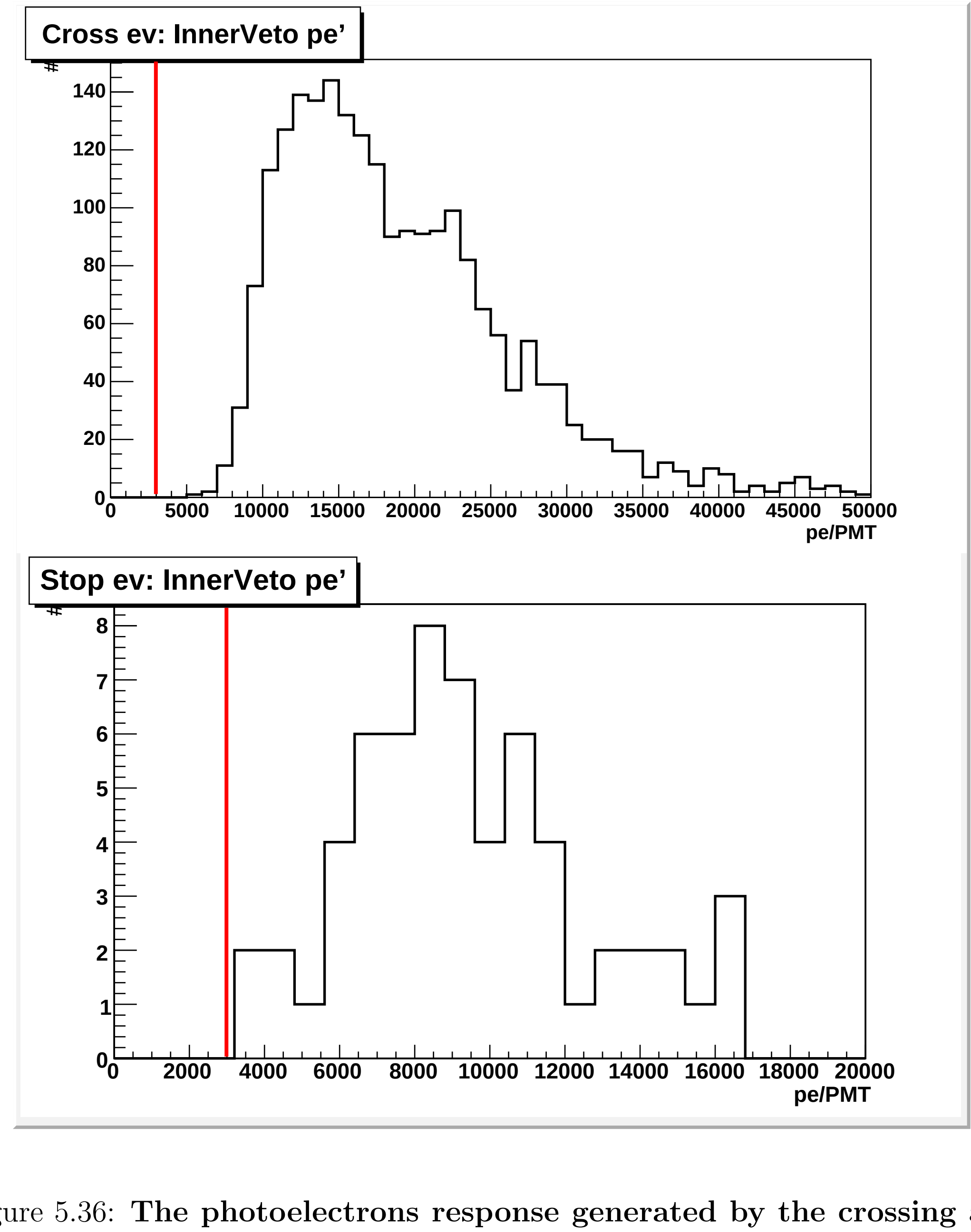

Figure 5.36: **The photoelectrons response generated by the crossing and by the stopping muons inside the inner veto region.** The red vertical line indicates the foreseen Eiv threshold.

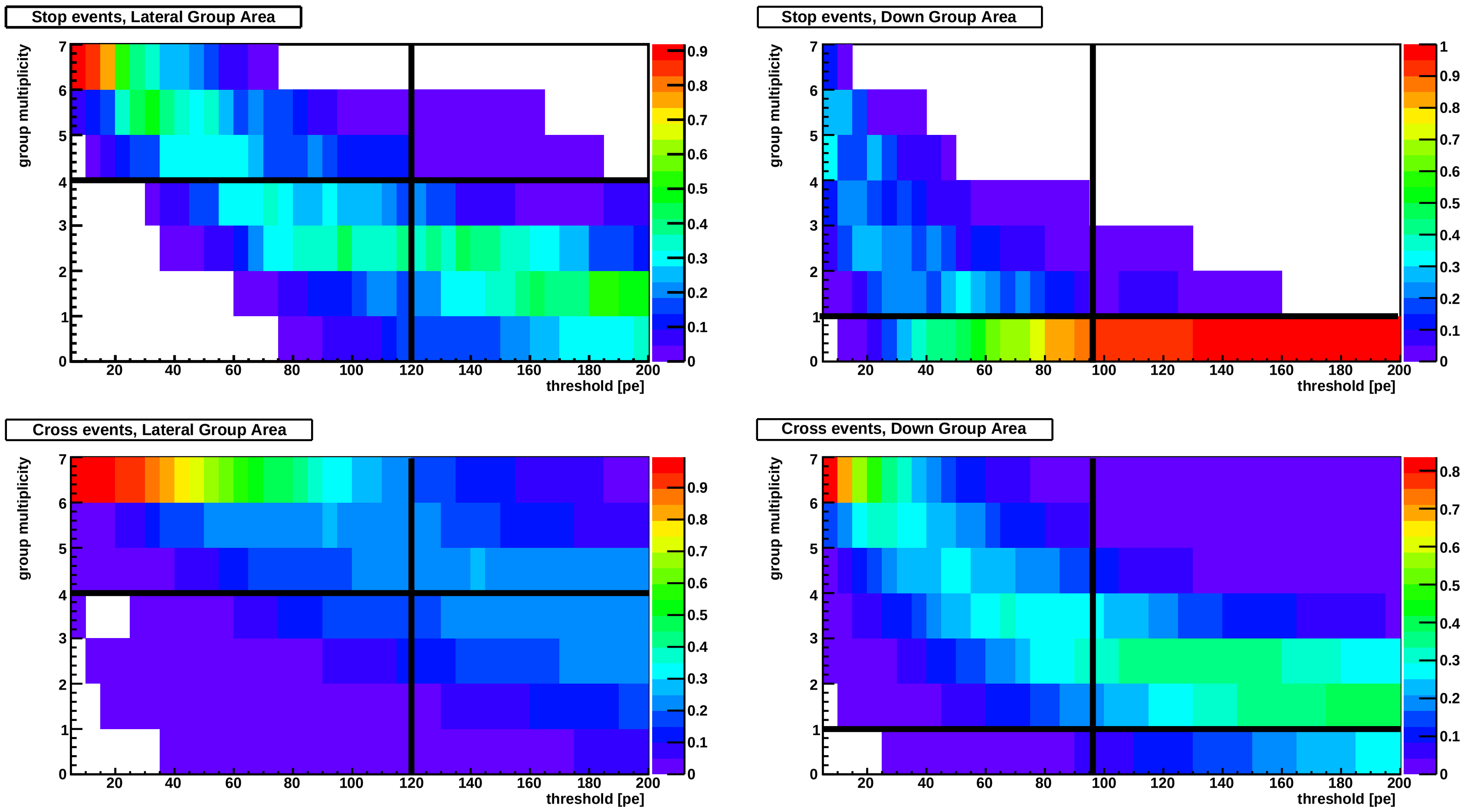

Figure 5.37: **The group multiplicity versus group threshold for the crossing and for the stopping muons in the lateral and in the down PMT group area.** The vertical lines indicate the foreseen group thresholds. The horizontal black lines indicate the multiplicity conditions of the IVMPR algorithm.

The Results

As an overview on the results provided by IVMPR, figure (5.38) indicates the distribution of the muon categories for generated and recognized events. This figure shows that the majority of the buffer muons are recognized as passing muons. This is due to the small amount of light created by passing muons in the central region. The other muon classes have similar proportions.

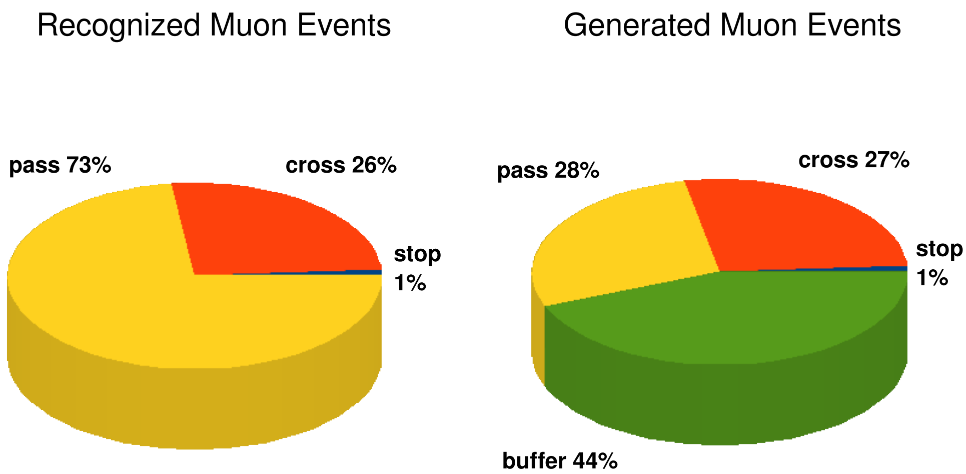

Figure 5.38: **The relative distributions of the muon categories.**

Figure (5.38) does not offer information on the mixing between the different categories. For example, it is not clear if the 1% recognized stopping muons are also the generated stopping muons. Therefore, a more elaborated presentation of the results based on relations (5.29) and (5.30) is required.

Using the normalization from relation (5.29) the IVMPR results are expressed as:

$$\begin{pmatrix} p \\ c \\ s \end{pmatrix}_{rec} = \begin{pmatrix} 37 & 2 & 0 & 61 \\ 0 & 100 & 0 & 0 \\ 0 & 7 & 93 & 0 \end{pmatrix} \begin{pmatrix} p \\ c \\ s \\ b \end{pmatrix}_{gen} \tag{5.31}$$

and using the normalization (5.30) as:

$$\begin{pmatrix} p \\ c \\ s \end{pmatrix}_{rec} = \begin{pmatrix} 100 & 6 & 5 & 100 \\ 0 & 94 & 13 & 0 \\ 0 & 0 & 82 & 0 \end{pmatrix} \begin{pmatrix} p \\ c \\ s \\ b \end{pmatrix}_{gen} \tag{5.32}$$

As expected, almost all of the buffer muons are recognized as passing muons. This is shown by the first line in (5.31) and by the last column in (5.32). The majority of generated passing muons are well recognized (first column in 5.32), but the recognized sample of passing muons using the IVMPR algorithm, contains only 37 % generated passing muons (first line in 5.31), the rest coming from the generated buffer muons.

The recognized crossing muons are 94 % generated as crossing muons (second line in 5.31 and the second column in 5.32), the rest of 6 % generated crossing muons are recognized as passing muons. This interpretation can also be applied to the stopping muons (last line in 5.31 and third column in 5.32). One finds that 7 % of the recognized stopping muons were generated as crossing muons, and 13 % of the generated stopping muons are recognized as crossing muons.

5.6 Summary

The design of the Double Chooz trigger has been investigated with simulated event samples. Data processing procedures have been elaborated in order to understand the trigger efficiency parameters.

The optimization of the trigger algorithm results in a set of parameters able to ensure a high efficiency for all kinds of foreseen events. The dependence of the trigger performance on the variation of the several detector parameters has also been investigated.

The trigger efficiency for simulated inverse beta decay events is 100 %. The trigger efficiency for background events is also high.

Overall, the design of the trigger system algorithm fulfills the requirements of the Double Chooz experiment.

Chapter 6

Conclusions

Neutrinos have been in the focus of fundamental research since Pauli proposed their existence. One crucial improvement on the present knowledge will be achieved by a high precision measurement of the mixing angle θ_{13}. The Double Chooz experiment can significantly improve the present θ_{13} limit.

Double Chooz uses two identical detectors at different distances from the source in order to increase the precision of the measurement. The detectors are optimized for antineutrino detection and background tagging. The use of the same cavern as the predecessor experiment (CHOOZ) reduces the total costs and the construction time.

The Double Chooz trigger system aims to detect antineutrino and background events with very high efficiency. The trigger decisions are based on the discrimination of the PMT signals having amplitude proportional to the deposited energy in the detector. The main trigger threshold is established at $\sim$0.5 MeV, substantially below the energy of positron annihilation as result of an antineutrino event. The trigger uses three boards for processing the detector signals, two of them correspond to the central region and the third to the inner veto. The board decisions are evaluated by the trigger master board. The redundancy provided by the central region boards permits the detection of hardware failures and the measurement of the trigger efficiency from offline data.

The trigger board algorithm considers a minimum multiplicity of the photomultipliers groups as a measure against single noisy PMT. The event classes implemented by the trigger algorithm classifies physics and background events based on their energy depositions in different regions of the detector.

The trigger simulations aim to establish the trigger algorithm and to provide a set of parameters able to provide a high efficiency for all considered event classes. The trigger efficiency has been analyzed for different design configurations and thresholds.

The Double Chooz trigger design permits multiple methods for measuring its efficiency: not only "conventional" methods based on the use of a low energy threshold (0.3 MeV) or the use of a random trigger but also a "specific" method, based on the redundancy of the central region boards. The results can be crosschecked in order to increase the overall measurement precision.

The trigger efficiency for antineutrino events and various kinds of backgrounds has been tested using Monte Carlo data. The trigger efficiency for antineutrino events in central region is close to 100 %. The trigger efficiency for background events above 0.5 MeV is also close to 100 %.

Appendix A

The Event Rate of the Double Chooz Experiment

In the following, we consider an antineutrino detector having a fiducial volume filled with liquid scintillator and having a mass of t [tons]. The detector is placed at a distance L [km] from a reactor having power P [GW] and a load factor l [%]. Assuming no oscillations, the rate R [day^{-1}] of antineutrino events counted by experiment can be expressed [31] using following relation:

$$R = \frac{5.39 \cdot 10^{16} sec^{-1} \cdot P \cdot l \cdot <\sigma> \cdot t \cdot n_p}{W} \cdot \frac{1}{4\pi L^2} \tag{A.1}$$

where:
$<\sigma>$ [cm^2 · fission^{-1}] is the cross section of the inverse β-decay, averaged for the typical fuel composition during a reactor cycle (figure 1.4).
n_p [ton^{-1}] is the number of protons per ton in the fiducial volume of the considered detector.
W [MeV · fission^{-1}] is the released mean energy per fission.

By inserting the values of $<\sigma>_{fission}$, n_p and W from reference [31], relation (A.1) delivers:

$$R = 15.4 \frac{cm^2 \cdot ton^{-1} \cdot sec^{-1}}{MeV} \cdot \frac{P \cdot l \cdot t}{4\pi L^2} \tag{A.2}$$

One may assume that a detector placed at 1 km from a 1 GW reactor and having 1 ton of liquid scintillator in its fiducial volume will count ~1 event in 24 hours.

Inserting the values of the Chooz reactors: 2*4.27 GW power with an 80 % load factor and the target mass of a Double Chooz detector (10 tons), the interraction rate is expressed by the green line in figure (A.1). One may also consider the effect of neutrino oscillations on the event rate. This is represented by the red line in figure (A.1).

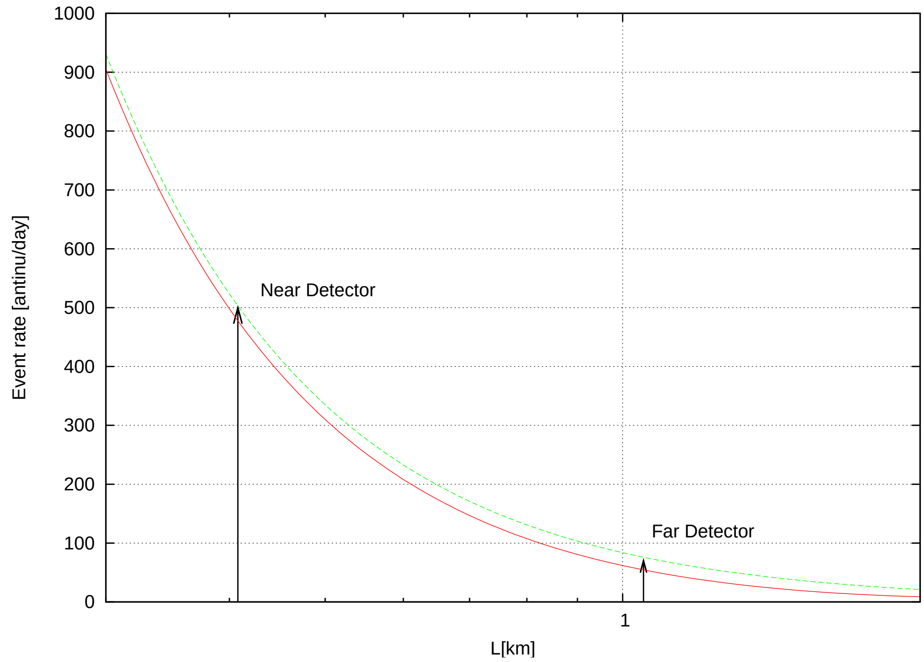

Figure A.1: **The Double Chooz event rate.** The green line indicates the event rate for the no oscillation case. The red line indicates the event rate for the oscillation case. The values of the oscillation parameters are those from reference [40]: $\sin^2\theta_{13} = 0.056$ and $|\Delta_{\text{atm}}| = 2.4 \cdot 10^{-3}\text{eV}^2$. For the reactor antineutrino energy, the mean value: 4.2 MeV [39] is assumed. The positions of the Double Chooz detector sites are indicated by arrows.

From figure A.1 one assumes for Double Chooz a rate of antineutrino events of ≈505 events/day for the near detector and ≈75 events/day for the far detector.

The main contribution to the total deadtime of Double Chooz is represented by the veto time applied offline after each muon event [42]. The deadtime T_d induced by background muons can be expressed as:

$$T_d = r_\mu \cdot \tau \qquad \text{(A.3)}$$

where r_μ is the muon rate and τ is the veto time applied after each muon event. For Double Chooz, $\tau = 500\,\mu\text{s}$ [42]. The rates of the background muons are: 250 Hz for the near site and 45.4 Hz for the far site (chapter 3). Using relation (A.3), the corrections due to deadtime result in a loss of ≈63 events/day for the near detector and ≈2 events/day for the far detector.

Appendix B

PMT Grouping Scheme

The PMT grouping scheme is described using the following numbering scheme:

photomultipliers: from 0 to 389 for the central region and from 390 to 467 for the inner veto.

trigger groups: from 0 to 12 for each of the central region trigger boards and from 0 to 17 for the inner veto board.

trigger boards: 0 and 1 for the central region trigger boards, 2 for the inner veto board.

This numbering scheme is the same as used by the Double Chooz simulation software [66]. Respecting the above notation, the PMT grouping scheme is described in table (B.1).

The correspondence between the PMT indexes and the geographical coordinates is shown in figure (B.1).

The photomultiplier grouping scheme is also implemented with the PMT cable labels. The cable labeling schemes for the central region and the inner veto are shown in figure (B.2) and respectively in figure (B.3).

Table B.1: The PMT grouping scheme.

Group	Board	PMT index
0	0	0 18 20 36 38 62 64 90 92 94 122 124 150 152 154 180
1	0	8 9 22 40 42 66 68 70 96 98 126 128 130 156 158 184
2	0	2 24 26 44 46 72 74 100 102 104 132 134 160 162 164 186
3	0	12 13 28 48 50 76 78 80 106 108 136 138 140 166 168 188
4	0	4 30 32 52 54 82 84 110 112 114 142 144 170 172 174 190
5	0	16 17 34 56 58 60 86 88 116 118 120 146 148 176 178 194
6	0	182 192 200
7	0	196 210 212 214 242 244 270 272 274 302 304 350 352 370 382 383
8	0	198 216 218 246 248 250 276 278 306 308 310 346 348 366 368 388
9	0	202 220 222 224 252 254 280 282 284 312 314 342 344 364 378 379
10	0	204 226 228 256 258 260 286 288 316 318 320 338 340 360 362 386
11	0	206 230 232 234 262 264 290 292 294 322 324 334 336 358 374 375
12	0	208 236 238 240 266 268 296 298 300 326 328 330 332 354 356 384
0	1	6 7 19 37 39 61 63 65 91 93 121 123 125 151 153 181
1	1	1 21 23 41 43 67 69 95 97 99 127 129 155 157 159 183
2	1	10 11 25 45 47 71 73 75 101 103 131 133 135 161 163 185
3	1	3 27 29 49 51 77 79 105 107 109 137 139 165 167 169 189
4	1	14 15 31 53 55 81 83 85 111 113 141 143 145 171 173 191
5	1	5 33 35 57 59 87 89 115 117 119 147 149 175 177 179 193
6	1	187 195 205
7	1	197 211 213 241 243 245 271 273 301 303 305 351 353 369 371 389
8	1	199 215 217 219 247 249 275 277 279 307 309 347 349 367 380 381
9	1	201 221 223 251 253 255 281 283 311 313 315 343 345 363 365 387
10	1	203 225 227 229 257 259 285 287 289 317 319 339 341 361 376 377
11	1	207 231 233 261 263 265 291 293 321 323 325 335 337 357 359 385
12	1	209 235 237 239 267 269 295 297 299 327 329 331 333 355 372 373
0	2	402 404 406 408 410 412
1	2	390 403 413
2	2	392 394 405
3	2	396 407 409
4	2	398 400 411
5	2	401 414 425 426 448
6	2	391 415 416 428 430
7	2	393 417 418 432 434
8	2	395 419 420 436 438
9	2	397 421 422 440 442
10	2	399 423 424 444 446
11	2	427 449 450 466
12	2	429 431 451 453
13	2	433 435 454 456
14	2	437 439 457 459
15	2	441 443 460 462
16	2	445 447 463 465
17	2	452 455 458 461 464 467

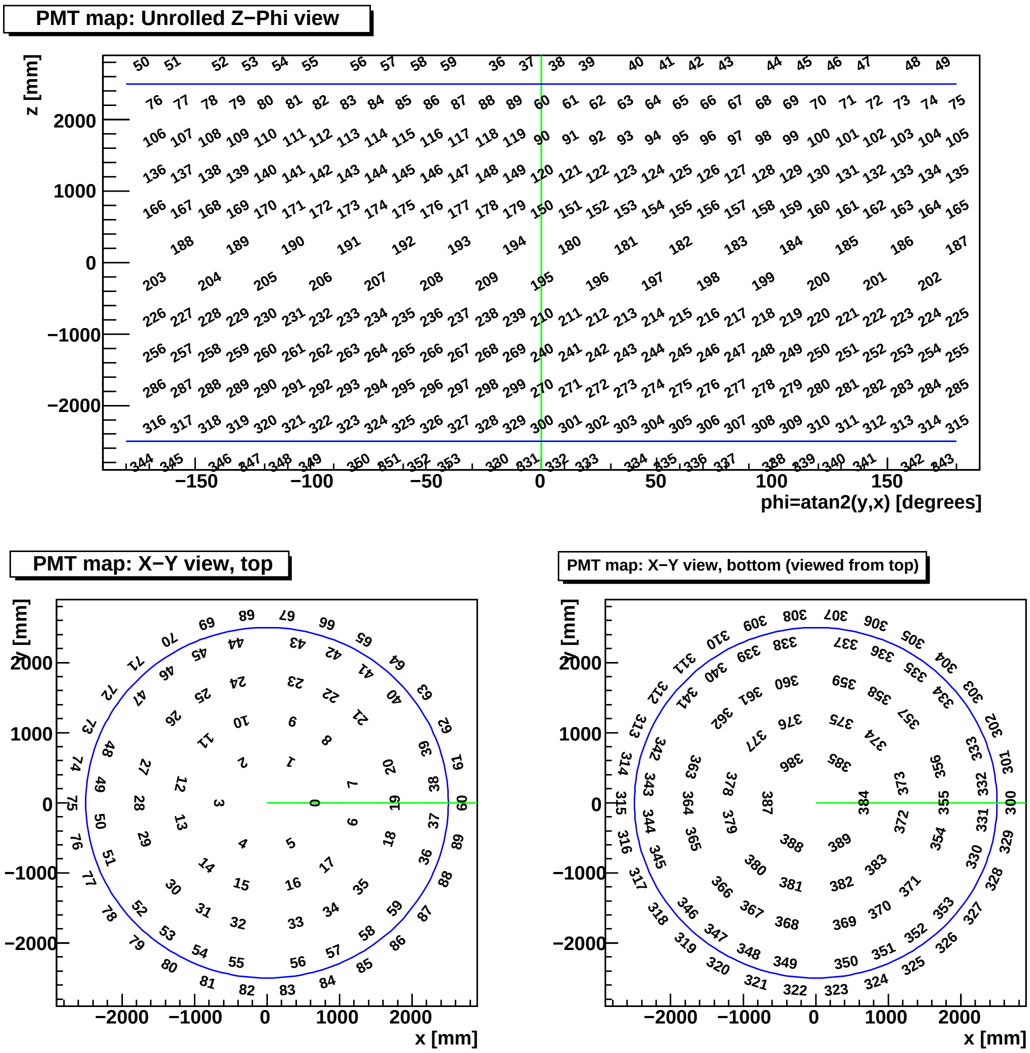

Figure B.1: **The central region PMT numbering scheme.** The photomultipliers encircled blue in lower plots have the same vertical coordinates. The horizontal blue lines in the upper plot correspond to the blue circles marked in the lower plots.

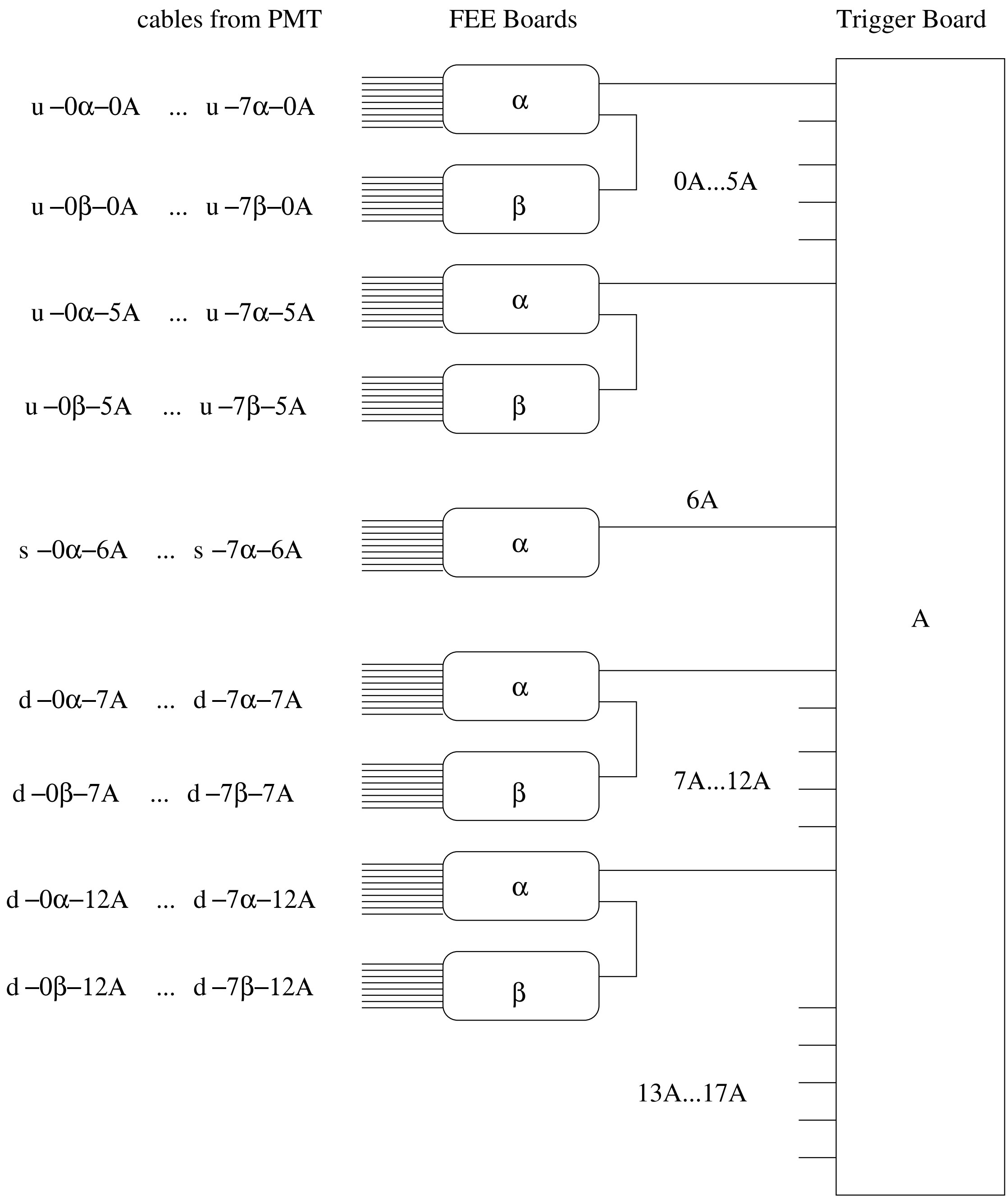

Figure B.2: **The labeling scheme of the central region PMT cables.**

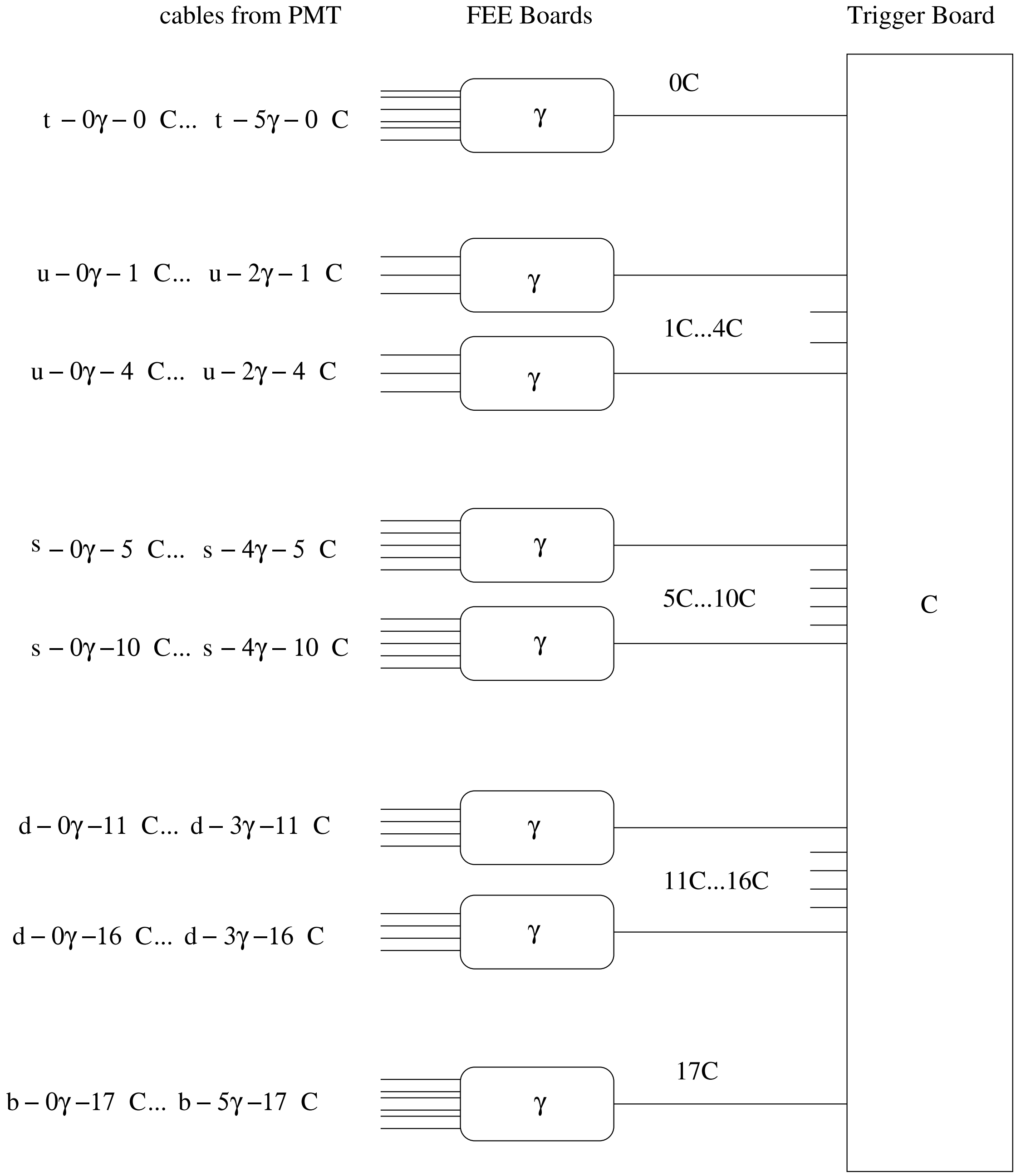

Figure B.3: **The labeling scheme of the inner veto PMT cables.**

Appendix C

The Error Function

The error function **"erf"** is defined as:

$$erf(x) = \frac{2}{\sqrt{\pi}} \int_0^x e^{-t^2} dt \tag{C.1}$$

If G(x) is the normal distribution (gaussian) function, the error function fulfills the following relation:

$$erf\left(\frac{x}{\sigma\sqrt{2}}\right) = \int_{-x}^{x} G(x)dx \tag{C.2}$$

If the results of a series of measurements are described by a normal distribution with a standard deviation σ and the expectation value 0, then $erf\left(\frac{x}{\sigma\sqrt{2}}\right)$ is the probability that the error of a single measurement lies between x and +x, for positive x.

The limits of the error function are:

$$\lim_{x \to +\infty} erf(x) = 1 \tag{C.3}$$

and for the negative values:

$$\lim_{x \to -\infty} erf(x) = -1 \tag{C.4}$$

At the origin,

$$erf(0) = 0 \tag{C.5}$$

The error function is odd:

$$erf(-x) = -erf(x) \tag{C.6}$$

For small x values, it can be expanded as:

$$erf(x) = \frac{2}{\sqrt{\pi}}\left(x - \frac{x^3}{3} + \frac{x^5}{10} - \frac{x^7}{42} + \frac{x^9}{216} - \ \dots\right) \tag{C.7}$$

while for the large values of x, an approximate expression can be obtained from:

$$erf(x) = 1 - \frac{e^{-x^2}}{\sqrt{\pi}x}\left(1 - \frac{1}{2x^2} + \frac{1\cdot 3}{(2x^2)^2} - \frac{1\cdot 3\cdot 5}{(2x^2)^3} + \cdots\right) \tag{C.8}$$

A graphical representation is given in figure:

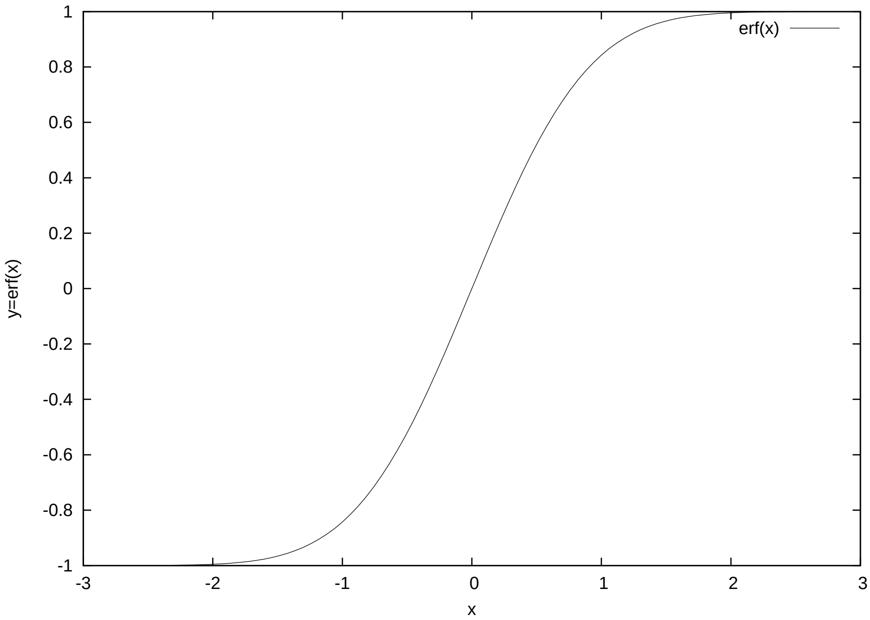

Figure C.1: **The Error Function.**

Appendix D

The Parameters of the Trigger Efficiency for Different Design Configurations

The Double Chooz trigger efficiency is discussed in chapter (5) for various design configurations. Table (D.1) and figure (D.1) present the summary of these simulation results.

Case	σ	E_{th}	Ampl.	VMR	C_σ	C_μ
Reference	55.76	456.44	98.6	0.12	1	1
Electronics included	61.97	511.41	98.6	0.12	1.11	1.12
20 PMT out of order	57.48	480.9	98.6	0.12	1.03	1.05
Multiplicity M_4	58.71	464.28	98.3	0.13	1.05	1.02
Group thr. $E_{gr} = 0.5$ pe/PMT	109.22	636.21	95.1	0.17	1.96	1.39
Up-down macro-grouping	64.37	403.12	98.9	0.16	1.15	0.88
All the PMT together	49.9	490.2	98.3	0.1	0.89	1.07
One trigger board	69.9	495.4	98.2	0.14	1.25	1.09
Central events	60.19	460	99.8	0.13	1.08	1.01

Table D.1: **The influence of the design configurations on the trigger efficiency parameters.** The "Reference" case, has the following parameters: interlaced macro-grouping, no electronics simulation included, multiplicity: M_2 (more than one PMT group above the group threshold), group threshold: $E_{gr} = 0.25$ pe/PMT, fill events. Other cases show the variation of the trigger efficiency if one parameter is different from the reference case. C_σ and C_μ show the deviation from the reference case: $C_\sigma = \sigma/\sigma_{Reference}$, $C_\mu = \mu/\mu_{Reference}$.

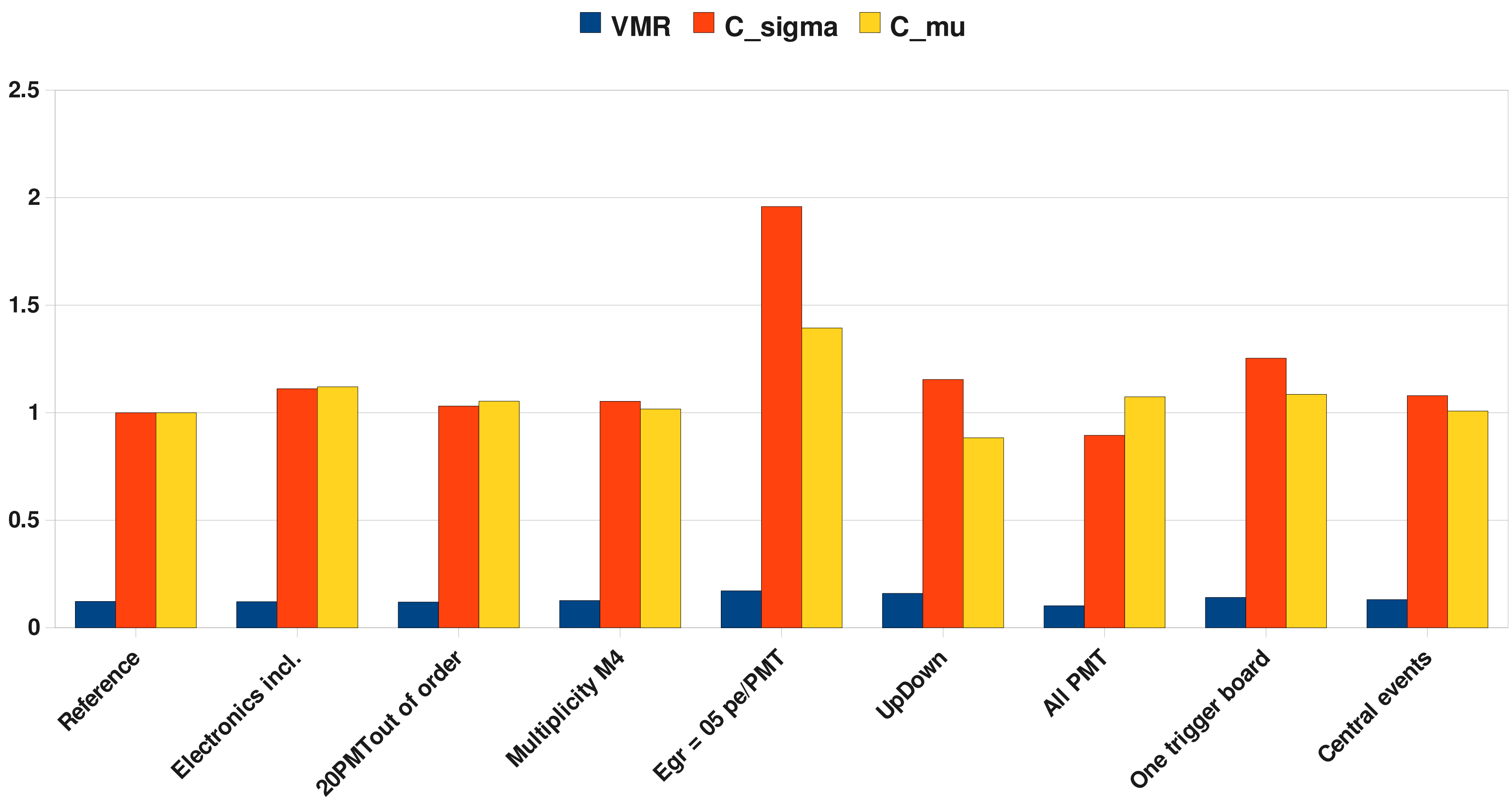

Figure D.1: **The influence of the design configurations on the trigger efficiency parameters.** This figure represents the last 3 columns of table (D.1): VMR (variance to mean ratio), C_σ and C_μ.

List of Figures

List of Tables

Bibliography

[1] W. Pauli. *Letter to L. Meitner and her colleagues* (open letter addressed to the participants of the Tubingen conference on radioactivity), (1930).

[2] E. Fermi, *Versuch einer Theorie der β-Strahlen*, Ricerca Scientifica 2 N12, (1933).

[3] F. Perrin, *Sur la densite de l'energie dans la theorie de la lumiere*, Comptes Rendus 197, (1933).

[4] F.Reines, C.L.Cowan, *Detection of the Free Neutrino*, Phys. Rev. 92 (1953).

[5] C.L.Cowan, F.Reines, F.B.Harrison, H.W.Kruse, A.D. McGuire, *Detection of the Free Neutrino: A Confirmation*, Science 124, (1956).

[6] A. Salam, *Original Papers on the Theory of the Two-component Neutrino*, Nuovo cimento 5, (1957); S.L. Glashow, *Partial symmetries of weak interactions*, Nucl. Phys. 22, (1961); S. Weinberg, *A model of leptons*, Phys. Rev. Lett. 19, (1967).

[7] M.Goldhaber, L.Grodzins, A.W.Sunyar, *Helicity of Neutrinos*, Phys. Rev. 109, (1958).

[8] ALEPH Collaboration, (D. Buskulic et al.), *A Precise measurement of Gamma (Z - b anti-b) / Gamma (Z - hadrons)*, Phys. Lett. B313, (1993); DELPHI Collaboration, (P. Abreu et al.), *Search for Neutral Heavy Leptons Produced in Z Decays*, Z. Phys. C74(1997); L3 Collaboration, (M. Acciari et al.), *Search for charged Higgs bosons in e+e collisions at centre-of-mass energies between 130 and 183 GeV*, Phys. Lett. B431 (1998); OPAL Collaboration, (R. Akers et al.), *Measurement of G(Z to b'b)/G(Z to hadrons) using a double tagging method*, Z. Phys. C65, (1995).

[9] see for example G. McCabe, *The Structure and Interpretation of the Standard Model*, Elsevier (2007)

[10] W.-M. Yao et al, *Review of Particle Physics*, J. Phys. G33, (2006).

[11] LEP Higgs Working Group (G. Abbiendi, et al.), *Search for the Standard Model Higgs Boson at LEP*, Phys. Lett. B565 (2003), arXiv:hep-ex/0306033.

[12] B. Pontecorvo, *Neutrino Experiments and the Question of Leptonic-Charge Conservation*, Zh. Eksp. Teor. Fiz. 53 (1967).

[13] J. N. Bahcall and M. H. Pinsonneault, *What do we (not) know theoretically about solar neutrino fluxes?*, Phys. Rev. Lett. 92, (2004).

[14] H. A. Bethe, *Energy production in stars*, Phys. Rev. 55, 434456 (1939).

[15] A. Cabrera, *Systematic Comparison of the Minos Near and Far Detector Readout Systems*, PhD. thesis, University of Oxford, (2005).

[16] J.N. Bahcalls home page, `http://www.sns.ias.edu/~jnb/SNviewgraphs/snviewgraphs.html`

[17] Kai Zuber, *Neutrino Physics*, IoP. (2004).

[18] Homestake Collaboration (B. T. Cleveland et al.), *Measurement of the Solar Electron Neutrino Flux with the Homestake Chlorine Experiment*, Astrophys. J., 496, 505 (1998).

[19] GALLEX Collaboration (W. Hampel et al.), *GALLEX solar neutrino observations: Results for GALLEX IV*, Phys. Lett. B447, 127 (1999).

[20] SAGE Collaboration (J. N. Abdurashitov et al.), *Measurement of the solar neutrino capture rate by the Russian-American gallium solar neutrino experiment during one half of the 22-year cycle of solar activity*, J. Exp. Theor. Phys. 95, 181 (2002).

[21] E. Kh. Akhmedov, *Neutrino physics*, arXiv:hep-ph/0001264v2.

[22] Kamiokande Collaboration (Y. Fukuda et al.), *Solar neutrino data covering solar cycle 22*, Phys. Rev. Lett. 77, 1683 (1996).

[23] T. J. Haines et al., *Calculation of Atmospheric Neutrino Induced Backgrounds in a Nucleon Decay Search*, Phys. Rev. Lett. 57, 1986 (1986).

[24] Super-Kamiokande Collaboration (Y. Fukuda et al.), *Measurement of a Small Atmospheric Muon-neutrino / Electron-neutrino Ratio*, Phys. Rev. Lett. 81, (1998).

[25] Frejus Collaboration (C. Berger et al.), *Study of atmospheric neutrino interactions with the Frejus detector*, Phys. Lett. B227, 489 (1989).

[26] W. W. M. Allison et al., *Measurement of the atmospheric neutrino favour composition in Soudan-2*, Phys. Lett. B391, 491 (1997).

[27] The NUSEX Collaboration (M. Aglietta et al.), *Experimental study of atmospheric neutrino flux in the NUSEX experiment*, Europhys. Lett. 8, 611 (1989).

[28] LSND Collaboration (A. Aguilar et al.), *Evidence for neutrino oscillations from the observation of anti-nu/e appearance in a anti-nu/mu beam*, Phys. Rev. D64, 112007 (2001).

[29] SNO Collaboration (Q. R. Ahmad et al.), *Direct evidence for neutrino fa-vor transformation from neutral-current interactions in the Sudbury Neutrino Observatory*, Phys. Rev. Lett. 89, 011301 (2002).

[30] Super-Kamiokande Collaboration (S. Fukuda et al.), *Solar B-8 and he p neutrino measurements from 1258 days of Super-Kamiokande data*, Phys. Rev. Lett. 86, 5651 (2001).

[31] Double Chooz Collaboration (F. Ardellier et al.), *Letter of Intent for Double-CHOOZ: a Search for the Mixing Angle Theta 13*, arXiv:hep-ex/0405032v1.

[32] KamLAND Collaboration: (K. Eguchi et al.), *First results from KamLAND: Evidence for reactor anti- neutrino disappearance*, Phys. Rev. Lett. 90, 021802 (2003); KamLAND Collaboration (T. Araki et al.), *Measurement of neutrino oscillation with KamLAND: Evidence of spectral distortion*, Phys. Rev. Lett. 94, 081801 (2005).

[33] CHOOZ Collaboration (Apollonio, M. et al.), *Search for neutrino oscillations on a long base-line at the CHOOZ nuclear power station*, Eur.Phys.J. C 27, (2003).

[34] H. Murayama's home page, `http://hitoshi.berkeley.edu/neutrino/`

[35] K2K Collaboration (E. Aliu et al.), *Evidence for muon neutrino oscillation in an accelerator based experiment*, Phys. Rev. Lett. 94, (2005).

[36] KARMEN Collaboration (B. Armbruster et al.), *Upper limits for neutrino*

oscillations anti-nu/mu ¿ anti- nu/e from muon decay at rest, Phys. Rev. D65, (2002).

[37] MiniBooNE Collaboration (H. L. Ray et al.), *Current status of the MiniBooNE experiment*, (2004).

[38] MINOS Collaboration (P. Adamson et al.), *Search for active neutrino disappearance using neutral-current interactions in the MINOS long-baseline experiment*, Phys.Rev.Lett. 101, (2008).

[39] A. Piepke for the Palo Verde Collaboration, *Final Results from the Palo Verde Neutrino Oscillation Experiment*, Progr.Part.Nucl.Phys. 113-121 (2002)

[40] T. Schwetz, M. Tortola and J. W. F. Valle, *Three-flavour neutrino oscillation update*, New J. Phys. 10, (2008)

[41] F. Beissel, *DC TR 1*, Double Chooz internal note, (2006); F. Beissel, *DC TR MA*, Double Chooz internal note, (2007)

[42] Double Chooz Collaboration (F. Ardellier et al.), *Double Chooz: A Search for the Neutrino Mixing Angle θ 13* arXiv:hep-ex/0606025.

[43] `http://www.caen.it/nuclear/product.php?mod=V1724`

[44] D. Motta, *Double Chooz*, 6th Rencontres du Vietnam - Hanoi, (2006).

[45] Double Chooz Collaboration, *Technical Design Report for the Double Chooz Experiment*, Double Chooz internal note, (2007).

[46] `http://neutrino.phys.ksu.edu/~GLG4sim/`, `http://neutrino.phys.ksu.edu/~GLG4sim/docs/html_latest/FAQ.html`

[47] `http://root.cern.ch/`

[48] `http://www.fluka.org/fluka.php`

[49] P. Antonioli, C. Ghetti, E.V. Korolkova, V.A. Kudryavtsev, G. Sartorelli, *A three-dimensional code for muon propagation through the rock: MUSIC*, Astroparticle Phys. 7, (1997).

[50] S. Brisken, *Die Messung von Neutrinos aus Supernova-Explosionen bei Double Chooz*, Diplom thesis, RWTH University Aachen, (2007).

[51] A. Cabrera, D. Kryn, A. Tonazzo, *The Double Chooz 2nd Level Trigger (Online Data Filter)*, Double Chooz internal note, (2006).

[52] A. Tang, G. Horton-Smith V.A. Kudryavtsev, A. Tonazzo, *Muon Simulations for Super-Kamiokande, KamLAND and CHOOZ*, Phys.Rev. D 74, (2006).

[53] A. Tonazzo, *Muon Rates at the new Near Site*, Double Chooz Collaboration Meeting Kobe, (2008).

[54] B. Reinhold, *Development and Implementation of a Level-1 Trigger and Timing System for the Double Chooz Reactor Antineutrino Experiment*, PhD. thesis, RWTH University Aachen, (2009).

[55] J.B. Birks, *Theory and Practice of Scintillation Counting*, Pergamon Press Oxford, (1964).

[56] *Minutes of the Double Chooz topical meeting held at Aachen April 2006* Double Chooz internal note.

[57] A.S. Cucoanes, *PMT Grouping and the L1 Trigger Efficiency*, Double Chooz Collaboration Meeting - Aachen, (2006).

[58] Hamamatsu Photonics K.K., *Photomultipliers Tubes, Basics and Applications*, (1999).

[59] `http://ie.lbl.gov/education/`

[60] A. Tonazzo, D. Kryn, A. Cabrera, *The L2 Software Trigger (online filter)*, Double Chooz Collaboration Meeting - Aachen, (2006).

[61] P. Kammel, *Muon Capture and Muon Lifetime*, arXiv:hep-ex/0304019v2

[62] T. Luu, C. Hagmann, *Neutron Production by Muon Spallation I: Theory*, UCRL-TR-226323, (2006)

[63] A. W. Wolfendale, *Cosmic Rays*, George Newnes London, (1963).

[64] A.S. Cucoanes *Inner Veto Muon Pattern Recognition*, Double Chooz Collaboration Meeting, Chooz, (2008).

[65] The sample of cosmogenic muons was provided by Daniel Greiner from Physikalisches Institut der Universität Tübingen

[66] `https://cvs.in2p3.fr/dchooz/DOGS/DCDB/data/Geometry/DC_CoordinatesPMT.dat` (v.1.8)

Acknowledgements

I am sincerely indebted to Prof. Christopher Wiebusch and for his constant guidance over my Ph.D period and to Prof. Achim Stahl for giving me the possibility to be part of the Physikalisches Institut IIIB Aachen, and supported this work with helpful discussions. Thank you for all.

My deepest thanks go also to my colleagues, Franz Beissel, Stefan Roth and Bernd Reinhold with whom I worked closely at Aachen.

Special thanks to Anatael Cabrera and, in general, to all the Double Chooz Collaboration.

Finally I would like to acknowledge the Landesamt für Besoldung und Versorgung Nordrhein-Westfalen, the agency who supported my Ph.D.

Toata dragostea mea pentru Florentina, Ana Otilia, mama si tata. Va multumesc pentru tot.

Lebenslauf

Persönliche Daten:

Name: Cucoanes

Vorname: Andi Sebastian

Geburtstag: 16 Oktober 1974

Geburtsort: Câmpina (Rumänien)

Staatsangehörigkeit: rumänisch

Qualifikationen:

1989 - 1993 Bacaleaureat, Liceul teoretic "Nicolae Grigorescu" Câmpina

1998 - 2002 Diploma de licenta, Facultatea de Fizica, Universitatea Bucuresti

2002 - 2004 Diploma de master, Facultatea de Fizica, Universitatea Bucuresti